INTERNALIZATION AND PHOTOINDUCED ENDOSOMAL RELEASE OF POLYPLEXES STUDIED ON A SINGLE CELL LEVEL

KARLA GERDA DE BRUIN
AUS
ALMELO, NIEDERLANDE

2008

Erklärung

Diese Dissertation wurde im Sinne von § 13 Abs. 3 der Promotionsordnung vom 29. Januar 1998 von Herrn Prof. Dr. Christoph Bräuchle betreut.

Ehrenwörtliche Versicherung

Diese Dissertation wurde selbständig, ohne unerlaubte Hilfe erarbeitet.

München, den   2008

Dissertation eingereicht am
1. Gutachter: Prof. Dr. Christoph Bräuchle
2. Gutachter: Prof. Dr. Ernst Wagner
Mündliche Prüfung am   3. Juli 2008

Bobby McFerrin

Summary

In order to develop more efficient gene vectors a detailed understanding of the intracellular behavior of these vectors is essential. Single particle tracking is a method that has proved useful to elucidate biological processes on a single cell level. In this thesis single particle tracking was used to study the internalization, intracellular trafficking, and endosomal release of nonviral gene vectors consisting of plasmid DNA condensed with cationic polymers, so-called polyplexes. A dual-color setup allowed separate detection of either polyplex and GFP-labeled cellular structures or polymer and DNA.

In the first part of this work the internalization of different polyplexes into the cell was studied. The internalization process of epidermal growth factor (EGF) receptor-targeted particles was investigated and compared with untargeted (PEG as well as LPEI) particles. Differences in internalization between targeted and untargeted particles were revealed by trajectory analysis. Trajectories were generated by means of single particle tracking and represented the movement of the particles during internalization. In these trajectories three different phases were distinguished differing in morphology and instantaneous velocities. Analysis by means of quenching experiments and mean square displacement as a function of time enabled a biological interpretation of the three phases.

   The first phase started directly after attachment of the particle to the cell membrane and was characterized by a directed and a diffusional component. The directed component with a value of $v_I = 0.015 \pm 0.003$ μm/s resulted from the retrograde movement of the cortical actin cytoskeleton to which the particles are connected through transmembrane proteins. The diffusional component of $D_I = 4 \cdot 10^{-4} \pm 4 \cdot 10^{-4}$ μm^2/s represented lateral diffusion of the membrane-bound particles on the cell membrane. During phase I particles were internalized into the cell. The second phase represented normal and confined motion in the cytoplasm. The confinements varied between 0.3 and 2.0 μm in diameter. During the third phase active transport along microtubules was visible, indicated by directed motion with a velocity of $v_{III} = 0.7 \pm 0.4$ μm/s.

   Differences between targeted and untargeted particles were found in the duration of phase I. Whereas EGFR-targeted particles showed phase I movement for some minutes, phase I movement could last more than one hour for untargeted particles. This was reflected in the percentage of internalized particles: 90% of the EGFR-targeted particles were internalized within 10 minutes. Untargeted particles showed an extremely large spread but rarely more than 80% internalization even after 80 minutes.

   For the first time, these results give a detailed view on the different phases during internalization and subsequent intracellular trafficking of polyplexes. Moreover these results show that targeting by means of a ligand leads to faster and more efficient internalization.

In the second part of this study the endosomal release of polyplexes was studied. Endosomal release was induced by means of photosensitizer excitation generating singlet oxygen and subsequently membrane damage.

The visualization of endosomal release was first proved with a dextran fluid phase marker. Upon photosensitizer activation the endosomal content was released within 100 ms.

In order to image the endosomal release of polyplexes, plasmid DNA and polymer were labeled with different colors. Three different polymers were used to condense the DNA: LPEI, PLL and PDL. These differ in endosomal buffering capacity, biodegradability and DNA binding affinity.

Differences in release behavior were observed between the particles themselves as well as between polymer and DNA. LPEI particles showed distinguishable behavior for polymer and DNA suggesting dissociation of the complex before endosomal release. LPEI quickly diffused away from the endosome due to its small size. DNA was not degraded but remained intact and immobile in the cytoplasm. For PLL particles polymer and DNA showed similar behavior. PLL quickly diffused away from the endosome. DNA was degraded and also diffused into the cytoplasm. In contrast, PDL particles remained intact in the endosome. In this case, both PDL and DNA did not diffuse out of the endosome but remained colocalized in the endosomal region, indicating intact particles.

These observations suggest differences in the final destination of the complexes. LPEI particles remained in endosomes, PLL and PDL particles were transported towards lysosomes.

Apart from increasing endosomal release, photosensitizer activation is known to have side effects on cells. In this study the effect on microtubules, actin, Rab5 and Rab9 proteins and endosomal motion was examined.

In tubulin-GFP expressing cells reduced microtubule dynamics was observed in combination with an intact microtubule skeleton. This may be explained by inhibition of polymerization and depolymerization of microtubules due to photosensitizer binding to tubulin heterodimers. In contrast to microtubules, no effect of the photosensitizer on actin was observed.

A change in location of Rab5 and Rab9 proteins was observed upon photosensitizer activation. Rab5 and Rab9 GFP-marked single endosomes, representing early and late endosomes respectively, disappeared upon singlet oxygen production concomitant with photosensitizer activation. Most probably the Rab proteins changed from their membrane-bound to their cytosolic conformation due to singlet oxygen damage of the connection between protein and membrane.

A last side effect concerned the motion of the endosomes. Upon photosensitizer activation an immediate stop of endosomal motion was observed. This may be related to the change in conformation of the Rab proteins, since Rab proteins play a role in the connection between endosome and microtubules. By transformation of the Rab proteins into their cytosolic form the connection between endosome and microtubule is lost and endosomal motion is stopped.

Combining the data in this thesis new insights into the mechanism of internalization and intracellular trafficking are obtained. Single particle tracking has proved to be an excellent tool in order to study the behavior of single gene vectors in detail. The new insights can be used to develop more effective gene carriers to enhance the efficacy of nonviral vectors.

Contents

1. Introduction

"*Viren, die das Auge retten*" (Viruses that rescue the eye) was the title of an article on the front page of the *Süddeutsche Zeitung* on the 28th of April 2008 [1]. Stephen Howarth, an 18-year-old British boy has suffered from Leber's congenital amaurosis since birth. This illness is an inherited disorder causing severe vision loss, especially in the dark [2]. Vision generally deteriorates over time and patients become blind when they are 30–40 years old. Stephen Howarth and five other patients were treated in a gene therapeutic clinical trial and showed improved visual function after treatment [3, 4].

This is the most recent success in the 20-year-old history of gene therapy trials, starting with a trial on advanced melanoma in 1989 [5]. Gene therapy is based on the introduction of a new, healthy gene into cells lacking expression of this gene. The new gene is introduced into the cell nucleus and can either interfere with a malfunctioning gene's function, restore a lost function or initiate a new function [6]. In this way normal gene expression by the target cells is induced.

There are two different ways to introduce a gene into the cell nucleus: with the help of viruses (viral vectors) or by means of nonviral vectors. In case of Stephen Howarth, an adeno-associated virus was used to carry the gene into the nucleus [3, 4]. In general, viral vectors induce a high expression of the target gene. Nevertheless, their disadvantage is the immunogenic response of the body upon administration. For this reason, a lot of research has been done on alternative vectors, so-called nonviral vectors.

Nonviral vectors consist of plasmid DNA condensed by either a cationic lipid, forming a *lipoplex*, or a cationic polymer in which case the complex is called *polyplex*. This study concentrates on the behavior of polyplexes. Until now, no clinical trials have been done using polyplexes. The main reason for this is the low transfection efficiency of these vectors. In order to induce gene expression, the DNA has to enter the cell nucleus. On its way to the cell nucleus there are several barriers to overcome. First the vector has to enter the cell. For polyplexes this mostly occurs via endocytosis [7]. Second, the complex has to escape the endosome. Third, the DNA has to be transported to the nucleus and fourth it has to enter the nucleus. Viruses have evolved specialized mechanisms to overcome these barriers. Nonviral vectors in contrast have to be modified chemically. In order to make nonviral vectors more efficient the different barriers have to be characterized in detail.

The first cellular barrier a gene vector encounters is the plasma membrane. Polyplexes consisting of DNA condensed with polyethyleneimine PEI are most probably internalized via HSPGs (heparan sulfate proteoglycans) present in the cell membrane [8–11]. Polyplexes equipped with a ligand targeting a specific receptor in the cell membrane showed a much higher transfection efficiency [12–14] and are expected to be internalized via a more efficient mechanism [15, 16]. Conventional biological techniques to unravel the difference in inter-

1

nalization between targeted and untargeted particles provide average or ensemble values. In this study the internalization process of both untargeted and targeted particles is studied on a single cell level. By means of single particle tracking the internalization of individual gene vectors is followed and differences between untargeted and targeted particles are observed in real time.

Another barrier on the way towards the nucleus constitutes the escape from the endosome. Polyplexes are known to be internalized into the cell via endocytosis. Thus, an internalized particle is entrapped in an endosome. In order to deliver the DNA into the cell nucleus the particle has to escape from the endosome. There are different mechanisms to induce escape from the endosome, e.g. using peptides or polymers that react with the membrane and create pores in it [7, 14]. In this study endosomal release is induced by excitation of a membrane-bound photosensitizer and subsequent singlet oxygen production. By means of this photochemical treatment the endosomal membrane is damaged and thus the polyplex is released. This treatment showed an increase in transfection efficiency [17–19]. However, the detailed mechanism has not yet been unraveled. By means of single particle tracking the mechanism of endosomal release of different polyplexes is studied in real time.

The last part of this study concentrates on the side effects of the photochemical treatment. Excitation of the photosensitizer induces singlet oxygen production which is toxic to several cellular components [20]. Here, the influence of the photosensitizer on microtubules, actin, Rab5 and Rab9 proteins and on endosomal motion is studied.

This thesis is structured as follows: the theory chapter following the introduction gives an overview of the basic biological background of this thesis. In chapter 3 the different experimental methods are described. Chapter 4 describes the first set of experiments concerning the internalization process of receptor-targeted and untargeted particles. The results described in this chapter are published in Molecular Therapy [21]. The process of endosomal release, induced by internalization and excitation of a photosensitizer, was imaged for three different gene vectors and is described in chapter 5. Finally, side effects on the cell of the use of photosensitizer are described in chapter 6. These two chapters are submitted for publication in the Journal of Controlled Release.

2. Principles of gene transfer

In this chapter an overview is presented of the biological background of this thesis. It starts with an introduction into gene therapy and different gene vectors. Then the cellular structures and possible barriers are described that a gene vector may encounter on its way from attachment to the cell membrane towards the cell nucleus. This includes a description of the different pathways by which a vector may be internalized into the cell, the endosomes in which the vector is transported inside the cell, release from the endosome, transport into the nucleus and finally expression of the target gene.

2.1 Therapeutic gene transfer

The discovery of DNA by Watson and Crick in 1953 [22] enables us to change the characteristics of a cell on a basic level: by modifying the genome of the cell we can alter its phenotype. Gene therapy makes use of this principle by correction of genetic disorders through interaction with a malfunctioning gene. DNA sequences (the "healthy" gene) are introduced into the cell nucleus of those cells that are supposed to regulate normal expression of the (malfunctioning) gene. The newly introduced gene can either interfere with a gene's function, restore a lost function or initiate a new function [6] to induce normal gene expression by the target cells. The advantage of gene therapy is the potential elimination of the disease state instead of alleviating the symptoms of the disease, as conventional medicines do. Obviously, diseases suitable for gene therapy are diseases caused by a genetic disorder [23].

The first experiments on cloning of mammalian genes in the late 1970s and early 1980s are commonly seen as the precursors of gene therapy [24] resulting in the first human gene therapy trial in 1989 [5]. Although since then more than 1300 gene therapy clinical trials have been performed, in Europe as well as in the USA no gene therapeutic medicine is available yet [25]. A major setback for gene therapy was the death of Jesse Gelsinger in 1999 during a clinical trial with an adenovirus-based gene vector [26]. Another unfortunate case occurred in 2002 when two children, treated for X-linked severe combined immunodeficiency (SCID-X1), developed leukemia [27]. Nonetheless, the treatment was successful in seven other patients. In the last years, positive results were obtained in different trials for the treatment of chronic granulomatous disease (an inherited primary immunodeficiency that affects phagocytes) [28], metastatic melanoma [29], and Parkinson's disease [25]. Most recently, a clinical trial on retinal dystrophy was performed and improved visual function was observed [3, 4].

Two different techniques of gene delivery exist: *ex vivo* and *in vivo* delivery [6, 30]. *Ex vivo* gene delivery involves isolation of cells from a patient, establishment of the cells in tissue culture, gene delivery to these cells and placement of the cells back into the patient. For *in*

vivo gene delivery genes or gene vectors are directly delivered to cells in the patient by local or intravenous injection. Both delivery mechanisms put requirements on the gene vectors that will be discussed in the next sections.

2.2 Overview of different gene vectors

In order to deliver genes into target cells, different possible vectors exist. The most well-known and in most clinical trials used is a viral vector. A viral vector is based on a replication-defective virus where part of the genome is replaced by therapeutic genes. The most commonly used viruses are adenoviruses and retroviruses [25]. A second class of vectors constitutes the nonviral vectors. They consist of a cationic compound condensing the anionic DNA. This cationic compound can be a polymer, in which case the gene vector is called a polyplex or it can be a lipid, and is then named lipoplex. When both lipid and polymer are used, the complex is termed lipopolyplex. The third class of vectors is naked DNA. Naked DNA can be injected directly into certain tissues, e.g., muscle tissue. Recently, gene therapy trials have started to use siRNA to (down)regulate expression of target genes [25]. The advantage of the use of siRNA is that the vector does not need to enter the cell nucleus [31]. When in the cytosol, siRNA degrades the complementary mRNA molecules that are released from the nucleus following transcription.

2.2.1 Viral vectors

Viral vectors are replication-defective viruses where part of the genome is replaced by therapeutic genes. The size of the gene that can be delivered is limited to the size of the original genome of the virus. The large advantage of viral vectors is their high transduction efficiency. Viral vectors can transduce cells *in vitro* with 100–10000 viral genomes per cell, whereas for nonviral vectors 100 times more gene copies per cell are needed [32]. In addition, viral vectors are able to transfect a large fraction of a defined cell population [33]. For these reasons, most gene therapy trials up to 2007 have used viral vectors (67%) [25].

A big problem in the use of viral vectors is the immunogenic response of the body upon administration of the vector. An immune reaction can either be innate and follow immediately after administration, or it can be adapted. In the latter case, the immune reaction is most prominent after the second or third administration of the vector. The immune response is strongly dependent on the viral vector used. Adenoviral vectors induce very strong immune responses, lentiviral and retroviral vectors in contrast almost none [34]. The vehement immune reaction upon administration of adenovirus-based vectors was the cause of death of Jesse Gelsinger in 1999 [26].

A second disadvantage of viral vectors is their affinity for a particular tissue and cell type, called tropism. Specific proteins, present on the coat of viruses, bind to defined receptors expressed on the cell membrane of the target cells. Depending on the virus, these surface proteins and thus their tropism differs. For use in gene therapy a change in tropism may be necessary, since the gene need not necessarily be delivered to the cell type specified by the surface proteins on the virus coat [35]. The efficient transduction of viruses is often caused by their specific tropism together with an infection process which is optimized for the target tissue. Therefore, changing the tropism of a virus may influence the transduction efficiency as well [36].

The third disadvantage of viral vectors is the preferential integration of the genome into an existing gene in the host genome [37]. In this way, the genome of the host cell is altered in an uncontrolled fashion. Treatment of SCID-X1 in the aforementioned gene therapy trial by means of a retrovirus resulted in integration of a therapeutic gene near an oncolytic gene causing leukemia [27]. On the other hand, the integration into the host genome has the advantage of often leading to stable expression of the gene [38].

2.2.2 Nonviral vectors

A general characteristic of nonviral vectors is that they do not use a virus to deliver the DNA into the target cell. The occurrence of serious side effects of viral vectors has motivated an increase in the research on nonviral vectors. The big advantage of nonviral vectors is their biosafety. Whereas viral vectors easily provoke an immune response and can alter the genome of the host cell, nonviral vectors do not incite such a strong immune reaction and will very rarely insert into the host genome. Further advantages of nonviral over viral vectors are the easy chemical modification, the low cost and the large size of genetic material that can be delivered to the target cell. Unfortunately, nonviral vectors are still less efficient than viral vectors in delivery of DNA to the cytoplasm and subsequently to the nucleus.

Different classes of nonviral vectors can be distinguished. The first category comprises *naked DNA*. Via microinjection naked DNA can be delivered into, e.g, muscle cells. Although naked DNA can easily be degraded in the cytoplasm by DNases, clinical trials with naked DNA have been performed [25].

The second class consists of DNA condensed with cationic lipids to protect DNA from degradation, these vectors are called *lipoplexes*. A cationic lipid is a positively charged amphiphile containing a hydrophilic head and hydrophobic tail. In aqueous solution, above a critical vesicle concentration cationic lipids spontaneously form micelles (consisting of a monolayer of the lipid) or bilayer vesicles. A multilamellar vesicle is formed when different bilayers surround each other. Bilayers and multilamellar vesicles are known as liposomes. The overall charge of the liposome is positive and via electrostatic interactions it is bound to the negatively charged DNA [39].

The third class of nonviral vectors is called *polyplexes* and contains DNA and a condensing polymer for DNA protection. Many different possible polymers are under current investigation. They can be separated into biodegradable and nonbiodegradable polymers. Biodegradable polymers include chitosan (a linear aminopolysaccharide, based on the naturally occurring chitin), polyesters and poly-L-lysine (PLL). Nonbiodegradable polymers are for example polyethyleneimine PEI, poly-D-lysine (PDL) and dendrimers. This study concentrates especially on PEI, PLL and PDL. All three condense DNA by interaction of their protonated amine groups with the phosphate groups of DNA.

The chemical structure of PEI is presented in figure 2.1a. It is available in two different forms: linear PEI (LPEI) and branched PEI (BPEI). Condensation of DNA with PEI (both LPEI and BPEI) results in particles with a positive net charge, because of the excess of PEI. PEI particles have been shown to give one of the highest transfection efficiencies compared to condensation with other cationic polymers [40] whereby the linear form of PEI has been shown to give even higher transfection efficiencies than its branched counterpart [41]. For this reason a lot of research has been done on PEI (both linear and branched) and it has
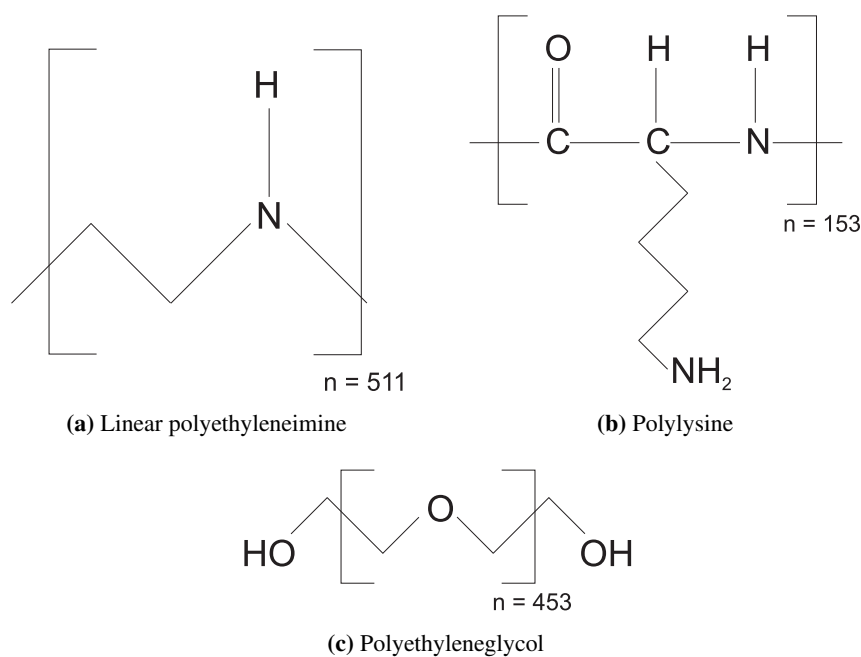
(a) Linear polyethyleneimine

(b) Polylysine

(c) Polyethyleneglycol

Figure 2.1: Chemical structure of linear polyethyleneimine, polylysine and polyethylenegly-col.

become something like a gold standard of nonviral gene delivery [42]. The high transfection efficiency of PEI compared to other polymers is thought to be caused by its high buffering ability; since every third atom of PEI is a protonatable amino nitrogen atom, PEI has a high ability to capture protons [43]. In endosomes, this buffering ability prevents the transition to lysosomes: the so-called "proton sponge" effect (see section 2.5.1) [44, 45].

Poly-L-lysine is one of the first polymers characterized as a DNA-condensing polymer, enabling DNA transfer into the cell [46]. Figure 2.1b shows the chemical structure of polyly-sine. It is a linear polypeptide with repeating units of the L-amino acid lysine and is thus biodegradable. The peptide structure can be degraded by peptidases present in the lysosome. This biodegradability is the big advantage of PLL compared to PEI. Unfortunately, the trans-fection efficiencies of PLL are lower. Moreover, PLL is not biologically inert. It is known to have an influence on membrane permeability [47] and on the internalization mechanism by enhancing pino- and phagocytosis [48, 49]. Additionally polylysine has a lytic activity on cells [50]. The stereoisomer poly-D-lysine (PDL) is also capable of condensing DNA [51]. PDL is not biodegradable since D-amino acids are not naturally present in the cell, and so cannot be degraded by peptidases.

All cationic polyplexes have the disadvantage of inducing an immune reaction *in vivo* by activation of the complement system [52]. Upon intravenous administration, PEI interacts with albumin and red blood cells, and forms aggregates that end up in the lung, causing an embolism [53]. PLL polyplexes also react with red blood cells, but upon binding to plasma proteins, PLL is rapidly cleared from the blood stream [54]. To avoid these unwanted side effects, positively charged polyplexes can be shielded with polyethylene glycol (PEG, chemical structure presented in figure 2.1c) [53]. The electrically neutral PEG shield reduces interactions with blood components.

Intravenously delivered PEI particles lead to high gene expression in the lung and lower expression in other organs like spleen, heart, liver and kidneys [55]. Since these organs may not be the target tissue, enhanced delivery towards a defined tissue is needed. This is achieved by coupling a ligand to the gene vector. The ligand binds specifically to a well-defined receptor that is expressed on the cell surface of the target tissue. In this way, unspecific binding to other tissues is avoided and the gene vector is delivered efficiently to the desired tissue. An example of a ligand is the epidermal growth factor (EGF) which binds to the epidermal growth factor receptor (EGFR) which is overexpressed on tumors. The effect of EGF receptor targeting has indeed already been demonstrated *in vivo* [56].

2.3 Internalization pathways

In general, polyplexes enter the cell by means of endocytosis. For most eukaryotic cells it is the common process to internalize extracellular molecules and larger substances. Endocytic processes can be divided into two different classes: phagocytosis ("cell eating") and pinocytosis ("cell drinking"). Pinocytosis may occur by means of three different mechanisms: macropinocytosis, clathrin-dependent, and lipid raft-dependent endocytosis (whereby lipid raft-dependent endocytosis can be separated into caveolin-dependent and caveolin-independent mechanisms). In the next sections phagocytosis and the different subclasses of pinocytosis will be discussed. A diagram illustrating the different pathways is presented in figure 2.2.

2.3.1 Phagocytosis

Particles larger than ~500 nm in diameter are often internalized by phagocytosis [58]. Upon binding of the particle to the plasma membrane, specialized surface receptors are activated and trigger local actin polymerization. Driven by this polymerization the plasma membrane zippers up closely around the particle so that the particle is engulfed by the plasma membrane. The membrane closes up and the phagosome is sealed off from the membrane and is transported towards the cytosol. Phagocytosis is restricted to so-called phagocytes, in mammals these are, e.g., macrophages and neutrophils [59, p.788].

2.3.2 Macropinocytosis

Macropinocytosis occurs by cell membrane ruffling induced by growth factors or other signals. As with phagocytosis, actin plays a major role in this process [57]. The cell membrane is pushed upwards by local actin polymerization in protrusions perpendicular to the cell mem-
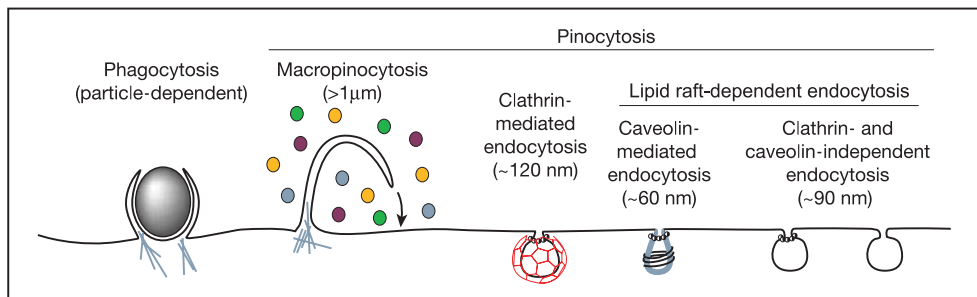
Figure 2.2: Schematic representation of the different internalization pathways as described in the following subsections. Phagocytosis and pinocytosis are the main classes of endocytosis. Three different mechanisms of pinocytosis exist: macropinocytosis, clathrin-dependent endocytosis and lipid raft-dependent endocytosis. Figure adapted from [57].

brane. Unlike phagocytosis, the cell membrane is not zippered up around a particle, but the protrusions collapse onto and fuse with the cell membrane (see figure 2.2). Hereby large and morphologically heterogeneous endocytic vesicles are formed that are typically 0.5–2.5 μm in diameter [60]. By means of macropinocytosis especially macromolecules in large volumes of extracellular fluid are internalized into the cell.

2.3.3 Clathrin-dependent endocytosis

Clathrin-dependent or clathrin-mediated endocytosis (CME) is a form of pinocytosis and is dependent on the protein clathrin. Clathrin consists of three heavy and light chains forming a three-legged structure, a triskelion. By self-assembly, triskelions can form a cage. The first stage in CME is the formation of a coated pit. This is induced by binding of so-called adaptor or assembly proteins (AP's) to the cytosolic site of cell surface receptors [61]. The clustering of AP-receptor complexes triggers clathrin binding to the complexes. Subsequent self-assembly of clathrin into a cage induces the curvature of the membrane, which now represents a coated pit [60,62]. The second stage in clathrin-mediated endocytosis is scission of the vesicle. After clathrin assembly and invagination of the membrane, the GTPase dynamin is rapidly transported towards the small extracellular opening of the invaginated vesicle [63]. Dynamin, together with polymerizing actin, then bring about the detachment from the plasma membrane [64]. Once the vesicle is internalized, the clathrin coat dissociates from the vesicle.

For the Low Density Lipoprotein receptor and the transferrin receptor it was shown that ligands bind to a preexisting coated pit [65] that is present as a stationary structure on the cell surface [66]. However, not all receptors are present in coated pits on the cell surface. The epidermal growth factor (EGF) receptor clusters only upon ligand binding [67–69], followed by clathrin redistribution to the cell periphery [70]. A comparable behavior is observed for the endocytosis of influenza viruses [71].

2.3.4 Lipid raft-dependent endocytosis

In addition to the clathrin-mediated pathway, the existence of several clathrin-independent, but lipid raft-dependent endocytic pathways has been demonstrated (for a review on this subject, see Nichols et al. [72] or Sandvig et al. [73]). These pathways are distinctly less well understood than clathrin-dependent endocytosis and contrary views exist on the importance and abundance of several pathways [73–75].

For all clathrin-independent pathways the presence of lipid rafts[1] was confirmed, as far as biochemical assays have been carried out [72]. The best characterized of these pathways is caveolin-mediated endocytosis. Although the extent of uptake via this pathway is controversial [74–76], both SV40 virus and cholera toxin are known to use caveolae for their internalization [77, 78]. Caveolae are flask-shaped invaginations in the plasma membrane with a size of 50–80 nm in diameter, that are highly immobile and rich in caveolin, a dimeric cholesterol-binding membrane-associated protein. The endocytic mechanism of caveolae remains to be elucidated but the entry of the SV40 virus revealed uptake into organelles that were distinct from classical endosomes and were called 'caveosomes' [79]. Evidence also exists that the protein dynamin is involved in caveolar endocytosis [80].

Several other clathrin-independent pathways have been demonstrated which can be classified as dynamin-dependent or dynamin-independent. Many involve small GTPases such as RhoA, CDC42 or ARF6 [81]. Some of them show a dependence on the endocytic protein flotillin. The detailed mechanism of these pathways is still unclear and more research has to be done to elucidate it.

2.4 Endosomal transport

Once internalized into the cell via endocytosis, a gene vector is entrapped in an endosome. The main function of the endosome is sorting out cargo for degradation and cargo for recycling. This occurs immediately after internalization, in the early endosome. Cargo designated for degradation is transported towards late endosomes and subsequently to lysosomes where acid hydrolases breakdown macromolecules into smaller subunits. In the following the different endosomal compartments are described through which a gene vector can be transported.

2.4.1 Early endosomes

Immediately after internalization by endocytosis, particles are entrapped in early endosomes. These are vesicles with a diameter of 0.3–0.4 μm with extending narrow (< 60 nm) tubules [82] and a pH of around 6.4 [83]. The primary function of early endosomes is sorting of

---

[1] dynamic, detergent-resistant regions of the plasma membrane enriched in cholesterol and lipids

cargo. The slightly acidic pH induces dissociation of several ligands from their receptors (e.g. transferrin) [83]. These receptors are segregated into the tubular extensions which are pinched off from the early endosome and move back to the plasma membrane to recycle the receptors (these endosomes are called recycling endosomes). Not all receptors are recycled in this way. Some remain, together with other cargo that is to be degraded, in the spherical domain of the early endosomes. After pinching off from the tubular domain, the spherical domain fuses with other endosomes (homotypic fusion) such that cargo is concentrated in fewer and larger endosomes [84]. These endosomes are transported towards the perinuclear area along microtubules.

Early endosomes can easily be distinguished from late endosomes or lysosomes by the protein early endosome antigen 1, EEA1 [85]. EEA1 is involved in early endosome docking and fusion [86] and is associated with early endosomes through binding to another protein especially present on early endosomes, Rab5. Rab5 is often used as a marker for early endosomes. It is a small GTPase which is known to regulate fusion events between different early endosomes [87, 88]. It also plays a role in the movement of early endosomes along microtubules [89]. Displacement of Rab5 by the GTPase Rab7 in the perinuclear area induces the transition of early endosomes to late endosomes [84].

2.4.2 Late endosomes

In the perinuclear area, after homotypic fusion, early endosomes are transformed to late endosomes when Rab5 is displaced by Rab7. The pH of late endosomes (lying between 5 and 6 [90]) is lower than in early endosomes. Late endosomes, in contrast to early endosomes, do not exist as a single bilayer vesicle, but consist of several intralumenal vesicles enveloped by an outer membrane. Late endosomes are therefore also called multivesicular bodies (MVB). The intralumenal vesicles are generated by budding of a vesicle from the original membrane, in the same way as endosomes bud from the plasma membrane. The membrane of intralumenal vesicles contains mannose 6-phosphate receptors which distinguishes late endosomes from lysosomes [91]. MVBs sort cargo for degradation and enable fusion with lysosomes [92]. Intralumenal vesicles can in rare cases be recycled back to the cytosol [93,94]. In most cases the content of intralumenal vesicles is delivered to lysosomes. For the transition from late endosomes to lysosomes the contents of both compartments are fused, which was shown by means of confocal microscopy by Bright et al. [95]. This occurred 10–15 minutes after incubation of the cell with dextran.

Rab9 is another member of the Rab family of Rab GTPases. Rab9 is located on the surface of late endosomes and regulates the transport of mannose 6-phosphate receptors to the trans-Golgi network [96]. Rab9 also influences the size of the late endosome [97]. Therefore, Rab9 can be used as a marker for late endosomes.

2.4.3 Lysosomes

Lysosomes are considered as membrane-bound organelles storing a variety of acid hydrolases [98]. They are ∼0.5 µm in diameter, have a heterogeneous morphology and are concentrated in the perinuclear area of the cell. Lysosomes are distinguished from late endosomes by the lack of mannose 6-phosphate receptors. By means of proton-pumping vacuolar ATPases, the pH of lysosomes is maintained at 4.6–5.0 [90] which activates the acid

hydrolases. By fusion with late endosomes, a hybrid organelle is formed which is the major compartment for degradation of cargo [99]. In lysosomes different enzymes are present that can degrade cargo into smaller subunits. Examples are peptidases and glycosidases that can break down polypeptides and glycans or DNases that can degrade DNA into nucleotides. Since enzymes act isomerically specific, only cargo comprised of L-amino acids can be degraded. The smaller subunits are transported out of the lysosome by diffusion and carrier-mediated transport [100].

2.5 Endosomal release

When a gene vector reaches the lysosome, the DNA is degraded by DNases present in the lysosome and active at low pH. To avoid this degradation, the vector has to escape from the (early or late) endosome. Different techniques have been developed to enhance endosomal escape. One example is the use of peptides or polymers that change their conformation upon a decrease in pH, associate with the membrane and in this way induce membrane damage [7]. They can be coupled to gene vectors. One example is melittin, a cytolytic peptide extracted from bee venom that induces transmembrane pores in lipid bilayers [14, 101]. Two additional possibilities to enhance endosomal release are the "proton sponge" effect and the use of photosensitizers. These are discussed in detail below.

2.5.1 Proton sponge hypothesis

The term "proton sponge" was first introduced in connection with the buffering ability of PEI by Boussif et al. [44]. Since every third atom of PEI is a protonable amino nitrogen atom (see figure 2.1a), PEI is an effective "proton sponge". The overall protonation level of PEI increases from 20% to 45% as the pH decreases from 7 to 5 [43]. In case PEI particles are internalized into endosomes, this large buffering capacity leads to reduced acidification of the endosomes and therefore to avoidance of trafficking to lysosomes [102]. In endosomes, a vacuolar ATPase pump brings H^+ atoms inside the endosome and simultaneously Cl^- enters the cell [90]. Due to the buffering capacity of PEI, the influx of protons and concomitant Cl^- ions is large [45]. Thus the osmotic pressure of the endosome increases and leads to increased passive diffusion of H_2O molecules into the endosome. The endosome increases in size, so-called osmotic swelling, whereupon lysis of the endosome occurs [45]. In this way, the gene vector is released from the endosome without being degraded by lysosomal enzymes. This makes PEI an efficient gene carrier.

2.5.2 Photoinduced release

Photoinduced endosomal release makes use of the generation of singlet oxygen by excitation of a photosensitizer. The principle is illustrated in figure 2.3. A photosensitizer, usually a porphyrin, is added to the cell together with the gene vector. The photosensitizer binds to the plasma membrane and is internalized via endocytosis [103]. By illumination with light of a defined wavelength, the photosensitizer is excited into a singlet state and intersystem crosses to its lowest excited triplet state [104]. This triplet state can be quenched by molecular oxygen resulting in generation of singlet oxygen. Singlet oxygen is a highly reactive species with a lifetime of maximal 4 µs in H_2O [105] and a diffusion radius of ~50 nm [106]. It is known
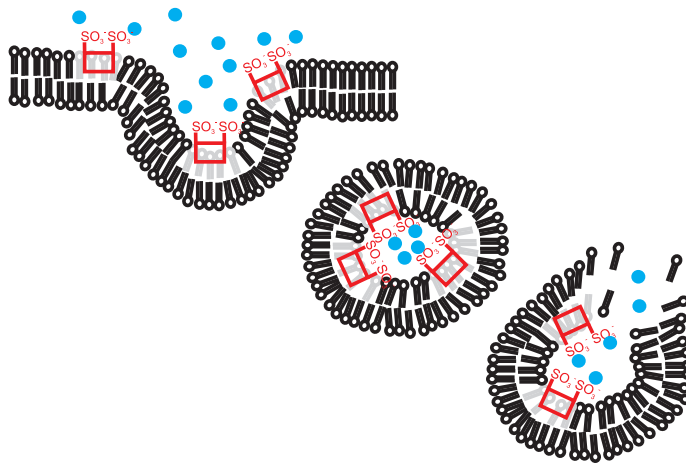
Figure 2.3: Mechanism of photoinduced endosomal release. The photosensitizer (red) binds to the plasma membrane and is endocytosed together with the gene vectors (blue). Upon activation of the photosensitizer, singlet oxygen is generated and the endosomal membrane is damaged. The endosomal cargo is then released into the cytoplasm.

to oxidize membrane lipids, proteins, amino acids and several other organic macromolecules [20] close to the site of generation. Since these molecules are present in the endosomal membrane, the membrane is damaged enabling the cargo to get out of the endosome [104].

2.6 Nuclear import

Although endosomal release is a large barrier in gene transfer, transport towards the nucleus and nuclear entry are at least as important. Late endosomes are localized close to the nucleus and endosomal release may therefore release the DNA close to the nucleus. Due to its size, transport of the plasmid DNA to the nucleus is extremely slow [107, 108]. However, most research has focused on nuclear import rather than on the transportation towards the nucleus.

In general, two possibilities exist for a nonviral vector to enter the nucleus. A first possibility exists when the cell undergoes mitosis. The nucleus is separated from the cytosol via a double membrane, called the nuclear envelope. During mitosis, the nuclear envelope completely disassembles [109] and the gene vector can enter the nucleus via diffusion. Indeed, gene transfer has been shown to be dependent on cell cycle [110]. Entry into the nucleus during mitosis has been shown to be the major route for PEI particles [111].

The second possibility comprises nuclear import via small pores in the envelope, so-called nuclear pore complexes (NPC). The upper size limit for passive diffusion through the NPC is ~ 50 kDa [112]. Thus, plasmid DNA must make use of active transport for entry into the nucleus and therefore a nuclear localization signal (NLS) is needed which targets the plasmid towards the nucleus. This nuclear localization signal can be covalently attached to the DNA and interacts with the nuclear pore complex to facilitate entry of the DNA to the nucleus [113–115].

2.7 Gene expression

A most important aspect in gene therapy is the sustained expression of the therapeutic gene. Expression may either be transient or stable. Transient expression is reduced over time because the newly introduced gene does not replicate into new cells. Often duration of expression is related to the form in which the gene is present in the nucleus. The gene can be integrated in the chromosome of the host cell or it may be present as a separate molecule. In general, plasmids from nonviral vectors exist as a separate molecule and they may not be replicated when the cell replicates [38]. Integrating genes into the chromosomes of the cell may induce sustained expression but a site-specific integration of the genes in the chromosome is difficult and there is a risk of integration into an existing gene [37]. Some plasmids are able to replicate extrachromosomally, they are called episomes.

3. Experimental methods

In this chapter the experimental techniques used in this thesis are explained. It starts with a description of polyplex synthesis and of cell culture. Then the principles of widefield fluorescence microscopy are described and the experimental setup is shown. The technique used to analyze the obtained video streams is called single particle tracking and is explained in section 3.5. The last section describes quenching which was used to distinguish intra- and extracellular particles.

3.1 Synthesis of polyplexes

All polyplexes in this thesis consist of plasmid DNA condensed by a cationic polymer via electrostatical interactions. In order to visualize polymer as well as DNA both components were labeled with a fluorescent dye. For the experiments described in chapter 4 only DNA was labeled. To form a polyplex rapid mixing of polymer and DNA is sufficient [116]. Figure 3.1 shows the synthesis of the polyplexes, as described in detail in the following sections. The size of the polyplex depends on the solvent: mixing in heparan buffered glucose results in particles of 100–140 nm, in heparan buffered saline particles grow to a size of 1–1.5 µm [116]. After mixing, the polyplexes were purified by size exclusion chromatography.

3.1.1 DNA labeling

Plasmid DNA (pCMV Luc, ∼ 5500 bp, described in [117]) was covalently labeled with the fluorophores cy3 or cy5 using the Label IT kits (MIRUS, Madison, WI) according to the
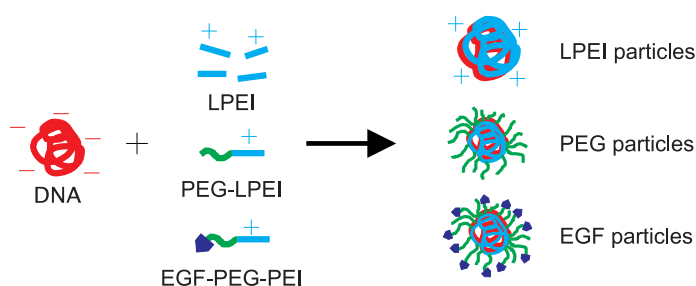

Figure 3.1: Synthesis of LPEI, PEG and EGF particles. PLL and PDL particles are synthesized analogous to LPEI particles. Upon rapid mixing of DNA and cationic polymer polyplexes are formed.

manufacturer's instructions. 20 μg of DNA were diluted with 1X Buffer A to a final volume of 195 μl. After addition of 5 μl reconstituted Label IT reagent, the reaction mixture was incubated for 3 hours at 37°C. To precipitate labeled DNA 550 μl of ice-cold 100% ethanol and 22 μl of 3 M sodium acetate were added. The solution was then mixed and placed at −20°C overnight. Subsequent centrifugation at 16000 rpm for 1 hour at 4°C allowed removal of unreacted label in the supernatant. The pellet was gently washed with ice-cold 70% ethanol and centrifuged again. Labeled DNA was allowed to dry for 5 minutes and finally resuspended in sterile HEPES-buffered glucose (HBG, 20 mM HEPES, glucose mass fraction of 5%, pH 7.1). The concentration of cy3 and cy5 was measured by absorption at 550 nm and 650 nm, respectively. The extinction coefficients of these fluorophores are: $\epsilon_{cy3, 550nm} = 150000 \ \mathrm{lmol^{-1}cm^{-1}}$ and $\epsilon_{cy5, 650nm} = 250000 \ \mathrm{lmol^{-1}cm^{-1}}$. DNA was quantified by measuring the absorbance at 260 nm. The ratio of the absorbance at 260 nm:280 nm is an index for DNA purity. On average, one dye molecule was bound per 50 to 100 DNA basepairs.

3.1.2 Polymer labeling

For the experiments described in chapters 5 and 6 double-labeled particles were used consisting of cy5-labeled DNA and polymer labeled with Alexa Fluor 488 carboxylic acid, succinimidyl ester (A488, Invitrogen, Karlsruhe, Germany). The three polymers used to condense DNA are linear polyethyleneimine (LPEI, MW 22 kDa, Euromedex, Souffelweyersheim, France), poly-L-lysine (PLL-HBr, MW 32 kDa, Sigma Aldrich, Munich, Germany) and poly-D-lysine (PDL-HBr, MW 35 kDa, Sigma Aldrich, Munich, Germany).

For LPEI labeling, A488 was dissolved in DMSO at a final concentration of 10 mg/ml. 1 mg (1.55 μmol) A488 was mixed with 8.54 mg (0.388 μmol) LPEI. The volume was adjusted to 1 ml with HEPES-buffered saline (HBS, 20 mM HEPES, pH 7.4, 150 mM NaCl). The reaction was incubated light-protected for 1 hour at room temperature on a rotation wheel. In order to separate labeled LPEI from free A488, size exclusion chromatography was performed with a gel filtration column (Sephadex G-25 superfine; HR10/30 column, Amersham Biosciences, Germany) preequilibrated with HBS. The amount of A488 and of LPEI was determined spectrophotometrically at 495 nm and via a copper complex assay, respectively. The molar ratio of LPEI:A488 was 1:2.2.

Poly-L-lysine (PLL) and poly-D-lysine (PDL) were labeled according to the labeling protocol for LPEI, with slight modifications. The concentration of A488 dissolved in waterfree DMSO was 5 mg/ml. 0.5 mg (0.775 μmol) of A488 were added to 625 μl HEPES (20 mM, pH 8.0) containing either 12.5 mg (0.391 μmol) PLL-HBr or 13.5 mg (0.391 μmol) PDL-HBr. The reaction was incubated light-protected for 1 hour at room temperature on a rotation wheel. Size exclusion chromatography was performed with a gel filtration column (Sephadex G-25 superfine) preequilibrated with HEPES (20 mM, pH 7.4) containing 0.5 M NaCl. The amount of A488 was determined spectrophotometrically at 495 nm and the PLL/PDL amount by a TNBS assay. The molar ratio of PLL:A488 was 1:1.26 and of PDL:A488 1:1.15.

3.1.3 PEI particles

Unlabeled LPEI was dissolved in water, neutralized with HCl and gelfiltrated on a Sephadex G-25 superfine column using 20 mM HEPES, 0.25 M NaCl, pH 7.4. For complex preparation stock solutions of 1 μg/ml LPEI were prepared and provided by Katharina von Gersdorff and

Carolin Fella (Prof. Wagner, LMU Munich). LPEI particles were prepared at a final DNA concentration of 20 μg/ml by mixing plasmid DNA with LPEI, both diluted in HBG, at a molar ratio of LPEI nitrogen to DNA phosphate (N/P) of 6.

For the experiments described in chapters 5 and 6 double-labeled LPEI particles were used. These particles were synthesized as described above using A488-labeled LPEI instead of unlabeled LPEI.

3.1.4 PEG-PEI particles

For the preparation of PEG (polyethyleneglycol) particles, a PEG-PEI conjugate, consisting of 20 kDa PEG, coupled to 22 kDa LPEI, was synthesized and provided by Katharina von Gersdorff and Carolin Fella (Prof. Wagner, LMU Munich) [116]. The PEG-PEI conjugate was mixed with free LPEI at a molar PEG:LPEI ratio of 22:100. This solution was mixed with DNA at an N/P ratio of 6 and a final DNA concentration of 200 μg/ml. The complexes were incubated for 30 minutes at room temperature, snap-frozen in liquid nitrogen, and subsequently stored at −80°C until use. Before use, the complexes were allowed to stand for 30 minutes at room temperature after thawing.

3.1.5 EGF-PEG-PEI particles

For EGF particles DNA was condensed by a mixture of three different conjugates. The first conjugate (EGF-PEG-PEI) consisted of murine epidermal growth factor (EGF), 20 kDa polyethyleneglycol (PEG) and branched polyethyleneimine. The second conjugate (PEG-PEI) consisted of 20 kDa polyethyleneglycol and linear polyethyleneimine. Both conjugates were synthesized and provided by Katharina von Gersdorff and Carolin Fella (Prof. Wagner, LMU Munich) [116]. These conjugates were mixed with free LPEI at a molar EGF:PEG:PEI ratio of 13:22:100. This solution was then mixed with plasmid DNA at an N/P ratio of 6 and a final DNA concentration of 200 μg/ml. In this way, the amount of PEI in the particles stems for 10% from the EGF-PEG-PEI conjugate, for 12.5% from the PEG-PEI conjugate and for 77.5% from free LPEI. The complexes were incubated for 30 minutes at room temperature, snap-frozen in liquid nitrogen, and subsequently stored at −80°C until use. Before use, the complexes were allowed to stand for 30 minutes at room temperature after thawing.

3.1.6 PLL and PDL particles

For the preparation of PLL and PDL particles A488-labeled PLL or PDL was mixed with DNA (consisting of 50% cy5-labeled DNA) at an N/P ratio of 2 and a final DNA concentration of 20 μg/ml. Complexes were allowed to stand for 30 minutes at room temperature and were subsequently purified.

3.1.7 Polyplex purification

Polyplex purification was only performed for the experiments described in chapters 5 and 6. The polyplexes were purified by size exclusion chromatography to remove unbound, labeled polymer or DNA. For this purpose, a custom made free flow column was used. This method was established by Boeckle et al. [118]. A standard-sized pasteur pipette was plugged with glass wool and column material (Sephacryl S-200 HR, MW exclusion limit 250 kDa for

globular proteins; Pharmacia Biotech, Uppsala, Sweden) and was filled into the glass pipette leading to a final bed volume of 1.5 ml. The column material was equilibrated with HBG at a pH of 7.4. Before loading the polyplexes onto the column, column material was preconditioned with approximately 500 µg of the corresponding polymer-Alexa conjugate to reduce posterior, unspecific binding of the polyplexes to the column material. Then the column was rinsed with HBG and subsequently 600 µl of the polyplex solution were loaded onto the column. The amount of A488 and cy5 was determined by measuring the absorbance at 495 nm and 647 nm, respectively, using a Genesys 10-UV scanning spectrophotometer (Thermo Spectronic, Rochester, USA). The final labeling ratio (molar ratio of A488:cy5) for LPEI, PLL, and PDL particles was 5:1, 5.5:1 and 4:1, respectively.

3.2 Cell culture

Cell culture medium (DMEM/F12) and fetal bovine serum (FBS) were purchased from Invitrogen GmbH (Karlsruhe, Germany). HUH7 WT cells (JCRB 0403; Tokyo, Japan) were cultured in DMEM/F12 (1:1) Glutamax-I medium supplemented with 10% FBS at 37°C in 5% CO_2 humidified atmosphere. 48 hours before seeding the medium was changed to DMEM/F12 (1:1) Glutamax-I with 5% B27 (Invitrogen, Karlsruhe, Germany) to reduce autofluorescence of the cells.

HUH7 actin-GFP and tubulin-GFP (green fluorescent protein) expressing cell lines were produced and provided by Katharina von Gersdorff (Prof. Wagner, LMU Munich) [116]. Rab5-GFP and Rab9-GFP expressing cell lines were produced and provided by Nadia Ruthardt (Prof. Braüchle, LMU Munich).

Cells were seeded in DMEM/F12 (1:1) Glutamax-I medium with 5% B27 24 or 48 hours before measurement in a density of $2.0 \cdot 10^4$ or $1.0 \cdot 10^4$ cells per well (1 cm^2), respectively, on collagen A-coated LabTek chambered cover glass (Nunc, Rochester, NY).

3.3 Widefield fluorescence microscopy

3.3.1 Widefield microscope

Widefield microscopy is based on uniform illumination of a micron-sized sample area [119]. To achieve uniform illumination, Koehler illumination is used. This principle was developed by Koehler in 1893 [120] and is based on a separate illumination and image-forming pathway with different conjugate planes to avoid focusing the light source in the sample [121].

The light source of a modern widefield microscope is mostly a laser or an arc lamp and emits uniform light. This light passes through a collector, focusing it into the back focal plane of the condensor. Most modern fluorescence microscopes are epi-fluorescence microscopes in which the objective serves as a condensor [122]. This has the advantage that excitation light in the detection channel is reduced, since only reflected excitation light will be detected. From the objective a parallel light beam is transmitted, illuminating the sample. The fluorescence from the sample is collected by the objective and is focused on the eye through the eyepiece or onto the camera via a separate side exit of the microscope.

Fluorescent particles are visible on the camera as bright spots on a dark background. Particles that are smaller in size than the excitation wavelength are not presented as points but show a diffraction pattern called an Airy disk [121,123] consisting of a bright spot surrounded
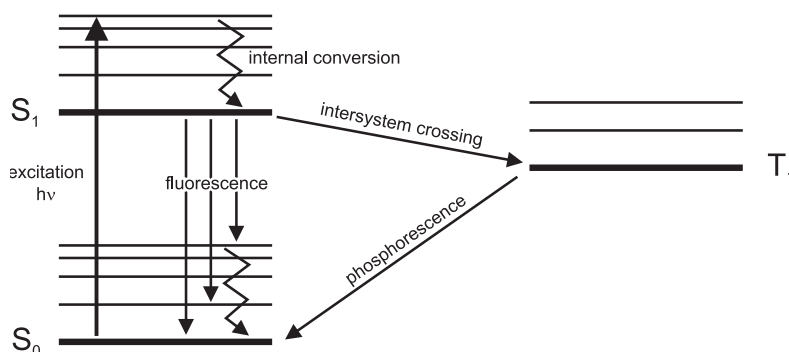
Figure 3.2: Jablonski diagram showing S_0, S_1 and T_1 state. By absorption of a photon with energy hν the molecule is excited from its S_0 state into its S_1 state. From here the molecule can return back into the S_0 state by emission of a photon. By intersystem crossing a transition from the S_1 state into the T_1 state is possible with subsequent relaxation by means of phosphorescence.

by successive dark and bright concentric rings. The position of two adjacent particles can be determined separately, i.e. the particles are just resolved, when the centers of their Airy disks are separated by a distance equal to the radius of the Airy disk. The resolution of a setup – the minimum distance between two particles allowing determination of each particle position separately – is given by the Rayleigh criterion [121]:

$$d = \frac{0.61\lambda}{\text{N.A.}} \qquad (3.1)$$

in which d is the distance between the two particles, λ is the excitation wavelength, and N.A. is the numerical aperture of the objective. A higher N.A. of the objective results in more efficient fluorescence collection and thus in a shorter minimum distance of two objects that can be resolved [124].

3.3.2 Fluorescence

The photophysics of most common fluorescent dyes can be described by a simple three level Jablonski diagram consisting of S_0, S_1 and T_1 state [119]. In figure 3.2 the different states are depicted. For each electronic level several vibrational states are shown. Fluorophores are usually excited to higher vibrational levels of S_1 by absorption of a photon of excitation energy hν (h is the Planck constant, ν is the optical frequency of the excitation light) emitted by a lamp or laser. Via internal conversion the molecule relaxes to the lowest vibrational level of S_1 generally within 10^{-12} s or less [125, p.6]. From this state the excited molecule can return to the ground state by emission of a photon. Fluorescence takes place on a time scale of the order of 10^{-8} s [125]. The molecule is brought back to the initial ground state by means of vibrational relaxation. Vibrational relaxation in both ground and excited state causes a redshift of emission in comparison to absorption. The energy difference between absorption and emission is called Stokes shift.
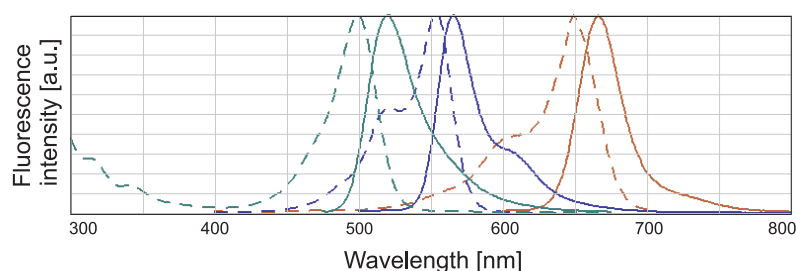
Figure 3.3: Absorption (dotted line) and emission (solid line) spectra of Alexa Fluor 488 (green), cy3 (blue) and cy5 (red).

From the S_1 state also transitions to the first triplet state are possible. This process is called intersystem crossing and involves a change in spin angular momentum [126, p.552]. The triplet state lifetime is in the order of microseconds to seconds and the molecule can relax by means of phosphorescence or by means of a bimolecular deactivation mechanism (quenching).

Two different mechanisms of quenching exist: collisional quenching which is dependent on diffusion of the quencher to the fluorophore and static quenching, in which case a complex is formed between quencher and fluorophore [125, p.237]. A general kinetic expression for a fluorescence quenching reaction is [127]:

$$A^* + Q \underset{k_{-1}}{\overset{k_1}{\rightleftharpoons}} (A^* \cdots Q) \overset{k_2}{\rightarrow} (A \cdots Q) + \Delta$$
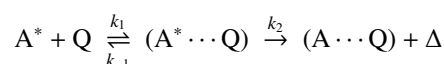
with A* the excited state of a fluorophore, $(A^* \cdots Q)$ an encounter complex and $(A \cdots Q)$ is some resulting complex in which excess energy has been dissipated as heat, Δ. k_1 and k_{-1} are diffusional rate constants for the formation and breakdown of the encounter complex. k_2 is the rate constant for the internal quenching process which may take place as electron spin exchange, electron transfer or resonance energy transfer.

The absorption (dashed line) and emission (solid line) spectra of the dyes most frequently used in this work are presented in figure 3.3. The spectrum of Alexa Fluor 488 is presented in green. This dye was used to trace the endosomal escape of dextran and to label the polymer component in the polyplexes. The spectrum of cy3 and cy5 is presented in blue and red respectively. With these dyes DNA was labeled.

3.4 Experimental setup

The experimental setup is illustrated in figure 3.4. It is based on a Nikon Eclipse TE 200 microscope. In the following the excitation and detection pathway are discussed in detail.

3.4.1 Excitation pathway

Four different lasers were available for the excitation of different dyes. A 405 nm laser was used to excite the photosensitizer, used for the experiments in chapters 5 and 6. It is a 50
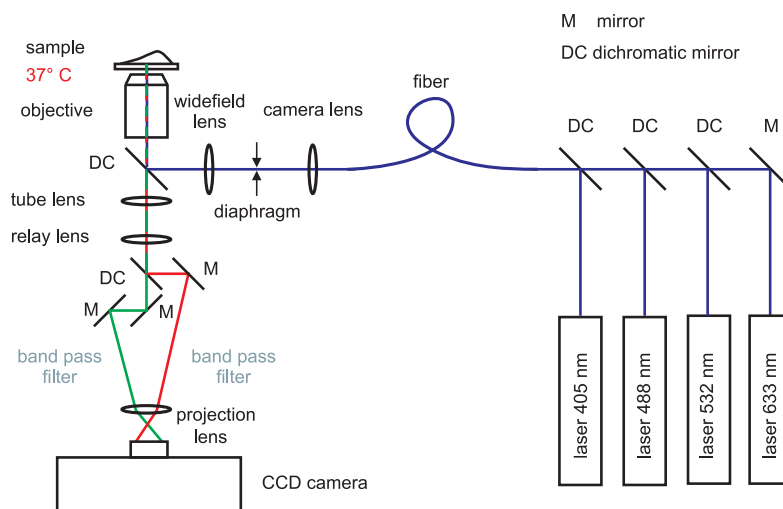
Figure 3.4: Experimental setup. Four different laser lines are available to excite the sample. They are focused into the back focal plane via a fiber and two different lenses. The fluorescence of the sample is collected by the objective and separated into two different channels. These were projected onto two halves of the camera chip.

mW continuous wave Coherent diode laser. This laser was always used at an intensity of 0.34 W/cm^2. A 488 nm Coherent Sapphire (optically pumped semiconductor) laser with a maximum power of 20 mW was used to excite Alexa Fluor 488. For excitation of cy3 a 532 nm a Soliton continuous wave solid phase laser was available with an output of 5–200 mW. The fourth laser was a Coherent Helium-Neon Laser with a maximal output of 35 mW at 632.8 nm. The intensity of the lasers varied extremely between 1 and 200 µW/cm^2 depending on the amount of dye. The laser lines were spatially overlayed via dichroic mirrors and coupled into a multimode fiber (Amphenol, Wallingford, CT) to simplify alignment of the different laser lines. A camera lens (AF Nikkor 50 mm, $f = 45$ mm) was used to parallelize the light at the fibre exit. Through a rectangular field diaphragm the area of excitation was confined to the area detected on the chip of the camera. The laser lines were focused in the back focal plane of the microscope's objective by a widefield lens ($f = 200$ mm). Two different objectives were used for the measurements: a Nikon PlanApo 60x/1.4 and a Nikon PlanApo 100x/1.4. Both are oil immersion objectives.

3.4.2 Emission pathway

The fluorescence light of the sample is collected by the objective and passes through a trichroic mirror. It is focused by a tube lens ($f = 160$ mm). A telescope ($f_1 = 150$ mm, $f_2 = 135$ mm) reduces the image by a factor of 1.1. In the parallel beam path the fluorescence signal is splitted by means of a dichroic mirror, separating light under 640 nm from light above 640 nm. Both emission beams are focused on one half of the camera chip. To eliminate scattered excitation light a filter was placed in each beam path. For the emission

path under 640 nm a bandpass filter was used (550/100 in case of GFP or Alexa Fluor 488 fluorescence and 575/80 in case of cy3). In the emission path above 640 nm another bandpass filter was used (720/150). The detection unit was an EM-CCD (electron multiplying charged coupled device) camera (Cascade 650; Roper Scientific, Tucson, AZ). The camera chip has a size of 653 x 492 pixel. Since 1 pixel on the chip has a size of 7.4 μm x 7.4 μm, 1 pixel on the chip corresponds to 85 nm in case of the 100x objective and 142 nm in case of the 60x objective. The overall magnification of the sample is given by the magnification of the objective times the magnification in the detection pathway [128]. Thus, with a 100x objective a magnification of 90x was obtained and a magnification of 54x was obtained when a 60x objective was used.

3.5 Single particle tracking

The research on imaging of single molecule movement started in 1996 with a publication on visualization of single phospholipids [129]. This arose much interest in imaging of single fluorescent structures, especially in biological contexts, leading amongst other things to the development of a technique called single particle tracking [130, 131]. In contrast to other methods like fluorescence recovery after photobleaching (FRAP) or fluorescence correlation spectroscopy (FCS), single particle tracking studies the properties of one single fluorescent structure, be it a molecule, protein, virus or nonviral vector. Single particle tracking has proved an excellent tool to provide new insights into the characteristics of macromolecules and its surroundings [132–136]. Apart from a direct visualization of single biological structures, the movement of a particle can be analyzed in detail enabling accurate biological interpretation.

To analyze the movement of a single particle, a trajectory has to be generated representing this movement. To achieve this, the position of the particles for each video frame has to be determined. The signal of single fluorescent particles appears on the detector as a spot. In order to determine the x and y coordinates of this spot, different approaches can be used. Direct fitting of a 2-dimensional Gaussian to the intensity profile of the spot is among the most widely used methods [129, 137, 138], since the intensity distribution of a single spot is well approximated by the gaussian equation:

$$f(x, y, A, w) = A \cdot \exp\left(-\frac{(x - x_0)^2 + (y - y_0)^2}{w^2}\right).$$
(3.2)

x_0 and y_0 are the x and y coordinates of the center of the curve, A is the amplitude of the signal and w is the width of the gaussian curve.

After determining the particle coordinates for each frame, the displacement of the particle between successive video frames can be determined. This can be calculated by means of the nearest neighbor algorithm [139].

In this thesis fitting of the Gaussian and calculation of the particle displacement was performed by means of a custom-build programm, developed by Kevin Braeckmans (Ghent University, Belgium) and written in Matlab (The Mathworks, Natick, MA, USA).
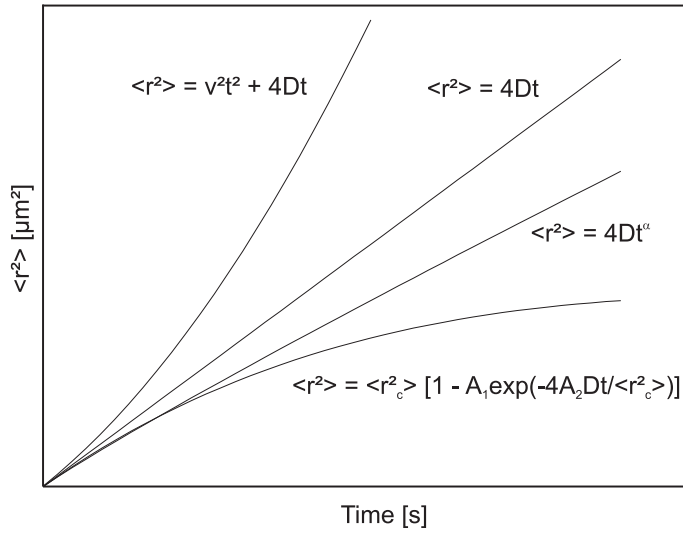
Figure 3.5: Three simulated MSD plots for different types of motion. The mean square displacement $\langle r^2 \rangle$ is plotted versus Δt. A linear plot indicates normal diffusion and is described by $\langle r^2 \rangle = 4D\Delta t$ (D = diffusion coefficient). A quadratic dependence of $\langle r^2 \rangle$ on t indicates directed motion and is characterized by $\langle r^2 \rangle = v^2\Delta t^2 + 4D\Delta t$. Asymptotic behavior for larger Δt with $\langle r^2 \rangle = \langle r_c^2 \rangle[1 - A_1 e^{-4A_2 D\Delta t/\langle r_c^2 \rangle}]$ indicates confined diffusion.

3.5.1   Analysis of single particle trajectories

Single particle tracking provides information on the $x-$ and $y-$coordinates of one particle in time. From these data a 2-dimensional trajectory can be generated. This trajectory not only gives information about the position of the particle in or at the cell, but also provides information on the instantaneous velocity of the particle. More importantly, the trajectory can be analyzed in order to get information on the diffusional behavior of the particle. Latter can be characterized by means of a plot of the mean square displacement (MSD) $\langle r^2 \rangle$ versus the time interval Δt [130]. Several different models have been developed to analyze single MSD curves [130, 140–146]. An example of an MSD-plot showing three different simulated curves is given in figure 3.5. The following considerations are valid for 2-dimensional diffusion only.

The linear plot indicates normal diffusion and can be characterized by

$$\langle r^2 \rangle = 4D\Delta t, \tag{3.3}$$

where D is the diffusion coefficient.

Small deviations from normal diffusion can occur when diffusion takes place in the presence of random obstacles [141]. In this case the MSD curve is characterized by

$$\langle r^2 \rangle = 4D\Delta t^\alpha, \tag{3.4}$$

with $\alpha < 1$. This mode of motion is called anomalous diffusion.

A quadratic dependence of $\langle r^2 \rangle$ on Δt indicates directed motion overlayed by normal diffusion and can be fitted by

$$\langle r^2 \rangle = v^2 \Delta t^2 + 4D\Delta t \tag{3.5}$$

where v represents the mean velocity of the particle.

Asymptotic behavior for larger Δt with

$$\langle r^2 \rangle = \langle r_c^2 \rangle [1 - A_1 e^{-4A_2 D\Delta t / \langle r_c^2 \rangle}] \tag{3.6}$$

indicates confined diffusion. In this case the particle is entrapped in a certain region out of which escape is not possible. $\sqrt{\langle r_c^2 \rangle}$ is the size of the confinement, the constants A_1 and A_2 are determined by the confinement geometry. The asymptotic value of $\langle r_c^2 \rangle$ for large Δt, which is independent of the confinement geometry, was taken for the calculation of the size of the confinement $\sqrt{\langle r_c^2 \rangle}$. Note that confinement within a certain region can only be observed when the observation time is large compared to the time between successive contacts of the particle with the barrier. For short observation times, only normal or anomalous diffusion within the confinement is observed.

3.6 Quenching

Quenching is a deactivation mechanism in which the excitation energy from one molecule is transferred to another molecule that subsequently becomes excited. The molecules must be in close proximity and one may act as a donor, the other as an acceptor. The acceptor molecule may relax into the ground state by fluorescence or phosphorescence [147, p.276-297]

In this thesis, quenching of a fluorescent dye was used to distinguish between intra- and extracellular particles. Trypan blue is a cell membrane impermeable dye that quenches the fluorescence of cy3. Addition of trypan blue to cells incubated with cy3-labeled particles results in fluorescence quenching of extracellular particles whereas internalized particles remain fluorescent. In this way extracellular and internalized particles can be distinguished.

In order to test the quenching effect, trypan blue was added to cy3-labeled particles on a glass surface. For these particles an abrupt decrease in fluorescence intensity was observed upon addition. This control was done for EGF, PEG and LPEI particles and a fluorescence intensity decrease was observed for all three particles. The experiment was repeated with cy3-labeled EGF particles on a cell. Cells were incubated with EGF particles and after 3 minutes $2.5\,\mu l$ of a 0.4% trypan blue solution were pipetted into $400\,\mu l$ medium in the experiment chamber. Two images from an obtained video sequence are presented in figure 3.6a and figure 3.6b. Six particles are marked by boxes. Before addition of trypan blue the fluorescence of the six particles was visible. After quenching, only particles 2 and 3 were visible and have thus been internalized. Particles 1, 4, 5 and 6 were quenched and were therefore still extracellular.

The fluorescence intensity of the boxed particles was plotted versus time in figure 3.6c. Upon addition of trypan blue after 3 minutes, the fluorescence intensities of particles 1, 4, 5 and 6 decreases abruptly to background level. The fluorescence of particle 2 and 3 remains constant. To separate the fluorescence of intra- and extracellular particles, a threshold was set between the intensity of the background and the intensity of the non-quenched particles. The horizontal black line indicates this threshold.

(a) Before quenching

(b) After quenching

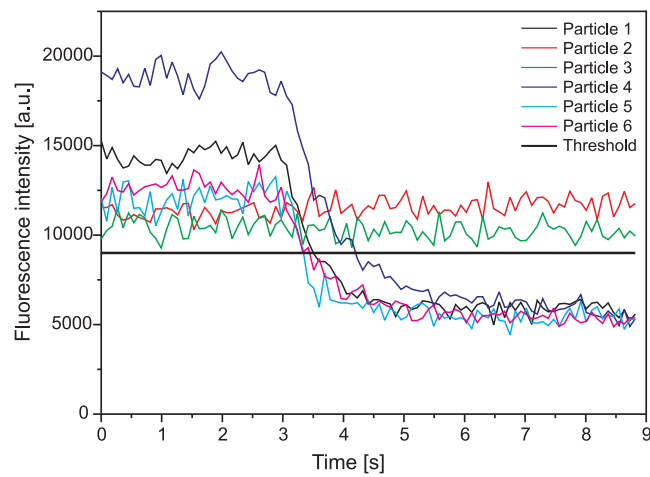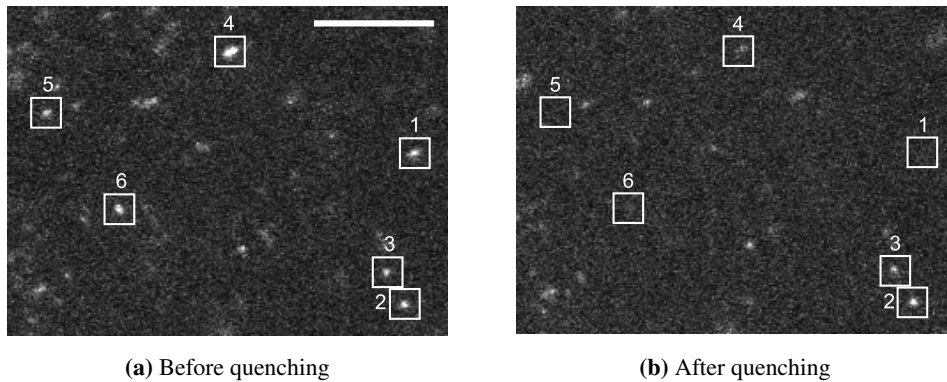

(c) Fluorescence intensity

Figure 3.6: (a) and (b): Two selected frames of a video sequence before and after addition of trypan blue to a cell incubated with EGF particles are shown. Six particles are marked by boxes. Particles 2 and 3 were still visible after quenching and are therefore considered as internalized. Particles 1, 4-6 were quenched and are therefore considered as extracellular. Scale bar: 10 μm. The corresponding fluorescence intensity of the particles is plotted versus time in (c). The quencher was added after 3 minutes. The fluorescence intensity of particles 2 and 3 remained constant whereas particles 1, 4-6 showed a decrease in fluorescence intensity to the background level. The horizontal line indicates the threshold separating unquenched (intensity above threshold) and quenched (intensity below threshold) particles after addition of trypan blue.

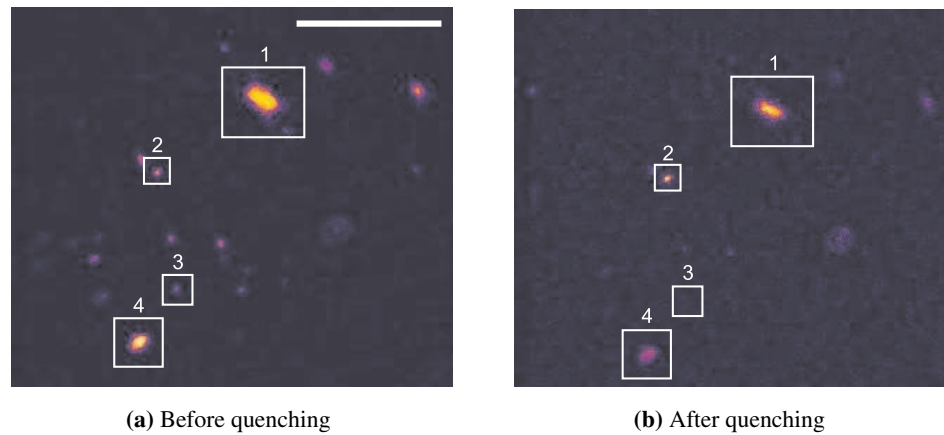**(a)** Before quenching   **(b)** After quenching

Figure 3.7: Two selected frames from a video sequence before and after addition of trypan blue to a cell incubated with PEG particles are shown. The quencher was added 40 minutes after particle incubation. Four particles are marked by boxes. The quenching of these particles is inconclusive. The fluorescence of particle 1 and 4 did not disappear completely. Scale bar: 10 μm.

In contrast to the quenching of EGF particles, PEG particle quenching on cells was inconclusive. Upon quenching large particles lost only part of their fluorescence intensity. An example of quenching of PEG particles in given in figure 3.7. Four particles are marked by boxes. Particle 1 and 4 showed a reduced size after quenching, but the fluorescence intensity (represented by the color map) remained the same. Particle 2 shows comparable behavior. Only the fluorescence of particle 3 has disappeared after quenching.

This inconclusive behavior was representative for PEG particles and made it difficult to state whether PEG particles were internalized or still on the cell membrane. The reduced quenching was observed especially for larger particles. Since larger particles, in particular PEG particles may be internalized by a mechanism different from smaller particles, an explanation for the incomplete quenching may be found in the internalization mechanism. For PEG particles no specific interactions with the cell membrane exist. Therefore, large PEG particles may be internalized via unspecific phagocytosis, described in section 2.3.1. In this pathway, the particle is engulfed by the cell membrane, driven by actin. The membrane completely surrounds the particle after which the so-called phagosome pinches off from the membrane. In case PEG particles are only partly quenched, the cell membrane could have surrounded the particle and may shield part of the particle against the quencher. This would hinder trypan blue to interact with the cy3-dye and causes a reduced quenching effect.

4. Internalization dynamics of polyplexes

The plasma membrane is the first cellular barrier a gene vector encounters on its way to the nucleus. Thus, in order to elucidate gene delivery by polyplexes, understanding the internalization process is of great importance. As we have seen in section 2.2.2, PEI particles, upon administration into the blood stream, especially end up in the lung [55], which may not be the desired target tissue. To enhance uptake by a specific tissue, a receptor-specific ligand can be coupled to the vector. In this way, the gene vector is mainly delivered to cells expressing the receptor corresponding to the ligand. In addition to this tissue-selective delivery ligand-receptor binding activates the receptor-mediated endocytic pathway, increasing uptake efficiency. Several studies have confirmed a positive effect of targeting ligands on gene expression [12] and internalization [13, 14] *in vitro*. However, the mechanism of enhancement by means of receptor targeting has not yet been investigated in detail. In this context, single particle tracking is a promising method to reveal the detailed dynamics and kinetics of the internalization process of targeted versus untargeted gene vectors.

An example of a ligand is the epidermal growth factor (EGF) which targets the epidermal growth factor receptor (EGFR) that is overexpressed on a wide range of tumors. In this chapter the internalization dynamics of polyplexes with and without targeting ligand is compared. The examined polyplexes consist of linear polyethyleneimine (LPEI) which provides the positive charge to condense the negatively charged DNA. The resulting positive charge of the polyplex is shielded by polyethyleneglycol (PEG) reducing unspecific binding of polyplexes to blood components and to cells (section 2.2.2). For targeting purposes EGF was added. Polyplexes consisting of DNA condensed by LPEI and PEG only were used as control particles. Additionally, the internalization dynamics of particles consisting of DNAand LPEI is analyzed. The different particles are hereafter called EGF, PEG and LPEI particles, respectively.

By means of single particle tracking trajectories were generated representing the particles' movement during the internalization process. In the first part of this chapter the morphological distinction of three different phases in the trajectories is discussed and a definition for the phases is given. Following this, the time point of internalization and the percentage of internalized particles for the three different polyplexes are determined. Lastly, the three phases are analyzed in detail by mean square displacement and a biological interpretation of the three phases is given.
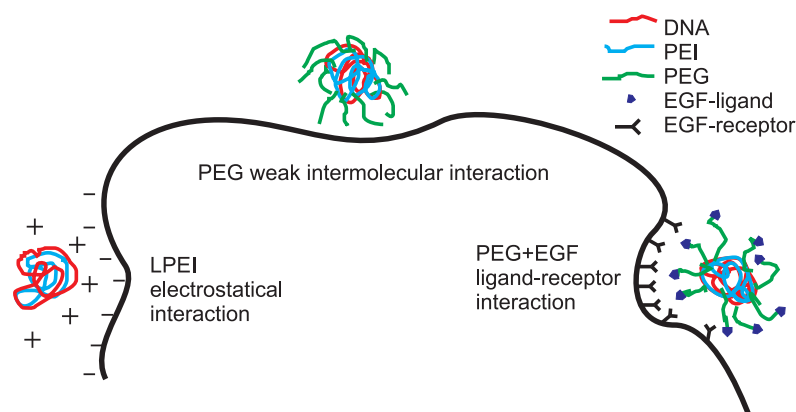
Figure 4.1: Interactions of the three different polyplexes with the cell membrane. LPEI particles bind to the cell via electrostatical interactions, PEG particles show weak van der Waals and hydrogen bond interaction and EGF particles bind to the EGF receptor.

4.1   Internalization of polyplexes

The examined polyplexes represent three different classes of interaction with the cell membrane: electrostatical interaction, interaction via intermolecular forces and ligand-receptor interaction. A schematic of these interactions is presented in figure 4.1. Positively charged LPEI particles interact electrostatically with the negatively charged cell membrane. PEG particles show a weak interaction with the cell membrane via van der Waals forces and hydrogen bonds [148]. Ligand-receptor interaction is represented by EGF particles that target the EGF receptor. In this section an overview is given of the proposed internalization mechanisms of the three particles.

The internalization pathway of PEI[1] particles is based on electrostatical interactions between the polyplex and components of the cell membrane. As a result of the excess of cationic polymer, PEI polyplexes contain a positive net charge (a molar excess of positive charge). The cellular membrane contains a negative net charge due to membrane-associated negatively charged proteins such as proteoglycans [149]. There is strong evidence that sulfated proteoglycans such as HSPG (heparan sulfate proteoglycan) serve as receptors for transfection by cationic polyplexes like PEI particles [8–11]. Inhibition of the sulfation of proteoglycans prevents stable binding and internalization of PEI coupled to quantum dots [10], suggesting a major role of HSPGs in the internalization of PEI polyplexes.

Two major subfamilies of cell surface heparan sulfate proteoglycans are distinguished: the syndecans and the glypicans. They differ in amino acid sequences of their core proteins and mode of interaction with cell membranes. Glypicans are localized especially on the extracellular side of the cell membrane whereas syndecans are transmembrane proteins that can interact with the actin cytoskeleton. Kopatz et al. [150] suggested that syndecans play a major role in polyplex internalization.

---

[1]   the following considerations are valid for linear as well as for branched PEI

The precise internalization pathway and mechanism of HSPGs still remains to be elucidated. It is known that HSPGs can take part in both clathrin- and caveolin-mediated internalization [151]. Also, binding of ligands to cell surface HSPGs can immobilize the proteoglycan in the plane of the membrane. For syndecans, ligand binding promotes dimerization/oligomerization of bound ligand/syndecan complexes, which enhances the interaction with the actin cytoskeleton [152].

The uptake pathway of PEI polyplexes has been examined in several studies by means of inhibitors of the clathrin- or caveolin-mediated pathway [9, 153, 154]. Besides being partly contradictory, the results were strongly dependent on cell type. Also, the pathway seems to depend on the size of the complex [155]. For PEI particles immobilization and interaction with the actin cytoskeleton, as observed for syndecan, was also observed [156].

Most recently, a detailed study examined the uptake of both PEI particles and HSPGs [9]. 100% colocalization of PEI polyplexes and antibodies against HSPGs was found immediately after internalization. Knock down of clathrin and caveolin by siRNA did not show significant inhibition of internalization of both polyplexes and HSPGs. The uptake mechanism of both polyplexes and HSPGs was dependent on dynamin and a high colocalization with the endocytic protein flotillin was found. These findings suggest an internalization pathway for PEI particles through binding with HSPGs independent on clathrin and caveolin, but dependent on dynamin and possibly flotillin.

Due to their positive charge PEI particles have toxic effects *in vivo* as described in detail in section 2.2.2. To reduce unwanted side effects, part of the PEI molecules can be substituted by PEG-PEI molecules (see section 3.1.4). Since the electrically neutral PEG shielding reduces binding to the cell membrane, adhesion of PEG particles to the cell is weak and PEG particles may be internalized in a reduced amount compared to unshielded (PEI) or targeted (EGF) particles. However, the PEG shielding is not complete. Studies on aggregation of PEG particles have shown that particles consisting of DNA condensed with 25 and 10 kDa branched PEI and covalently bound to 20 kDa PEG, were still able to interact with each other and form aggregates [157]. This suggests that the PEG shielding does not completely cover all PEI molecules of one particle. Therefore, some PEI molecules may still interact with the cell membrane and bind to the HSPGs. Since in the experiments partly and completely shielded particles cannot be distinguished, this introduces a bias towards partly shielded PEG particles.

Little is known about internalization of PEG-shielded particles. Luten et al. [158] compared poly(DMAEA-co-BA)phosphazene-based polyplexes with and without PEG shield by means of confocal microscopy and observed a reduced association and internalization in the case of PEG-shielded complexes. In our experiments PEG-shielded particles are used as a control to EGF particles to examine the influence of the EGF receptor targeting.

EGF particles consist of a PEI, a PEG-PEI and an EGF-PEG-PEI part (see section 3.1.5). The EGF ligand serves to target the epidermal growth factor receptor (EGFR), which controls proliferation, differentiation and cell survival. The EGF receptor is overexpressed on a wide range of solid tumors, including glioblastoma and hepatocellular carcinoma [159].

The EGFR is a 170 kDa transmembrane glycoprotein with a ligand-binding domain on the extracellular site of the plasma membrane [160]. Before binding of a ligand, EGFR is distributed evenly over the cell surface [68]. Upon binding, EGF receptors cluster into coated pits [15, 67–69] followed by clathrin redistribution towards the cell periphery [70]. The

latter observation, together with a publication on the colocalization of EGF with LDL (Low Density Lipoprotein), a protein that is present on clathrin-coated vesicles, suggests that EGF is internalized via the clathrin-coated pathway. However, clathrin-independent mechanisms for the uptake of EGF have also been described [16, 161, 162]. Taken together, internalization via both clathrin- and caveolin-dependent mechanisms seems likely [15, 16].

Internalization of ligand-bound EGFR is very fast. Haigler et al. described EGF-ferritin localization in vesicles after 2.5 minutes [69] and Baulida reported the internalization of ^{125}I-EGF starting after 1.5 minutes [163].

4.2 Tracking of polyplexes

In order to clarify the difference between EGF-targeted and untargeted, shielded PEG particles, 2-dimensional trajectories of both particles representing the internalization process were generated. In addition LPEI particles without targeting and shielding component were measured. For this purpose, the cells were treated as follows. HUH7 WT cells were seeded 24 or 48 hours before measurement in a density of $2.0 \cdot 10^4$ or $1.0 \cdot 10^4$ cells per well, respectively, on collagen A-coated LabTek chambered cover glass. EGF, PEG and LPEI particles were prepared as described in section 3.1. Before measuring, the medium of the cells was changed to CO_2-independent medium. Cells were placed on the microscope on a heated microscope stage at 37°C. To enable tracking of particles using our computer software particles had to remain in the focal plane to avoid a change in fluorescence intensity or disappearance of the particle. Therefore, cells had to be flat and preferentially the flat peripheral cytoplasm was imaged. Particles were pipetted directly onto the cell under observation in order to get a clear starting point of the attachment to the cell membrane. The DNA concentration on the cell was unimportant, as in the measurements single particles were followed and no dependency of the internalization on the DNA concentration was to be expected. The concentration was adjusted such that individual particles could be detected and afterwards tracked. This was achieved with a DNA concentration of 5.0 μg/ml for EGF and PEG particles and a concentration of 1.0 μg/ml for LPEI particles. Sometimes particles moved out of the focal plane due to cell movement during the measurement or during internalization. As already discussed above, tracking was hampered in these cases.

Taking into account the aforementioned conditions, the movement of the polyplexes on the cell was imaged. The obtained sequences show that the particles quickly sedimented and attached to the cell surface. After contact with the cell surface, EGF and LPEI complexes were irreversibly docked onto the cell membrane due to their specific interactions. For PEG particles a weaker attachment to the cell membrane was found than for EGF particles. By resuspension of the medium in the chamber PEG particles were easily removed from the cell surface, and undocking and docking events were even observed spontaneously with diffusion between these events in the medium closely above the cell membrane.

4.2.1 Trajectories of EGF, PEG and LPEI polyplexes

Particle trajectories representing the movement during internalization were obtained by means of single particle tracking (see section 3.5). More than 100 trajectories of single EGF, PEG and LPEI particles were generated representing the particle movement up to 20 minutes after cell
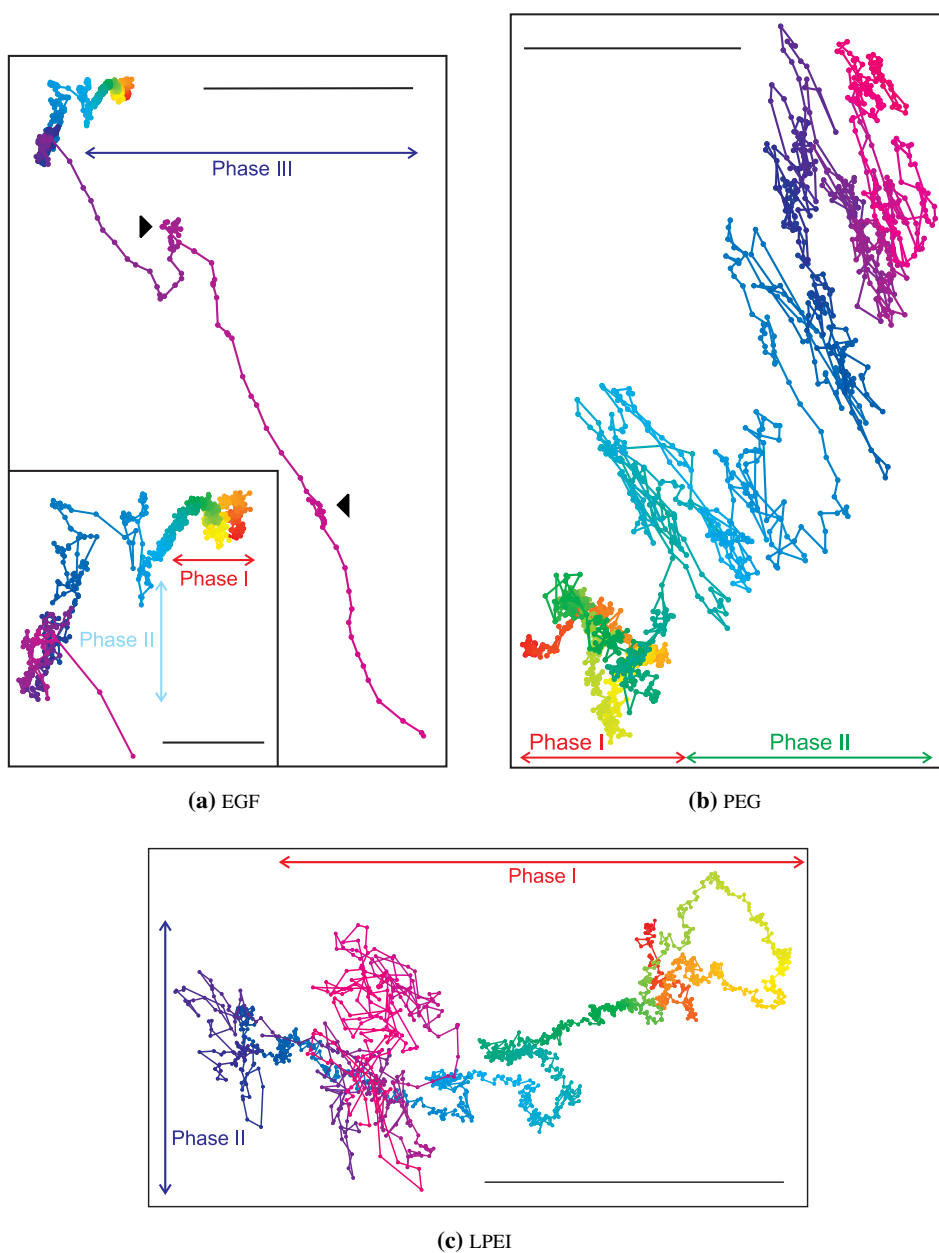
(a) EGF

(b) PEG

(c) LPEI

Figure 4.2: Trajectories of the particles. The color changes with progressing time from red through green to blue. (a) and (b) start directly after attachment of the polyplex to the cell membrane. The trajectories represent: (a) an EGF particle tracked over a period of 4.5 minutes with an acquisition time of 300 ms. The inset shows an enlargement of the first part of the trajectory. Three morphologically distinguishable phases can be detected. Scale bar: 5 μm; scale bar inset: 1 μm. (b) a PEG particle tracked over a period of 13.5 minutes (acquisition time: 500 ms). Two distinguishable phases can be detected. Scale bar: 2 μm. (c) a LPEI particle tracked over a period of 13.2 minutes (acquisition time: 500 ms). The trajectory starts 9.5 minutes after the attachment to the cell membrane. Two distinguishable phases can be detected. Scale bar: 2 μm.

attachment. In all trajectories, morphologically distinguishable phases could be observed. A definition for these three phases will be presented at the end of the next section.

In figure 4.2 a representative trajectory is shown for all three particles. Figure 4.2a represents a trajectory of an EGF particle recorded for 4.5 minutes starting with the attachment to the cell membrane. The inset shows an enlargement of the first part of the trajectory. In this figure, three different phases with morphologically distinguishable patterns can be detected. The first phase, which lasts until $t = 160$ s, is characterized by steps that cannot be individually distinguished, since the distance between subsequent steps is small. Also, a small directional component is visible in the trajectory. The second phase is characterized by an increased distance between subsequent steps and is accompanied by random motion of the particle. The third phase starts at $t = 240$ s. Here, the distance between subsequent steps is largest and steps are unidirectional. During the third phase alterations in the direction occur, these are marked by arrowheads. For EGF particles, three morphologically different phases were observed for the majority of the particles.

A trajectory of a PEG particle is presented in figure 4.2b. Although the PEG particle was tracked more than three times as long as (13.5 minutes) the EGF particle, only two different phases can be distinguished. The first phase consists of small steps within a small region of the cell and lasts until $t = 385$ s. The transition to the next phase is represented by a color change from green to blue. Within a few seconds the particle moves away from the small area where it remained during the first 385 seconds and single steps of the particle can be distinguished. The movement of the particle seems to go preferentially parallel to one axis. This might be caused by structures in the cytosol that hinder movement of the particle. This hypothesis will be discussed in detail in section 4.5.2. For PEG particles often two morphologically different phases were observed.

A trajectory of a LPEI particle is presented in figure 4.2c. The trajectory starts 9.5 minutes after pipetting the polyplexes onto the cells. The particle was tracked over a period of 13.2 minutes. In the beginning of the trajectory the particle moves in a circle that is completed within 4 minutes. This kind of movement was observed often (also for PEG and EGF particles) and may be explained by movement of the particle captured by filopodia as described in [164] and [165]. Filopodia may attach to the particle and pull the particle towards the cell. After 582 seconds the movement of the particle changes to the next phase where individual steps can be distinguished. As for PEG particles, often two morphologically different phases were observed.

In short, for all three particles morphologically distinguishable phases were observed. In order to sharply define the characteristics of these phases, velocity plots were generated.

4.2.2 Instantaneous velocity plots of EGF, PEG and LPEI polyplexes

The three phases observed in the trajectories are morphologically distinguishable by means of their step sizes. Therefore, the distance traveled in 1 second was plotted versus time in order to define the phases. The plots thus show instantaneous velocities. In figure 4.3 the instantaneous velocity plots corresponding to the trajectories shown in figure 4.2 are

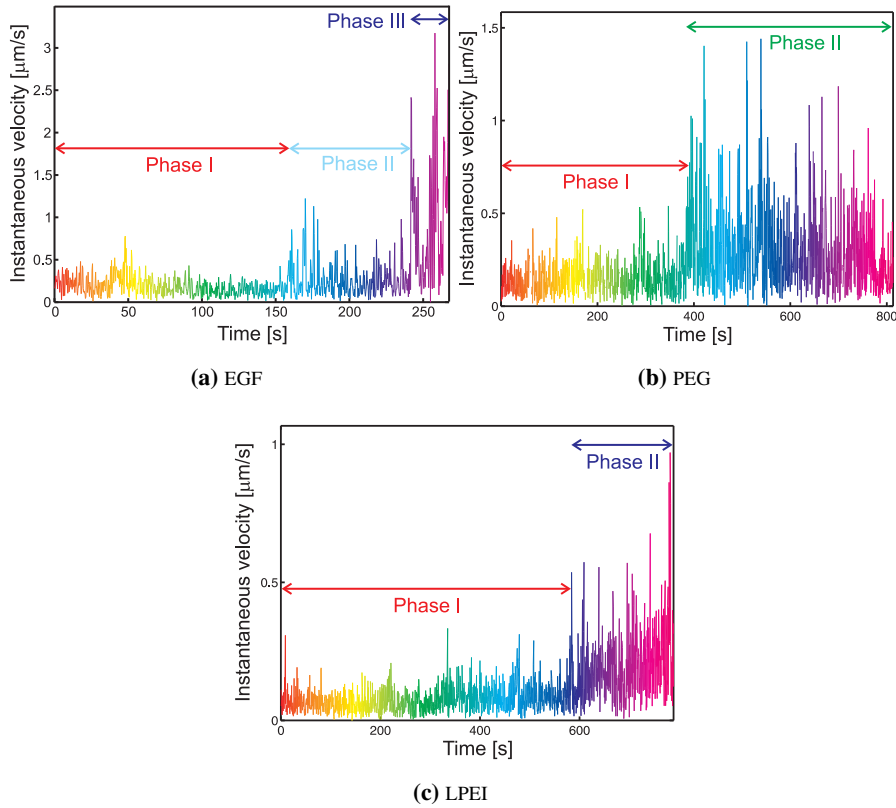**(a)** EGF

(b) PEG

(c) LPEI

Figure 4.3: Instantaneous velocity plots corresponding to the trajectories in figure 4.2. The color coding matches that of figure 4.2. The plot represents the instantaneous velocities of (a) an EGF particle. Three different phases can be distinguished based on the differences in instantaneous velocity. (b) a PEG particle. Two different phases can be distinguished. (c) a LPEI particle. Two different phases can be distinguished.

presented. Corresponding time points are marked with the same color.

In case of the EGF particle three different phases are clearly recognized in the plot. During the first phase, instantaneous velocities around 0.25 µm/s are measured. A clear increase in instantaneous velocity is observed for the second phase and another increase marks the beginning of the third phase. The time points of the phase changes correspond well to the morphological change in the trajectory: phase I was observed until $t = 160$ s, phase II until $t = 242$ s followed by phase III.

In figure 4.3b the instantaneous velocities of the PEG particle are plotted. Here, the distinction between the first and second phase is even more pronounced. Phase I is observed until $t = 385$ s, where the instantaneous velocity is around 0.25 µm/s. Phase II starts abruptly at $t = 385$ s and instantaneous velocities of up to 1.45 µm/s are observed.

For the LPEI particle, the transition from phase I to phase II is observed at $t = 582$ s. The

velocity of the first phase is in the same range as for EGF and PEG particles: velocities up to 0.3 μm/s are measured. The second phase is characterized by larger velocities up to 1.0 μm/s.

From these results it is clear that the different phases observed in the trajectories can be defined by their instantaneous velocities. Remarkably, comparing the velocity plots of the three particles, it becomes clear that for all three particles the first phase shows instantaneous velocities in the same range. For the second phase the values are in the same range as well. This implies that a definition of the different phases can be formulated applicable to all three particles.

After generating velocity plots for more than 100 EGF, PEG and LPEI particles, the phases were defined as follows: phase I contains no more than 5 successive steps with an instantaneous velocity above $v = 0.5$ μm/s. Phase II was defined as the intermediate period between phase I and phase III and was heterogeneous in respect to instantaneous velocities. In most cases, the average instantaneous velocities were above $v = 0.5$ μm/s. Phase III was distinguished from phase II by the criterion that it contains at least 16 successive steps in the same direction.

Having defined the phases, we can concentrate on the main question of this chapter: what is the difference between EGF particles and PEG particles? For PEG particles as well as for EGF and LPEI particles different morphologically distinguishable phases were detected during the internalization process. The instantaneous velocities of the different particles were in the same range. A difference was only found in the duration of phase I. Typically, for EGF particles, phase I lasted a few minutes, whereas for PEG particles and LPEI particles phase I could last more than half an hour.

4.3 Time point of internalization

After defining the different phases during the internalization process the question arises during which phase a particle is internalized into the cell. To determine the time point of internalization, a distinction must be made between extra- and intracellular particles. This was achieved by performing quenching experiments with trypan blue. This dye is cell membrane impermeable and quenches the fluorescence of cy3 as described in section 3.6. Addition of trypan blue to cells incubated with cy3-labeled particles results in fluorescence quenching of extracellular particles whereas internalized particles remain fluorescent. In this way extracellular and internalized particles could be distinguished and latter could be tracked further. Particles could be quenched only once and did not recover their fluorescence upon removal of the quencher. Therefore, one quenching experiment represents one single-cell measurement. For the quenching experiments, cells were treated similarly as described in section 4.2. To induce quenching, 2.5 μl of a 0.4% trypan blue solution were pipetted into 400 μl medium in the experiment chamber. Control experiments were performed and are described in section 3.6.

(a) Trajectory
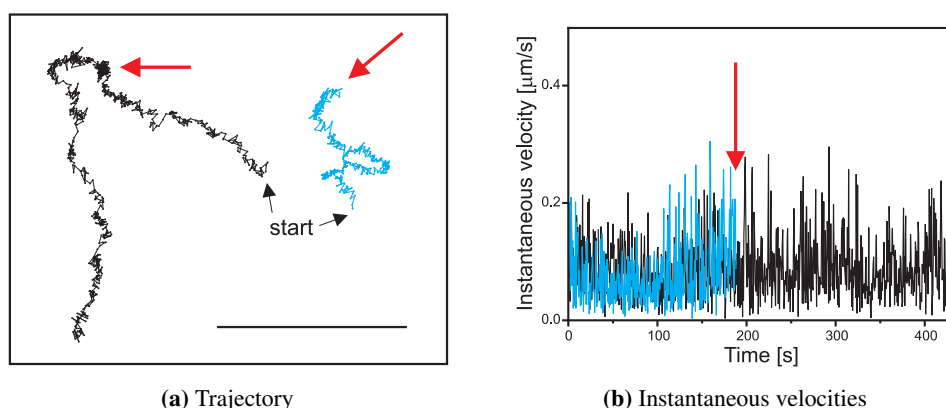

(b) Instantaneous velocities

Figure 4.4: (a) Trajectories of two EGF particles showing phase I, tracked over a period of 192 s (blue) and 424 s (black) with an acquisition time of 500 ms. After 192 s trypan blue was added to the cells (indicated by red arrows). One particle was quenched and the trajectory stops (blue). The other particle remains visible and still shows phase I movement (black). Scale bar: 2 μm. (b) Instantaneous velocity plot of the trajectories presented in (a). Both particles show the small instantaneous velocities characteristic for phase I.

To examine the time point of internalization in relation to the obtained trajectories, video sequences were recorded with different time points of quenching starting with particle attachment to the cell membrane. Trajectories were obtained as described before (section 3.5) and the different phases were related to the quenching behavior. 40 trajectories were analyzed and quenching of (part of the) polyplexes was only observed during phase I. Particles showing phase II or phase III motion were not quenched.

In figure 4.4a an example is given of two EGF trajectories showing phase I movement at the time point of quenching. After 192 seconds trypan blue was added, indicated by red arrows. One particle was quenched: the trajectory stops at the moment of quencher addition (blue). The second particle remains visible (black). This implies that the particle of which the trajectory is shown in blue was not internalized at the moment of quencher addition, whereas the second particle had already been taken up by the cell. The corresponding instantaneous velocities are plotted in figure 4.4b. Both particles show the small instantaneous velocities characteristic for phase I. These results show that during phase I particles can be either on the cell membrane or internalized in the cell and imply that during phase I internalization occurs.

An example of a trajectory showing phase II movement during quencher addition is given in figure 4.5a. The trajectory corresponds to a LPEI particle tracked for 16 minutes. At first phase I movement is displayed. After 585 seconds, phase II movement starts. With the start of phase II single steps in the trajectory become visible and in the corresponding instantaneous velocity plot (figure 4.5b) an increase shows up. Trypan blue is added after 840 seconds (in both figures indicated by a black arrow). The particle remains visible and has therefore already been internalized.
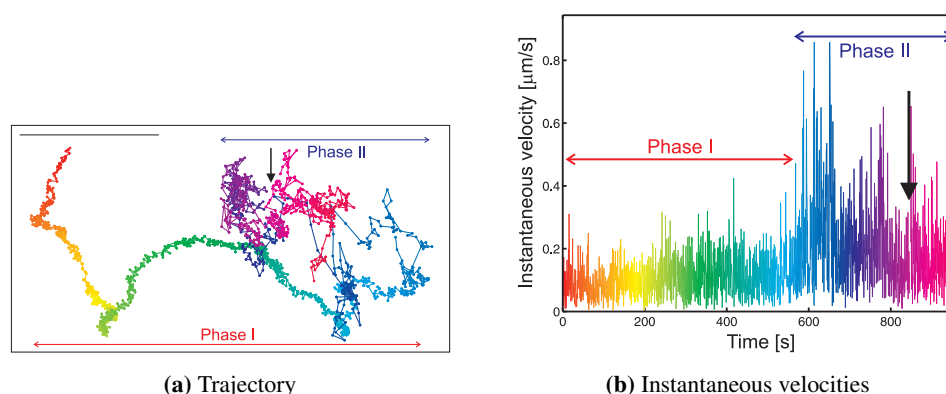
(a) Trajectory

(b) Instantaneous velocities

Figure 4.5: (a) Trajectory of a LPEI particle tracked over a period of 964 s with an acquisition time of 500 ms showing phase I and phase II. After 840 s, during phase II movement, trypan blue was added to the cells (indicated by a black arrow). The particle was not quenched. Scale bar: 2 μm. (b) Instantaneous velocity plot of the trajectory presented in (a). During phase I, small instantaneous velocities are observed. The beginning of phase II is easily recognized by a sudden increase in instantaneous velocity.

In summary, the quenching of most particles during phase I indicates that particles are still accessible to trypan blue and attached to the extracellular side of the membrane. Sometimes particles are not quenched during phase I. These particles obviously have been internalized by the cell. During phase II and phase III no quenching was observed and these phases therefore represent intracellular movement. Combining these results demonstrates that internalization of the particles takes place during phase I only.

4.4 Internalization percentages

The main question of this chapter concerns the difference in the internalization process between receptor-targeted EGF particles and untargeted PEG particles. In addition, LPEI particles without targeting and shielding component were examined. In section 4.2 we saw that differences between EGF particles and PEG particles are only observed in the *duration* of phase I. In the last section we saw that during phase I internalization takes place. These findings raise the question whether a difference is observed in the *internalization kinetics* of EGF and PEG particles. This question can be answered by quenching of particles at different defined time points and determination of the percentage of internalized particles.

Video sequences were recorded as described before (section 4.2). Trypan blue was added to the cells at different time points (see section 4.3). By analysis of the video streams, as described in section 3.6, the percentage of internalized particles per cell was determined at various time points. Single frames before and after quenching were analyzed with respect to the fluorescence intensity of all particles. By thresholding, the total number of particles before and after quenching was counted as demonstrated in figure 3.6.

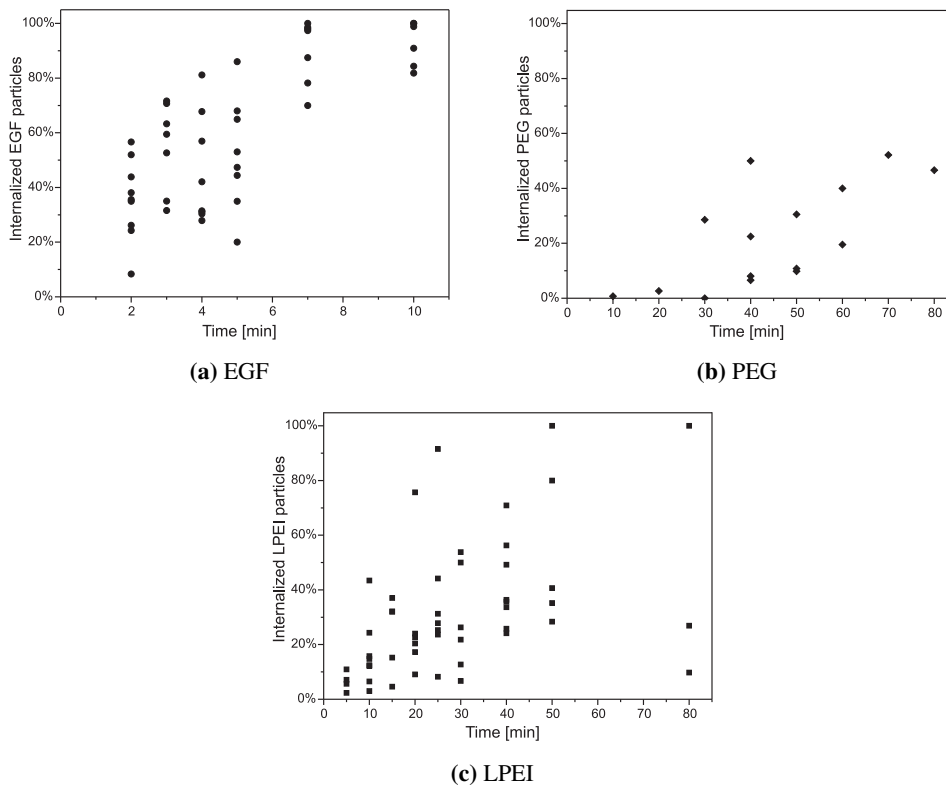**(a)** EGF

(b) PEG

(c) LPEI

Figure 4.6: Percentage of internalized particles as determined by means of quenching experiments at different time points. For EGF particles an extremely fast internalization is observed, occurring on a time scale of minutes. PEG particles are internalized very slowly: after 80 minutes, less than 60% of the particles are internalized. LPEI particles are also internalized slowly. The spread on the data is explained in the text.

Figure 4.6a shows the internalization kinetics of EGF particles. Internalization occurs within a few minutes. Already 50% (median value) of the cell surface-associated particles were internalized after 5 minutes, reaching 91% (median value) internalization after 10 minutes. This extremely fast internalization is in good agreement with earlier observations for the uptake kinetics of free EGF internalization. Haigler et al. described localization of EGF in vesicles after 2.5 minutes [69] and a start of EGF internalization after 1.5 minutes was shown by Baulida et al. [163].

In contrast, PEG particles showed a very slow internalization (figure 4.6b). After 80 minutes, less than 60% of the particles were internalized. As described in section 3.6, the quenching of large PEG particles was not unambiguous. Often, only partial quenching was observed. This may explain the large spread on the data. As mentioned in section 4.1 the shielding of LPEI by PEG was not complete. Therefore partly shielded PEG particles may still bind to the membrane by means of the unshielded LPEI molecules. This introduces a bias into the measurements towards partly shielded PEG particles and thus the percentage of internalized

PEG particles may actually be smaller.

For LPEI particles (figure 4.6c), the spread is even larger than observed for PEG particles. After 25 minutes, the internalization percentage varied from 90% to less than 10%. This huge spread can be explained by three different factors. The relevance of these factors increases with time.

First, after pipetting the polyplexes onto the cell surface and subsequent attachment, a medium change was performed. This medium change should produce a clear starting point and prevent particles to settle down during the measurement which would distort the percentage of internalized particles at a defined point in time. Although the medium change may have removed the majority of particles in the medium, a minority could still have been able to settle down after diffusing in the medium for some time. These particles could not be excluded from the measurements because due to computer memory constraints it was not possible to follow the particles continuously during more than 20 minutes. Particles that settled down onto the cell surface later could not be distinguished from particles that were present on the membrane from the beginning. These particles would lead to a bias towards extracellular particles.

Second, the amount of internalized particles is dependent on the region of the cell. Before internalization, particles are attached and distributed evenly over the cell membrane. After being internalized, particles are transported from the cell periphery towards the cell nucleus thus concentrating internalized particles in this region. The percentage of internalized particles in a region containing the cell periphery is therefore lower than in a region close to the nucleus. Since it is impossible to image all particles in one cell, the calculated percentage of internalized particles is dependent on the focal plane of the microscope.

A third factor influencing the spread on the data is fusion of particle-containing endosomes after internalization. After internalization, particles are present in endosomes. Fusion of these endosomes reduces the number of distinguishable particles inside the cell, since several particles are present in the same endosome, but cannot be detected individually. Calculation of the percentage of internalized particles will in this case yield too low a percentage.

Overall, these data show that EGF and PEG particles differ dramatically in their internalization kinetics. Whereas 91% of the EGF particles is internalized after 10 minutes, less than 60% PEG particles is internalized after 80 minutes. This can be explained by difference in duration of phase I, observed in section 4.2. It brings us back to the main question of the chapter and shows that targeting of a gene vector to a receptor markedly increases the efficiency of internalization.

4.5   Analysis of the three different phases

Although in section 4.3 we saw that internalization takes place during phase I, the cellular context of the different phases is still unclear. In this section the three different phases are analyzed by means of mean square displacement (section 3.5.1), which enables a physical description of the phases.
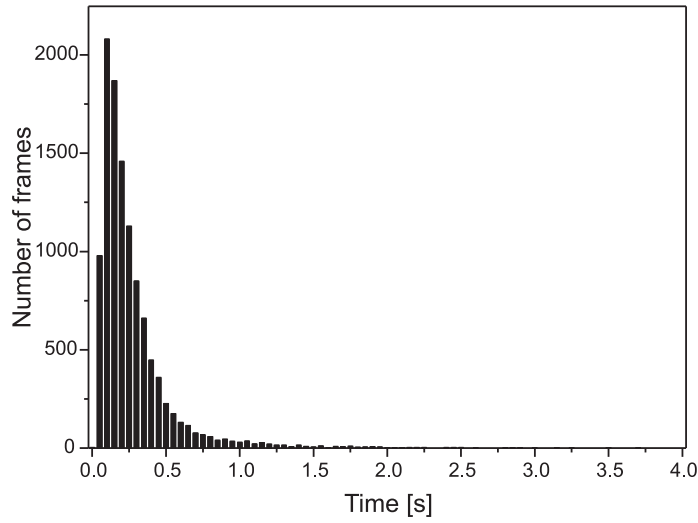
Figure 4.7: Histogram of the instantaneous velocities during phase I generated from 10 EGF particle trajectories. Phase I is characterized by a low instantaneous velocity typically below $v = 0.5$ μm/s. The distribution contains a maximum at $v = 0.1$ μm/s.

4.5.1 Phase I

At the end of section 4.2 a definition was given for the three phases observed in section 4.2.1. Phase I was defined as containing no more than 5 successive steps with an instantaneous velocity above $v = 0.5$ μm/s. Over 100 EGF, PEG and LPEI trajectories were divided into different phases, according to the aforementioned definition. For each phase a histogram was produced depicting the number of frames with a specified instantaneous velocity within a bin size of 0.05 μm/s. For phase I, the resulting distribution is presented in figure 4.7. It is characterized by a narrow velocity profile with a maximum in the distribution at $v = 0.1$ μm/s.

Phase I was further analyzed by plotting the mean square displacement (MSD) $\langle r^2 \rangle$ versus time Δt. (For a detailed description of mean square displacement see section 3.5.1.) In figure 4.8, the MSD plots of phase I of 10 representative EGF trajectories are displayed. The MSD plot for the trajectory shown in figure 4.2a is included and is distinguishable as a dotted curve. The plots show a quadratic dependence of $\langle r^2 \rangle$ on Δt, indicating directed motion. Fitting equation 3.5 to the data and averaging the obtained values for the 10 trajectories results in a mean drift velocity $v_{\mathrm{I}} = 0.015 \pm 0.003$ μm/s and a mean diffusion coefficient $D_{\mathrm{I}} = 4 \cdot 10^{-4} \pm 4 \cdot 10^{-4}$ μm²/s. The large standard deviation is a result of the broad spread of the diffusion coefficients from curve to curve in figure 4.8. For a single curve the diffusion coefficient can be calculated much more accurately.
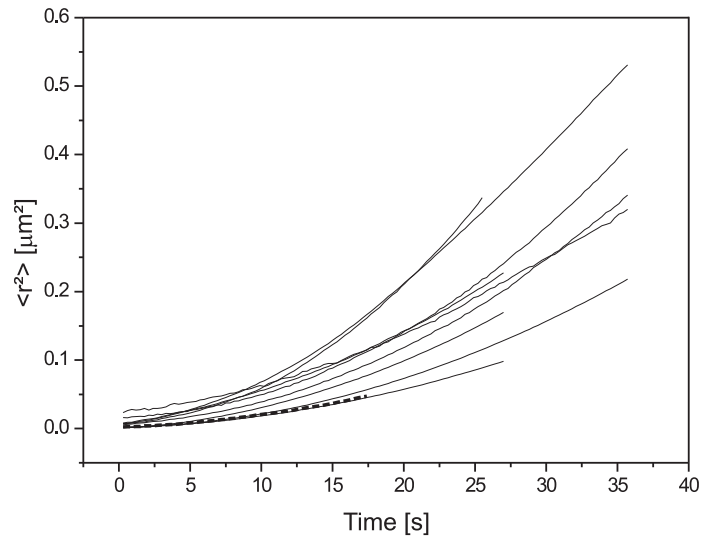
Figure 4.8: MSD analysis of phase I motion. Phase I parts of trajectories were selected by the criterion that they contain no more than 5 successive steps with an instantaneous velocity above $v = 0.5$ μm/s. The MSD plots of 10 representative EGF trajectories are plotted including the trajectory from figure 4.2a (dotted). The quadratic dependence of $\langle r^2 \rangle$ on Δt indicates a directed component.
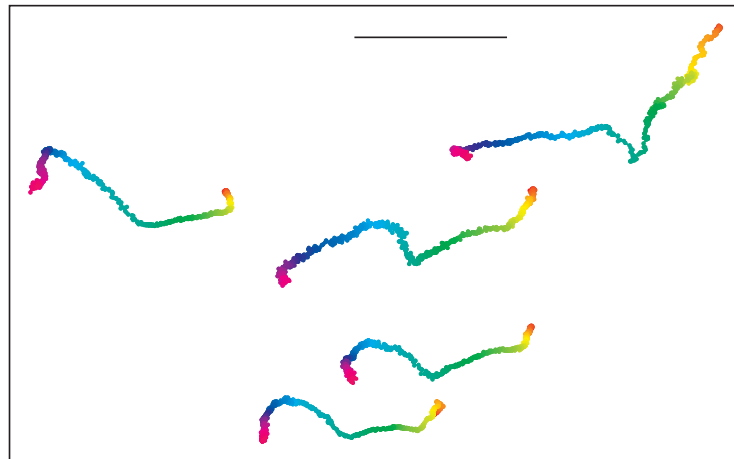

Figure 4.9: Multiple particle tracking of five LPEI particles. Particles were tracked for 422 s with an acquisition time of 500 ms. The trajectories start immediately after the particles attached to the cell surface. The color of the trajectory is shown as changing from red through green to blue with progressing time. Correlated movement is illustrated by the simultaneous bending of the trajectories. Scale bar: 4 μm.
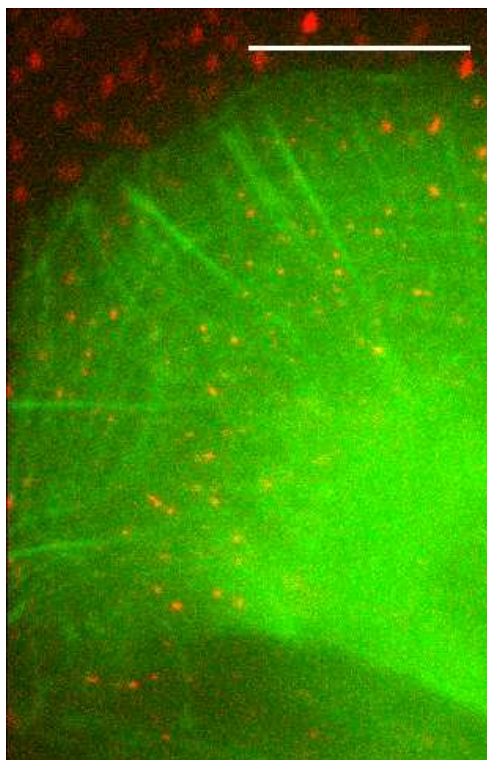
Figure 4.10: PEG particles on an actin-GFP expressing cell. The particles are represented in red, the actin cytoskeleton is shown in green. The cell nucleus is located in the bottom right corner of the image. Scale bar: 20 μm.

The question now arises what the origin of the directed movement during phase I is. An indication as to what the answer might be can be found by looking at several particles on the same cell simultaneously. The movement of particles on the same cell shows strong directional correlation, which can be demonstrated by tracking several polyplexes in proximate vicinity. Five trajectories of particles in close vicinity are presented in figure 4.9. The color of the trajectory changes with progressing time from red to blue for a total duration of 7 minutes. The trajectories show highly correlated motion patterns concerning both the form as well as the temporal coincidence of directional changes. All trajectories show the small steps characteristic for phase I. The directional and temporal correlation of the movement is illustrated by the simultaneous bending of the trajectories and indicates that phase I movement is not caused by independent movement of single particles.

As seen in the last paragraph there must be a common factor that influences the movement of all particles. Additional experiments with actin-GFP expressing cells revealed that the actin cytoskeleton played a major role in the movement during phase I. In the obtained video sequences particles moved in correlation with the retrograde actin flow. This can easily be recognized in a movie, of which one frame is shown in figure 4.10. The figure shows PEG particles, represented in red, on an actin-GFP expressing cell, shown in green. Thin actin fibers parallel to the cell edge and perpendicular to the radial stress fibers can be recognized. In the original movie a correlation of the movement of these fibers with the particles' movement was observed. This suggests that the correlated particle movement during phase I is the result of concerted movement of particles bound to the underlying cortical actin network through transmembrane proteins.

In short, the observations of phase I amount to the following: it consists of instantaneous velocities around $v = 0.1$ μm/s, the mean square displacement shows that a directed and a diffusional component is present, and a correlation of neighboring particles and actin cytoskeleton is observed. At the beginning of phase I particles are still on the cell membrane, but they are internalized during phase I. The correlated movement of polyplexes and local actin structures (figure 4.10) suggests that the directed movement of the polyplexes is attributed to the constant movement of the retrograde actin flow with velocity $v_I = 0.015 \pm 0.003$ μm/s (for EGF particles). A diffusional component is observed superimposed onto this flow with a diffusion coefficient of $D_I = 4 \cdot 10^{-4} \pm 4 \cdot 10^{-4}$ μm^2/s which might represent the lateral diffusion of the ligand-receptor complex in the cell membrane.

For EGF particles the *directed* component observed in the MSD plot can be interpreted as follows. The EGF receptor is directly linked to the actin cytoskeleton via its cytoplasmic site where an actin-binding sequence is present [166]. This results in a direct colocalization of EGF particles with the actin cytoskeleton and the measured velocity is most probably the velocity of the retrograde actin flow. In case of LPEI particles, Bausinger et al. [156] observed a similar actin-mediated behavior with a velocity of $v = 0.01$ μm/s. A connection between PEI particle-binding HSPGs and actin was suggested by Kopatz et al. [150]. Moreover, it was shown for membrane glycoproteins that their movement is driven by the actin cytoskeleton rather than by the lipid flow [167]. The velocity observed in our study is well in accordance with velocities reported for endocytosed latex beads that showed an actin-mediated retrograde flow with an average velocity of $v = 0.016$ μm/s and for gold particles bound to cell surface glycoproteins [167, 168]. These values confirm the interaction of a polyplex-bound HSPG with the actin cytoskeleton. The particles are thus transported by the flow of the underlying cortical actin network after binding to cell surface receptors.

The *diffusional* component may be explained by diffusion of plasma membrane components to which the particle is bound. In case of EGF particles the diffusion coefficient of $D_I = 4 \cdot 10^{-4} \pm 4 \cdot 10^{-4}$ μm^2/s is ten times lower than the diffusion of GFP-coupled EGF receptors on the cell surface measured by Keating et al. [169]. The difference may be caused by the particle binding to the receptor, which induces clustering of the EGF receptors (see section 4.1) and may hinder the diffusion of the receptor on the cell membrane. The measured diffusion coefficient is also in good agreement with Bausinger et al. [156] ($D = 2 \cdot 10^{-4}$ μm^2/s) who suggests that the diffusion represents the motion of the HSPGs in the membrane. This is
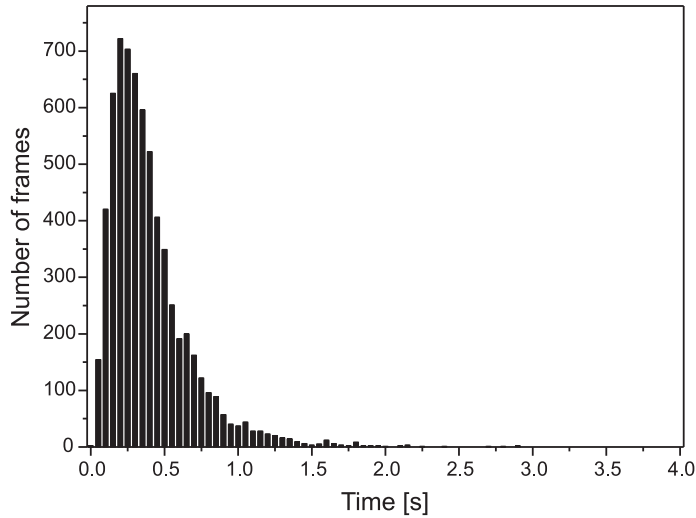
Figure 4.11: Histogram of the instantaneous velocities during phase II generated from 13 EGF particle trajectories. In phase II the instantaneous velocity is increased compared to phase I with a maximum of the distribution at $v = 0.2$ μm/s.

supported by the diffusion coefficient of $D \approx 2 \cdot 10^{-4}$ μm^2/s for glycoprotein-bound gold particles in the cell membrane reported by Sheetz et al. [167].

Finally, one last question remains to be answered. Why do we see phase I movement before *and* after internalization? This can be explained by the high density of actin fibers directly underlying the cell membrane. After "pinching off" from the membrane, the endocytic vesicle is entrapped in the cortical actin network and its movement is still correlated with the retrograde actin flow. Thus, the vesicle may need some time to escape this network.

4.5.2 Phase II

At the end of section 4.2 phase II was defined as the intermediate period between phase I and phase III with instantaneous velocities in average above $v = 0.5$ μm/s. As for phase I, a distribution of the instantaneous velocities was obtained by analyzing different trajectories and is presented in figure 4.11. Compared to phase I, the maximum of the distribution is shifted towards a higher velocity, in this case at $v = 0.2$ μm/s, and the distribution is broadened.

The MSD analysis of phase II is presented in figure 4.12. The mean square displacement of 13 representative trajectories was plotted versus time. The MSD plots show normal diffusion (Brownian motion) at the beginning for small Δt and often asymptotic behavior for larger Δt. This asymptotic behavior indicates confined diffusion. The diameters of these confinements were calculated by fitting equation 3.6 to the data. The obtained diameters range from 0.3 μm up to 2.0 μm. As stated in section 3.5.1, the detection of confined diffusion requires a minimal duration of phase II. Therefore, not all MSD plots in figure 4.12 show the characteristic
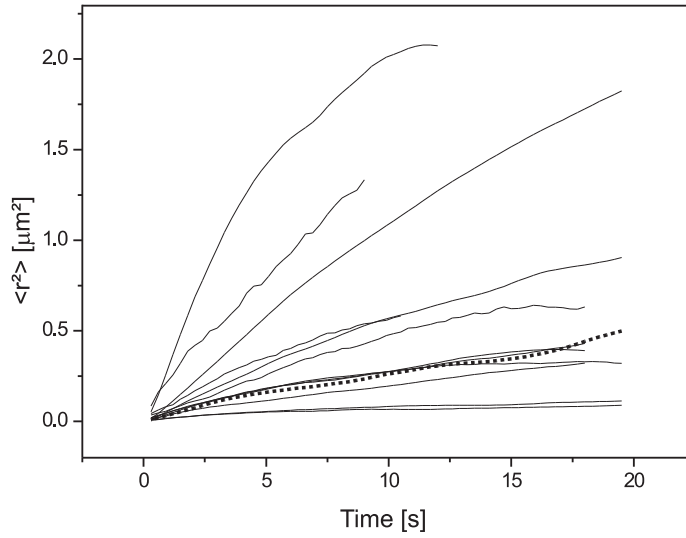
Figure 4.12: MSD analysis of phase II motion. Phase II parts of trajectories were defined as following phase I and showing instantaneous velocities in average above $v = 0.5$ µm/s. 13 representative EGF trajectories were analyzed including the trajectory from figure 4.2a (dotted). The plots mostly show asymptotic behavior for large Δt indicating confined diffusion. The linear dependence of $\langle r^2 \rangle$ on Δt of the dotted line indicates normal diffusion.

asymptotic behavior. The dotted line for example, corresponding to the polyplex trajectory shown in figure 4.2a, shows a linear dependence of $\langle r^2 \rangle$ on Δt, indicating normal diffusion with a diffusion coefficient of $D_{\mathrm{II}} = 5.6 \cdot 10^{-3}$ µm²/s.

Since the particles have already been internalized in phase I (section 4.3), the confined diffusion results from local microenvironments in the cytoplasm experienced by the endosome containing the particle. The network of cytoskeletal filaments, large macromolecules and cytoplasmic organelles may act as local obstacles for free diffusion [170]. The obtained confinements of 0.3–2.0 µm in diameter are within the typical range for confinements in the cytoplasm [171]. The "cage" sizes show a broad distribution as the size of the confinements is strongly dependent on the location of the particle or vesicle within the cell. The restricted diffusive mobility of larger structures such as vesicles enforces active transport in order to bridge larger distances within the cell. Phase II can therefore be regarded as a lag phase after internalization until a microtubule track for active transport is found.

A good example of barriers in the cytoplasm and therefore of confined diffusion is presented in figure 4.2b. Here, the confinement is clearly recognized. The endosome is moving mainly parallel to one axis; in other directions the movement of the endosome is hindered, probably by actin structures.
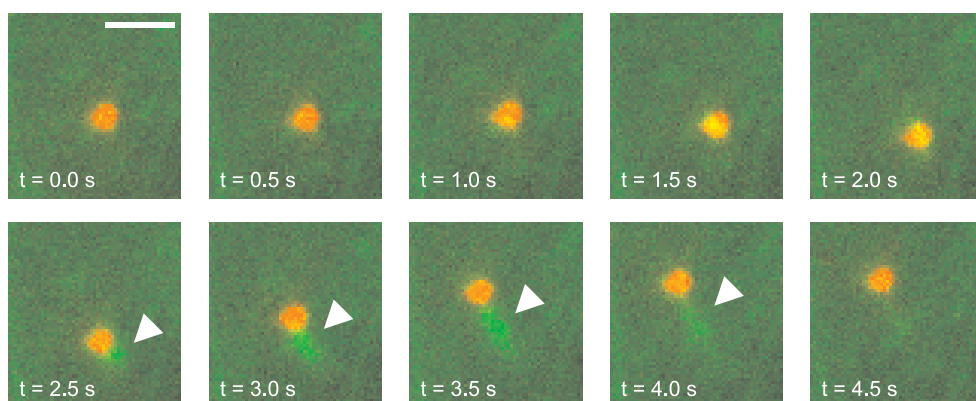
Figure 4.13: Formation of an actin tail. 10 consecutive images from a movie are shown representing the colocalization of a PEG particle (red) and actin (green). At first a local increase in the amount of actin is observed at the site of the particle, visible in the images as a yellow spot. After 2.5 seconds an actin tail is formed (arrowhead) which presumably pushes the particle in the direction of the cytosol. Scale bar: 2 μm.

Interestingly, when using actin-GFP expressing cells, sometimes colocalization of a particle and an actin tail was observed. In figure 4.13 several consecutive images from a movie are presented showing the formation of an actin tail. The particle is presented in red, actin is presented in green. First, colocalization is observed between the particle and actin. After 2.5 seconds an actin tail is observed which by actin polymerization presumably pushes the particle in the direction of the cytosol. The colocalization of actin and particle generally lasted for 30 to 60 seconds and was only observed for a small proportion of the polyplexes. Actin tails are a well-known mechanism for, e.g., intra- and intercellular transport of Listeria in bacteria [172]. They have also been observed to facilitate the internalization of the SV40 virus [173] and they are known to play a role in the transport of endosomes towards the cytosol [174, 175]. By means of a burst of actin polymerization, the endosome is propelled in the direction away from the cell membrane.

4.5.3 Phase III

Phase III was defined as containing at least 16 successive steps in the same direction (section 4.2). As for phase I and II, a distribution of the instantaneous velocities was generated and presented in the histogram in figure 4.14. A large increase in instantaneous velocity compared to phase I and phase II is visible. Peak velocities up to 4 μm/s were detected and the peak distribution is broader than in phase II.

Figure 4.15 presents 21 representative MSD plots of EGF particles for phase III including the trajectory from figure 4.2a (dotted line). The plots show a quadratic dependence of $\langle r^2 \rangle$ on Δt indicating directed motion. Fitting equation 3.5 to the data and averaging these values, a mean velocity of $v_{III} = 0.7 \pm 0.4$ μm/s was obtained and a mean diffusion coefficient $D_{III} = 0.1 \pm 0.1$ μm^2/s.
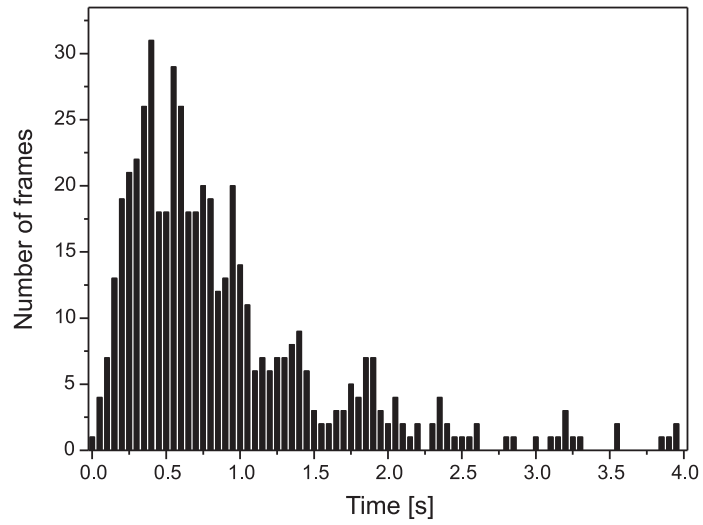
Figure 4.14: Histogram of the instantaneous velocities during phase III generated from 21 EGF particle trajectories. During phase III, rapid directed motion was detected with a broad distribution reaching its maximum around $v = 0.5$ μm/s and peak velocities of $v = 4$ μm/s.
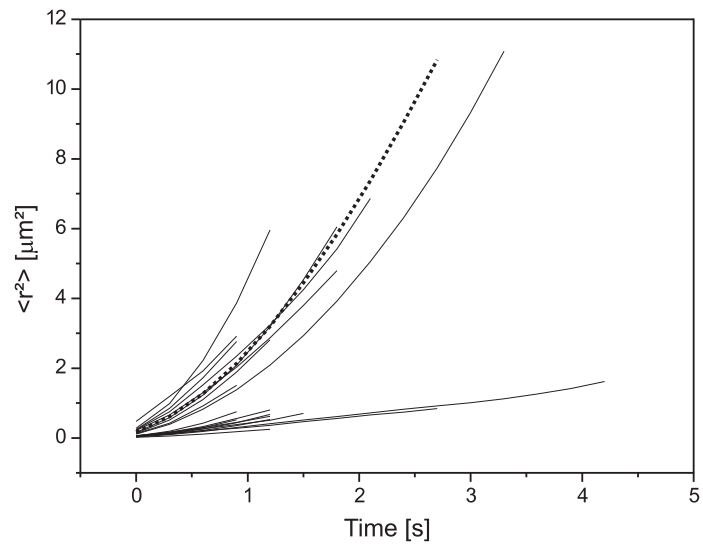

Figure 4.15: MSD analysis of phase III motion. Phase III parts of trajectories were selected by the criterion that they contain at least 16 successive steps in the same direction. 21 MSD plots of PEG trajectories including the one from figure 4.2a (dotted) are shown. The plots show a quadratic dependence of $\langle r^2 \rangle$ on Δt indicating directed motion.

Typically, directed motion was observed for periods of 5 to 15 seconds and was frequently alternated with phases of (confined) diffusion. Particles also stopped during directed motion, changed their direction and moved back and forth on the same track before resuming their original direction. Those alterations during directed motion resulted in an overall stop-and-go motion of the particles. An example of this is visible in figure 4.2a. Directed motion is first interrupted by diffusion (upper arrow head) and then by back-and-forth movement (lower arrow head). Treatment of the cells with nocodazole, a microtubule-disrupting drug, resulted in inhibition of phase III motion.

The interpretation of phase III motion is straightforward. Inhibition of the movement by nocodazole indicates that particles are connected to the microtubule network during phase III. The observed bidirectional transport showed stop-and-go motion characteristic for transport along microtubules [176]. Active transport of LPEI particles along microtubules has been shown before [156]. The mean velocity of $v_{III} = 0.7 \pm 0.4$ µm/s observed in this study is within the range for active transport by kinesin and dynein along microtubules [177]. Suh et al. observed active transport of LPEI particles with a velocity of $v = 0.2$ µm/s [178], but did not show the direct relation to transport on microtubules. Their average velocity for active transport includes stop phases with $v \approx 0$ and may therefore be reduced compared to the actual transport velocity. The same holds for the study of Bausinger et al., who obtained an average velocity of $v = 0.19$ µm/s. In contrast, in our calculations stop phases within the trajectories were excluded. The resulting average velocity is therefore closer to the values reported for active transport by kinesin and dynein. In short, these considerations give strong evidence that phase III represents active transport along microtubules.

Typically, all three phases were observed for EGF, PEG as well as LPEI particles displaying values for D and v in the same range. However, for many PEG and LPEI particles only one or two phases were distinguishable during the observation time while the phase order always remained unchanged. Differences between the particle types were only observed concerning the duration of phase I. For EGF particles, the duration of phase I was considerably shorter, lasting only a few minutes, whereas for PEG and LPEI particles it was sometimes observed for more than one hour. For the particles analyzed, no difference was observed in the duration of phase II (normal and confined diffusion) and phase III (directed motion).

4.6 Summary

In this chapter the internalization dynamics and kinetics of EGF, PEG and LPEI particles was examined. Combining trajectories and instantaneous velocity plots, the internalization process of polyplexes can be differentiated into three different phases. A biological interpretation of these phases could be given after analysis by means of quenching experiments and mean square displacement.

The first phase starts directly after attachment of the particle on the cell membrane. It consists of a directed and a diffusional component. The directed component amounted to $v_I = 0.015 \pm 0.003$ µm/s. Since particles showed correlated movement and colocalization with actin was observed, the directed component is most probably resulting from the movement of the actin cytoskeleton to which the EGF receptor and HSPGs are bound. The diffusional

component of $D_I = 4 \cdot 10^{-4} \pm 4 \cdot 10^{-4}$ μm²/s represents the motion of the receptor (EGFR in case of EGF particles, HSPG for LPEI and probably PEG particles) on the cell surface. Quenching experiments showed that during phase I internalization occurs.

Phase II starts with an increase in instantaneous velocity which may represent the escape of the particle from the cortical actin network. This phase is characterized by normal and later confined diffusion within the cytosol. The diffusion is limited by local macromolecules or proteins in the cytosol. The confinements showed sizes of 0.3–2.0 μm in diameter.

An abrupt increase in instantaneous velocity and clear directionality characterizes the beginning of phase III. The directed motion is alternated with short stop phases, representing characteristic stop-and-go motion along microtubules. The directed motion during phase III had a velocity of $v_{III} = 0.7 \pm 0.4$ μm/s and was inhibited by addition of nocodazole.

A difference between the three particles was only observed in the duration of the first phase. EGF particles showed phase I movement for some minutes, for PEG and LPEI particles this phase could take more than one hour. This is related to the difference in internalization percentages. The percentage of internalized EGF particles reached 50% within 5 minutes and more than 90% within 10 minutes, whereas PEG and LPEI particles showed an extremely large spread but rarely more than 80% internalization, even after 80 minutes.

These results show that targeting of polyplexes by means of a ligand leads to faster and more efficient internalization as compared to untargeted particles.

5. Photoinduced endosomal release of polyplexes

In the last chapter we have seen how polyplexes overcome the barrier of the cellular membrane. In this chapter we examine the next hurdle a vector encounters on its way to the nucleus: the escape from the endosome. As we have seen already, polyplexes are internalized by endocytosis and are therefore present in endosomes in the cell. Vectors that do not escape from the endosome end up in lysosomes. Since in lysosomes the DNA is degraded and is thus obviously not available for transcription in the nucleus, different techniques to induce endosomal escape are under investigation. Examples to induce vector escape from endosomes are functionalized vectors with pH-sensitive peptides or polymers that destabilize the endosomal membrane at the low pH prevailing in late endosomes [7]. For this technique, a change in vector synthesis is needed to implement the membrane-disrupting properties.

A vector-independent method developed by Berg et al. [179] employs photoactive compounds for disruption of endosomal membranes. The mechanism by which photoactive compounds induce endosomal escape is described in detail in section 2.5.2. In short, the photoactive compound binds to the cell membrane and is endocytosed together with the vector. Upon illumination with light of a defined wavelength, the photosensitizer becomes activated and the cell membrane is damaged enabling escape of the vector. Studies using fluorescent probes showed a change in distribution of the endosomal cargo within the cell before and after the activation of a photosensitizer and suggest successful endosomal damage and cargo release [179–181]. In addition, transfection studies with photoactive compounds showed enhancement in gene expression most probably due to improved release of the gene vector [17–19]. Photochemical release of gene vectors has also been implemented *in vivo* [181–183].

The detailed mechanism of endosomal release induced by photoactive compounds has not yet been unraveled. In this chapter, the endosomal release induced by activation of disulfonated *meso*-tetraphenylporphine with the sulfonate groups on adjacent phenyl rings ($TPPS_{2a}$) is imaged in real time using fluorescence microscopic methods. First the absorption and fluorescence characteristics of $TPPS_{2a}$ are determined. This provides information on the photophysical processes of $TPPS_{2a}$. Then, the visualization of endosomal release by means of microscopic methods is confirmed by the endosomal release of a fluorescent fluid phase marker, Alexa Fluor Dextran (AFD). Afterwards, the release of polyplexes is visualized.

Three different classes of polyplexes were examined. The first class consists of polyethyleneimine (LPEI) polyplexes. As described in section 2.5.1 LPEI polyplexes have a high buffering ability that prevents trafficking to lysosomes. Therefore, no degradation of the parti-
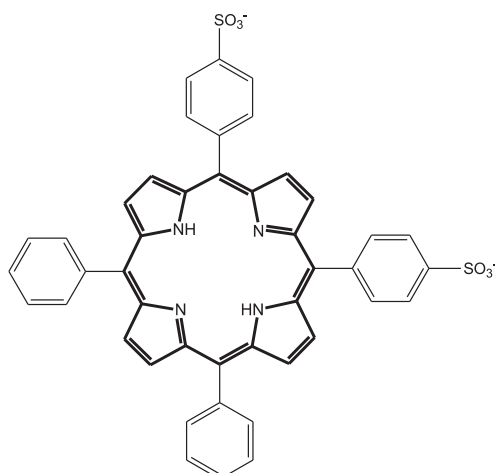
Figure 5.1: Chemical structure of disulfonated *meso*-tetraphenylporphine with the sulfonate groups on adjacent phenyl rings (TPPS$_{2a}$). The inner (bold) structure represents the chemical structure of a porphyrin.

cles before endosomal release is expected. The second class comprises polyplexes consisting of DNA condensed by poly-L-lysine (PLL). Together with the third class (DNA condensed with the stereoisomer poly-D-lysine (PDL)) it does not show buffering ability and both particles end up in lysosomes. Whereas PLL is biodegradable by peptidases in the lysosome because of its L-lysine residues, its stereoisomer PDL is nonbiodegradable.

By means of fluorescence widefield microscopy with high temporal resolution the photoinduced endosomal release of all three particles was visualized. Release characteristics such as mobility in the cytoplasm, degradation of the particles, and dissociation of polymer and DNA are discussed and related to biodegradability, buffering capacity, and condensation strength of the polymer.

5.1 Characterization of TPPS$_{2a}$

The chemical structure of TPPS$_{2a}$ is shown in figure 5.1. TPPS$_{2a}$ belongs to the class of porphyrins. Porphyrins contain a large, highly delocalized π system, resulting in a small energy gap between the highest occupied molecular orbital (HOMO) and the lowest unoccupied molecular orbital (LUMO). Thus, absorption bands of porphyrins lie in the visible and near UV regions of the spectrum [184, p.90]. Around 600 nm porphyrins typically show several absorption bands, representing absorption from the S_0 into the S_1 state [185]. In the region 400–450 nm a broad absorption band (called Soret band) is present which represents absorption from the S_0 into the S_2 state. Thus, from the S_0 state, transitions into the S_1 and the S_2 state are possible. From the S_2 state the molecule can show radiationless decay to the S_1 state, but also electron transfer from the S_2 state was observed [185]. From the S_1 state fluorescence can occur, or through intersystem crossing (ISC) a transition from the S_1 state to the T_1 state is possible.
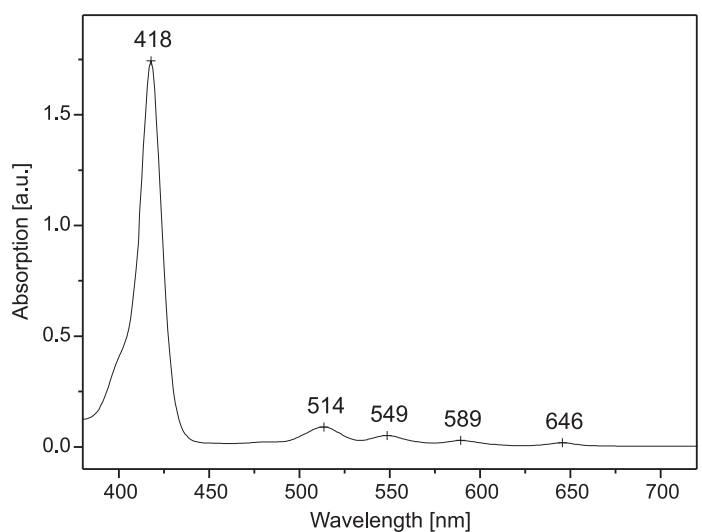
(a) Absorption spectrum
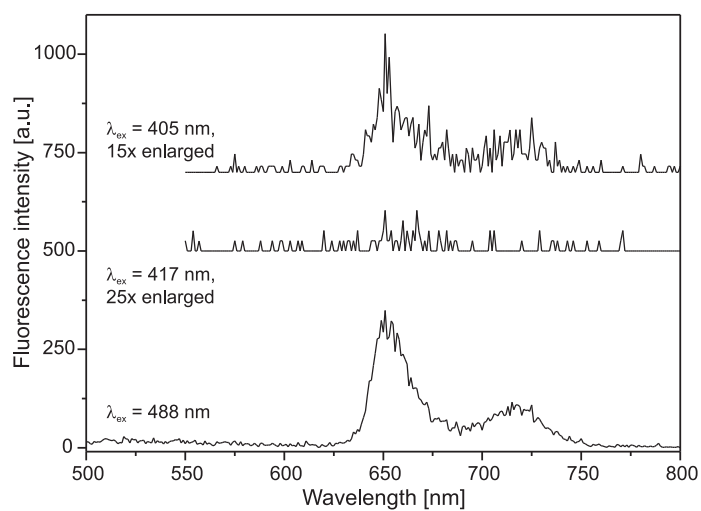
(b) Emission spectra

Figure 5.2: Absorption and emission spectra of TPPS$_{2a}$ dissolved in DMEM-F12 cell culture medium. A maximum in absorption is observed at 418 nm. Emission spectra were recorded with excitation at 405 nm, 417 nm and 488 nm. For excitation at 405 nm two weak fluorescence peaks are observed around 650 nm and 720 nm. Very weak fluorescence is observed for excitation with 417 nm and for 488 nm excitation two clear peaks are distinguished at 651 nm and 715 nm.

In general, porphyrins show a high quantum yield for triplet state formation [186] and thus long triplet lifetimes. The triplet state can be deactivated by phosphorescence, but in addition bimolecular deactivation mechanisms are possible involving the transfer of excitation energy from one molecule to another. The latter process is called quenching.

Molecular oxygen (O_2) has a triplet ground state $^3\Sigma_g^-$ and a low energy gap separates the triplet state from the lowest excited (singlet) state [187]. The long triplet lifetimes of porphyrins, in combination with the low excitation energy of molecular oxygen give excellent conditions for bimolecular deactivation processes of porphyrins and molecular oxygen, which lead to the production of singlet oxygen. Tetraphenylporphine (TPP) is known to have a high oxygen quenching constant of $1.42 \cdot 10^9$ dm^3 mol^{-1} s^{-1} [186] and is correspondingly a very efficient singlet oxygen generator. The mechanism of singlet oxygen generation by quenching of triplet state sensitizers is described in detail in the publications of Schmidt et al. and Mehrdad et al. [187, 188].

Figure 5.2a presents the absorption spectrum of TPPS$_{2a}$. It was recorded on a Perkin Elmer 330 absorption spectrometer. The maximum of the Soret band is observed at 418 nm. Further absorption bands are visible at 514 nm, 549 nm, 589 nm and 646 nm. As explained above, the broad Soret band corresponds to absorption from the S_0 state into the S_2 state. The weaker bands at lower energy represent absorption from the S_0 into the S_1 state.

Emission spectra of TPPS$_{2a}$ with excitation at 405 nm, 417 nm and 488 nm are presented in figure 5.2b and were recorded on a FS900 fluorescence spectrometer (Edinburg Instruments). All spectra were recorded under exactly the same conditions with the same scan speed and step width. Excitation by 405 nm shows two small fluorescence peaks at 650 nm and 720 nm. Since 405 nm lies within the Soret band, TPPS$_{2a}$ is expected to be excited into the S_2 state. Apparently, at least part of the population falls back into the S_1 state whereupon fluorescence is observed. The region of this fluorescence is in agreement with measurements on unsulfonated *meso*-tetraphenylporphyrine [189].

Excitation of TPPS$_{2a}$ by 417 nm shows very weak fluorescence around 650 nm. The reason why this fluorescence band is smaller than the band due to excitation with 405 nm light is not fully understood. The absorption at 417 nm most probably excites the molecule from its S_0 state into the S_2 state. The fact that only weak fluorescence is visible, suggests that at this excitation wavelength excited singlet TPPS$_{2a}$ is very efficiently converted to its triplet state from which either phosphorescence occurs or quenching by molecular oxygen.

Excitation of TPPS$_{2a}$ at 488 nm excitation shows a clear peak at 651 nm and 715 nm. Transition to the triplet state is probably not efficient in this case.

5.2 Endosomal release of AFD

In order to test whether endosomal release could be visualized in real time by microscopical methods, the release of a fluid phase marker, Alexa Fluor Dextran (AFD), was studied prior to endosomal release of polyplexes. Alexa Fluor Dextran is a 10 kDa dextran, a hydrophilic polysaccharide, and is internalized into the cell by means of fluid phase endocytosis [190]. The dextran is labeled with the Alexa Fluor 488 dye, which has an absorption maximum at 495 nm and an emission maximum at 519 nm [191].
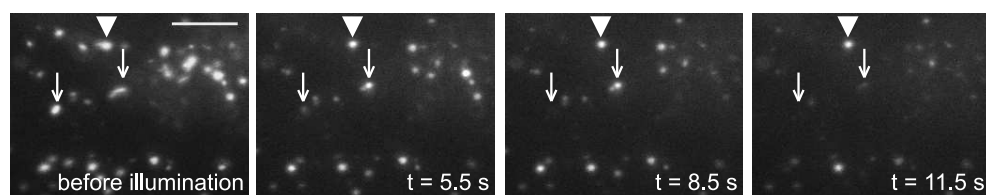
Figure 5.3: Four selected frames of a video stream (acquisition time: 500 ms). The first frame shows the cell with AFD-loaded endosomes before 405 nm illumination. Subsequent images are shown 5.5 s, 8.5 s, and 11.5 s after the start of 405 nm illumination. A successive disappearance of fluorescent endosomes was observed (arrows) after photosensitizer activation. A minority of endosomes showed constant fluorescence intensity without detectable intensity decrease (arrowhead). Scale bar: 5 μm.

HUH7 WT cells were seeded 48 hours before measurement in a density of $1.0 \cdot 10^4$ cells per well, on a collagen A-coated LabTek chambered cover glass. After 24 hours, the medium was changed in the dark to medium containing 0.025 μg/ml TPPS$_{2a}$ and 0.024 mg/ml AFD. Control cells were incubated with medium containing only AFD. In this way, the endosomal compartments were loaded with AFD, and TPPS$_{2a}$ was incorporated into the corresponding membranes. Excitation of the photosensitizer with 405 nm light should damage preferentially intracellular membranes with incorporated TPPS$_{2a}$, in particular endosomes loaded with the coincubated AFD. 12–16 hours later the cells were washed three times in the dark with CO$_2$-independent medium to remove residual TPPS$_{2a}$. Since illumination of the cells should be avoided, the samples were handled in aluminium foil before measurement and subsequently placed on a heated microstage (37°C) and imaged. For excitation of AFD, the 488 nm laser line was used. In the following, the time printed on the images always represents the time elapsed since the start of the 405 nm illumination.

The effect of photosensitizer activation on a cell preincubated with AFD and TPPS$_{2a}$ is presented in figure 5.3. The figure depicts four selected frames from a movie recorded with an acquisition time of 500 ms. The bright, fluorescent spots represent endosomes filled with AFD. The first frame shows endosomes before activation of the photosensitizer. Illumination with 405 nm laser light for 5 seconds resulted in successive disappearance of the fluorescence signal of single AFD-loaded endosomes visible in the following frames. The exact time point of disappearance varied for individual endosomes. Interestingly, the fluorescent signal of individual spots decreased in one sudden step (see arrows).

For a minority of AFD-loaded endosomal structures no decrease in fluorescence intensity was observed, even after prolonged illumination with 405 nm light (see arrowhead). Presumably, those structures did not incorporate TPPS$_{2a}$ in amounts sufficient for membrane disruption.

(a) Without photosensitizer
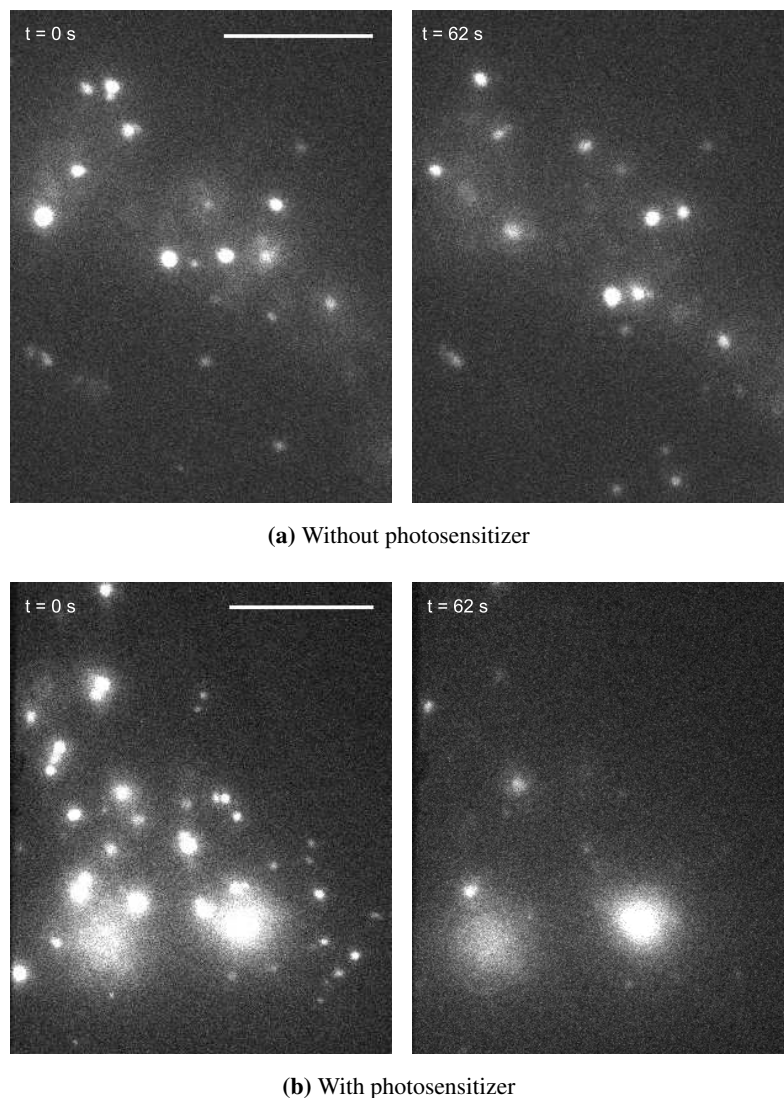

(b) With photosensitizer

Figure 5.4: Four selected frames from two different video streams (acquisition time: 70 ms). Both video streams are recorded under exactly the same experimental conditions and camera settings. Cells were incubated with AFD and without (a) or with (b) TPPS$_{2a}$. The first image shows the cell immediately after start of 405 nm illumination, the next image was taken 62 s afterwards. (a) No difference is observed in the amount of fluorescent endosomes. (b) The TPPS$_{2a}$-treated cell shows a strong reduction in the amount of fluorescent structures. Scale bar: 10 μm.

To exclude the possibility of bleaching of the dye by laser light, control experiments with cells incubated with photosensitizer-free medium were performed. For these cells different behavior was detected. Upon illumination with 405 nm laser light no sudden disappearance of fluorescent spots was observed. Under imaging conditions where a reduction in the amount of fluorescent structures was observed for a TPPS$_{2a}$-treated cell, fluorescent structures remained visible in control cells.

In figure 5.4 an example of a cell incubated with photosensitizer free medium is compared with a TPPS$_{2a}$-treated cell. For both examples, two images from a video sequence are presented. Both video sequences were recorded under exactly the same experimental conditions and with the same camera settings. The images are taken directly at the beginning of the 405 nm illumination period and 62 seconds after start of 405 nm illumination. No decrease in the amount of fluorescent structures is observed for the cell incubated with photosensitizer free medium (figure 5.4a), whereas the images representing the TPPS$_{2a}$-treated cell show a clear reduction in the amount of fluorescent structures. This confirms that the disappearance of fluorescent spots is not due to bleaching of the Alexa dye by laser illumination, as bleaching by the laser should be visible in both cases.

To further ensure that the sudden disappearance of fluorescent structures was indeed restricted to the activation of photosensitizer and subsequent endosomal release the interaction between TPPS$_{2a}$ and AFD was studied. A mixture of TPPS$_{2a}$ and AFD was imaged on a cover slip under the same experimental conditions used for the aforementioned experiments. No quenching effect or inactivation of the fluorescent AFD was observed.

In some cases, the disappearance of fluorescent spots after excitation of TPPS$_{2a}$ was accompanied by an increase in cytosolic fluorescence. In figure 5.5 the first and 50th frame (corresponding to a temporal separation of 25 seconds) from a movie recorded with an acquisition time of 500 ms with continuous 405 nm and 488 nm illumination are shown. At first, fluorescence is concentrated in bright spots representing endosomes. After 25 seconds, the cytosol shows a faint fluorescence indicating the cell boundary as well as the nucleus. At this time only few single fluorescent structures are visible. This indicates that the fluorescent endosomal contents have been released into the cytosol.

A detailed analysis of the increase in cytosolic fluorescence is presented in figure 5.6. In this figure the mean fluorescence intensity of a region in the cytosol of the cell periphery without fluorescent structures (marked by a circle in figure 5.5) is plotted versus the 405 nm illumination time. The fluorescence intensity was corrected for bleaching of the dye due to 488 nm laser illumination. The fluorescence intensity of a small spot was determined over time until the start of 405 nm illumination. Thus, bleaching of this spot was only due to 488 nm illumination. These values formed the so-called baseline. Division of the fluorescence intensity of the original spot by this baseline resulted in the presented values. These are therefore relative values and the fluorescence intensity at the start of the measurement was set to zero. The cytosolic fluorescence shows a steep increase between 6 and 15 seconds after start of the 405 nm illumination. This increase correlates with the disappearance of several bright spots.

The fluorescence increase of the cytosol was strongly dependent on the amount of AFD internalized by the cell. In cells heavily loaded with AFD, the cell boundaries became visible after excitation of TPPS$_{2a}$ as a result of the increase in cytoplasmic fluorescence. Charac-

(a) Before endosomal release   **(b)** After endosomal release
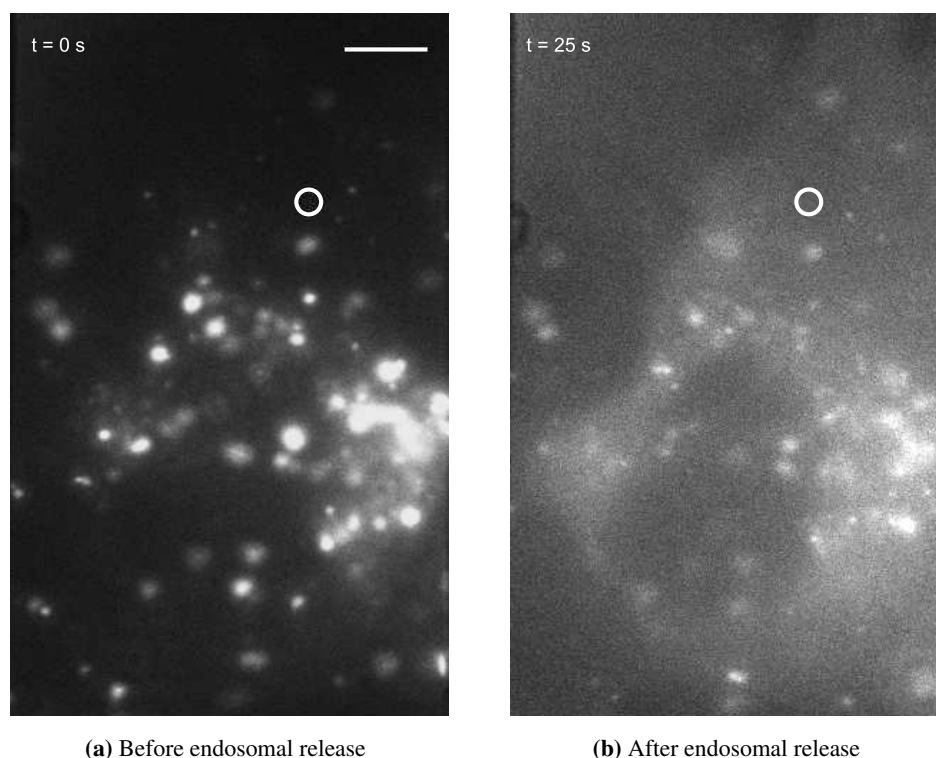
Figure 5.5: Two frames of a video stream recorded with an acquisition time of 500 ms. (a) Cell with beginning of 405 nm illumination. The AFD fluorescence is concentrated in bright spots representing endosomes. (b) After 25 s of 405 nm illumination the endosomal content has been released resulting in a faint fluorescence of the cytosol. Thereby, the boundary of the cell is visible. Scale bar: 5 μm. The circle indicates the region of interest analyzed in figure 5.6.

teristically, the nucleus did not show any increase in fluorescence intensity. For cells with small amounts of internalized dye, an increase in fluorescence intensity of the cytosol was not detected.

In order to obtain a detailed view of the endosomal release of AFD, the release process was imaged at a higher temporal resolution. Analysis of movies recorded with 20 ms acquisition time showed that the fluorescence of AFD did not disappear at once but dispersed around the endosome (see figure 5.7a). Often, the dye release occurred asymmetrically. This suggests rupture on one side of the endosome.

In figure 5.7b the fluorescence intensity of the endosome presented in figure 5.7a and its surroundings is plotted versus 405 nm illumination time. The fluorescence intensity was corrected for bleaching of the dye due to laser illumination as described before. A sharp decrease in fluorescence intensity of the endosome after 12.9 seconds of illumination with
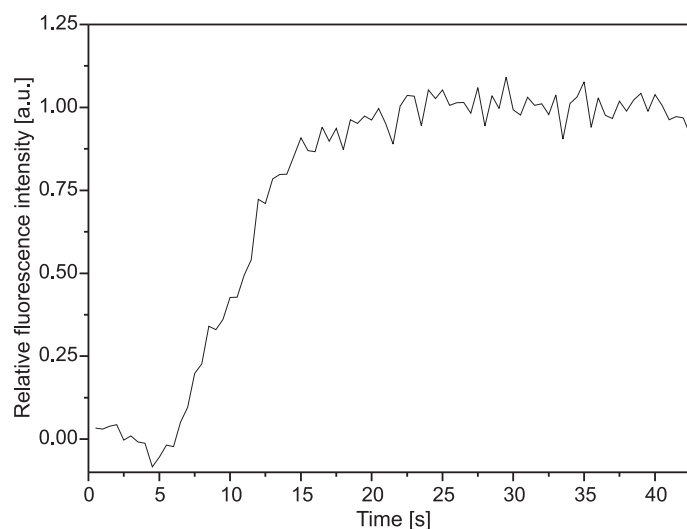
Figure 5.6: The mean fluorescence intensity of a cytosolic region without fluorescent structures (marked with a white circle in figure 5.5) was plotted against illumination time. A steep increase in intensity between 6 and 15 s represents the increase in cytosolic fluorescence and corresponds to the release of AFD from endosomes.

405 nm light indicates the release of the cargo and correlates with a fluorescence increase of the surrounding cytoplasm. Within 100 ms the fluorescence intensity of the endosome decreases to 50% of the original value. In the same time span the surrounding cytoplasm reaches maximum fluorescence intensity followed by a slower decrease to background level within the next 500 ms in which the dye spreads out further into the cytosol. After the respective maximum and drop in fluorescence, the fluorescence of the surroundings and the former endosome remains constant.

In summary, these results show that endosomal release can successfully be visualized by microscopic methods in real time. The photosensitizer was loaded into endosomes together with the fluorescent dextran. Upon photosensitizer activation, the endosomal membrane was damaged and the endosomal content was set free into the cytosol within 100 ms.

The rapid diffusion through the cytosol is in good agreement with studies on the diffusion characteristics of FITC-dextran as performed by Arrio-Dupont et al. [170]. For dextrans with a molecular weight of 95–150 kDa free diffusion in the cytosol was observed. In addition dextrans smaller than 40 kDa were seen to enter the nucleus [170, 192]. In our case, the nucleus was not stained by the Alexa dye, which may be due to the time point of observation. In the aforementioned studies, dextrans were microinjected into the cytoplasm and the cells were studied several hours afterwards to allow the cells to recover. In our case, the observation time was only 25 seconds. Nuclear entry of AFD may be observed when cells are imaged some hours after inducing endosomal release.
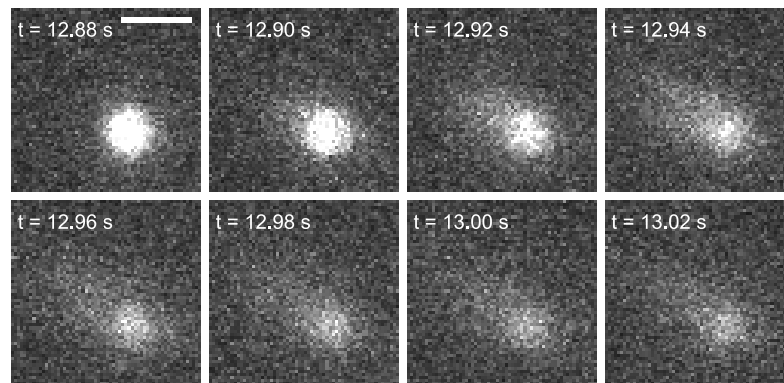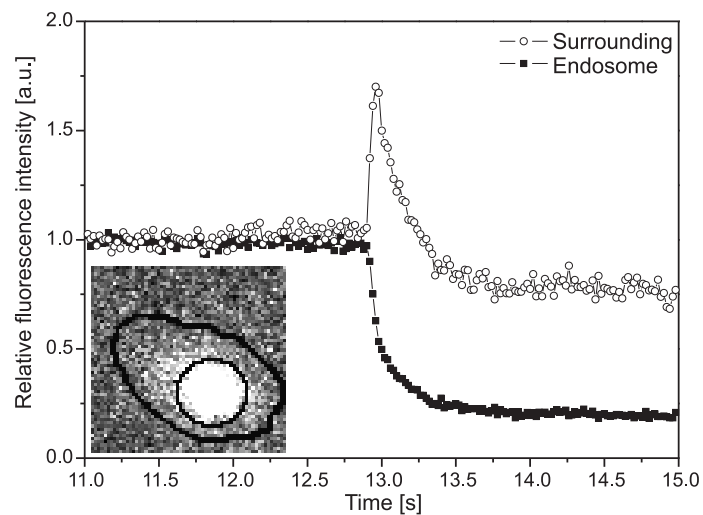
(a) AFD release

(b) Analysis of AFD release

Figure 5.7: (a) Endosomal release of AFD at a higher temporal resolution. The images show one single endosome filled with AFD and correspond to eight frames of a movie recorded with an acquisition time of 20 ms. The time stamp indicates the time after onset of 405 nm illumination. The release of AFD occurs asymmetrically around the endosome. Scale bar: 2 μm. (b) The mean intensity of the endosome shown in (a) and its surroundings was plotted versus 405 nm illumination time. The regions of interest are shown in the inset. Corresponding to the release demonstrated in (a), the fluorescence intensity of the endosome shows a sharp decrease at 12.9 s. Simultaneously, the intensity of the immediate surroundings of the endosome shows a sharp increase with a maximum after 80 ms, followed by a decrease due to diffusion of the dye in the cytoplasm. After 13.46 s the intensity remains constant for both endosome and surrounding.

5.3 Endosomal release of polyplexes

After ensuring visualization of photoinduced endosomal release of AFD, the release dynamics of polyplexes was investigated. Since LPEI, PLL and PDL polyplexes differ in their endosomal buffering capacity, biodegradability and their binding strength to DNA, they are expected to show distinct release dynamics.

LPEI is a nonbiodegradable polymer with protonatable amino groups with a pKa in the range of 4 to 7. As we have seen in section 2.5.1 this characteristic leads to buffering of endosomes such that lysosomal enzymes remain inactive and degradation of the gene vector is impeded.

The cationic polymer PLL does not show the buffering ability as seen for LPEI [45, 193]. After endocytosis, endosomes containing PLL particles show a decrease in pH and maturation to lysosomes takes place [193]. PLL is biodegradable because of its L-amino acid lysine. Therefore, in principle peptidases and proteases in the lysosomes are able to degrade PLL and consequently DNases are able to degrade DNA. However, studies with DNase I have shown that the strong condensation of DNA by PLL protects polyplexes against degradation [194].

Like PLL, the D-amino acid stereoisomer PDL does not possess buffering abilities. The intracellular pathway of PDL particles is therefore similar to that of PLL particles. In contrast to PLL, PDL is nonbiodegradable, because of the D-amino acid residues. Nevertheless, this characteristic does not influence the capability to protect DNA from enzymatic degradation [195].

In order to image both components of the polymer/DNA particles simultaneously, the cationic polymer was covalently labeled with Alexa Fluor 488 succinimidyl ester (A488) and DNA with cy5. The labeled particles were purified to exclude free dye and polymer (see section 3.1.7). HUH7 WT cells were seeded 48 hours before measurement in a density of $1.0 \cdot 10^4$ cells per well, on a collagen A-coated LabTek chambered cover glass. After 24 hours, the medium was changed in the dark to medium containing 0.025 µg/ml TPPS$_{2a}$ and 0.1–1.0 µg/ml DNA depending on the polymer. Control cells were incubated with medium containing only DNA. 12–16 hours later the cells were washed in the dark three times with CO_2-independent medium to remove residual TPPS$_{2a}$ and subsequently placed on a heated microstage (37°C) and imaged. Since illumination of the cells should be avoided, the samples were handled in aluminium foil before measurement. The focal plane of the microscope was found by weak excitation of the cy5-labeled DNA at 647 nm, since the photosensitizer was least activated at this wavelength.

The 12–16 hours incubation of polyplexes and photosensitizer differs from earlier published procedures [19]. In earlier publications cells were incubated overnight with photosensitizer only prior to incubation with polyplexes for 4 hours in photosensitizer free medium. The simultaneous, long incubation of polyplexes and photosensitizer as described above was chosen to ensure that particles and photosensitizer were in the same cellular compartment when observed under the microscope. To exclude adverse effects of this long incubation in photosensitizer-containing medium on the transfection ability of polyplexes, transfection experiments were carried out by Carolin Fella (Prof. E. Wagner, LMU, Munich) using both procedures. Comparing the long overnight incubation of particles with the 4-hour incubation on the following day, a higher transfection efficiency was observed for particles incubated overnight. This indicates that the transfection ability of polyplexes is not impaired by longer incubation times used for the microscopical observations.

A direct influence of TPPS$_{2a}$ on A488 fluorescence as well as on particle integrity was excluded for all used polymers by addition of TPPS$_{2a}$ to A488-labeled LPEI, PLL and PDL particles on a cover slip. No quenching effect or inactivation of the fluorescence of the polymer was observed.

In the following experiments the 405 nm laser line was used to induce photosensitizer activation, the 488 nm laser line to excite the A488-labeled polymer and the 647 nm line to excite the cy5-labeled DNA. The time printed on the images always represents the time elapsed since the start of the 405 nm illumination. The duration of the 405 nm illumination time is mentioned separately for each experiment.

5.3.1 LPEI

The first polyplexes to be characterized were LPEI/DNA particles. For these polyplexes, a difference in fluorescence distribution within the endosomes between polymer and DNA component was observed already before photosensitizer activation. Moreover, a different release pattern was detected as demonstrated in figure 5.8a. The images represent four consecutive frames of a movie recorded with an acquisition time of 500 ms and show a representative endosome filled with LPEI/DNA particles. The fluorescence signal of both particle components, LPEI and DNA, is presented in separate panels.

Before release, LPEI showed a homogeneous fluorescence distribution within the endosome. After activation of the photosensitizer, the release of LPEI was similar to AFD: the fluorescence disappeared in one sudden step without persisting fluorescence above the background level in the endosomal region (figure 5.8a, lower panel). Furthermore, sometimes an increase in cytosolic fluorescence throughout the whole cell was observed, depending on the particle load of the cell. The fluorescence signal in the lower panel exclusively represents the LPEI distribution, since free dye molecules were removed during the purification steps before and during particle generation (described in section 3.1.7).

DNA in contrast showed an inhomogeneous fluorescence distribution within the endosomes (figure 5.8a upper panel). In large endosomes, several bright spots could be distinguished. Upon photosensitizer activation, the bright spots were released in a sudden "blow-up"-like broadening of the DNA in different directions. This "blow-up" pattern reminded of endosomes that burst under pressure. Afterwards, significant amounts of DNA remained visible in a confined area of a few micrometers in diameter around the damaged endosome. Observations for two hours following release did not show any further movement of the remaining structures.

Analogously to AFD release, the release of DNA is analyzed in figure 5.8b. The fluorescence intensity of the endosome and its surroundings was determined and plotted versus time. Correction for bleaching of the dye due to laser illumination was done by dividing the fluorescence intensities of endosome and surroundings by the fluorescence intensity of a background region for each video frame. The values are therefore relative values and the fluorescence intensity at the start of the measurement was set to one.

As observed for AFD, a drop in fluorescence intensity of the endosome was detected after 28 seconds of 405 nm light illumination. The intensity of the endosome decreased to 50% within 4 seconds. Simultaneous with the decrease of the endosomal fluorescence intensity, an increase in surrounding fluorescence was observed. In sharp contrast to the observations for

(a) LPEI particle release

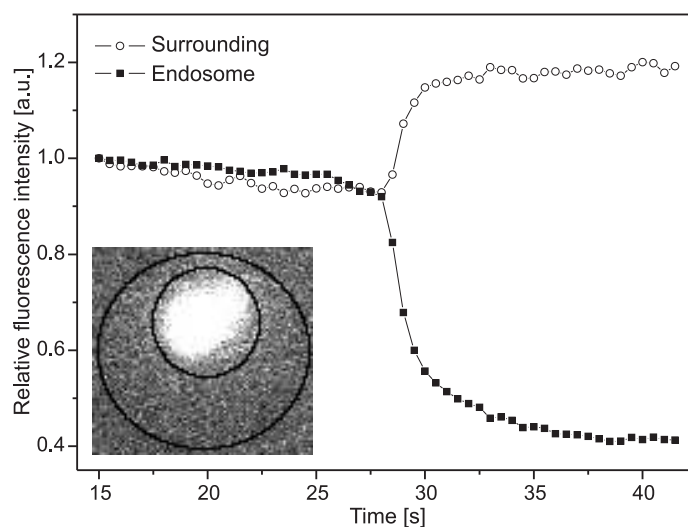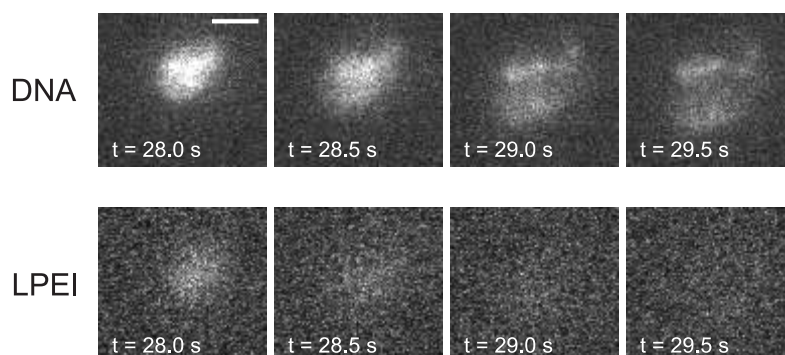**(b)** Analysis of DNA release

Figure 5.8: (a) The images present four frames of a movie recorded with an acquisition time of 500 ms and show one endosome filled with LPEI/DNA particles. The upper panel shows the fluorescence intensity of DNA, the lower panel LPEI. After 28 s of 405 nm illumination, the LPEI fluorescence disappears in one sudden step, whereas DNA fluorescence remains visible in a confined area. Scale bar: 2 µm. (b) The mean DNA-cy5 fluorescence intensity of the endosome shown in (a) and its surroundings (see inset) was plotted versus 405 nm illumination time. After 28 s, a decrease in endosome intensity and an increase in surrounding intensity was observed. Both intensities reach a constant level after 33 s.

AFD, the fluorescence intensity of the surroundings remained at a constant level and did not decrease to the background value. This shows that after membrane rupture, the DNA disperses in a sudden burst around the endosomal region but remains immobile afterwards. Therefore the intensity of the surroundings does not drop back to background level as observed for AFD, which diffused into the cytoplasm.

In short, we observed the following differences between the release patterns of DNA and LPEI: first, the heterogeneity (DNA) versus the homogeneity (LPEI) of the fluorescence within the endosome; second, the particulate versus homogeneous spread into the cytosol after release; third, the confined reminiscence of the DNA fluorescence versus spread of LPEI fluorescence throughout the whole cell; and fourth, the different time scales of endosomal fluorescence decrease.

From these differences, the release of LPEI/DNA particles can be interpreted as follows. After endosomal rupture, diffusion of LPEI through the cytosol is observed resulting in decreasing fluorescence intensity of the former endosome and an increase in cytosolic fluorescence. LPEI has a molecular weight of 22 kDa allowing diffusion in the cytoplasm [171, 192]. Plasmid DNA in contrast cannot diffuse in the cytosol due to its large size [107, 108]. Its diffusion in the cytoplasm is hindered by various cellular structures and DNA is therefore largely immobile. This explains the observed differences in the diffusion behavior between LPEI and DNA.

The fact that this difference was observed implies that LPEI and DNA are dissociated to a large extent during endosomal release. Decondensation of LPEI and DNA in the cytoplasm was shown by Itaka et al. [196]. Dissociation in the cytoplasm may be induced by RNA [197]. However, this process takes place on a larger time scale than the rapid release of LPEI observed here. This suggests that the particles in the endosome have to be in a decondensed state already before rupture of the endosomal membrane. The inhomogeneous pattern of the DNA versus the homogeneous distribution of LPEI in the intact endosomes supports (partial) decondensation of the polyplexes in the endosome.

The release of DNA was observed as a fast broadening of fluorescent structures that were immobile afterwards. The fast movement of the nondiffusible DNA for a very short moment may be induced by pressure. An eventual pressure in the endosomes may be explained by the "proton sponge" effect of LPEI (section 2.5.1). The buffering capacity and reduced acidification is accompanied by an increased chloride accumulation resulting in osmotic swelling of the endosomes [45]. Damaging the membrane of an endosome under pressure would therefore lead to a burst that is observed as a fast broadening of the nondiffusible DNA. The "proton sponge" effect also inhibits progression to lysosomes by buffering the pH of endosomes [198]. Therefore the DNA is protected against degradation even in case LPEI and DNA decondensate in the endosome before release. This is in agreement with the observation of nondiffusible and therefore intact plasmid DNA after endosomal release.

To summarize, LPEI/DNA particles seem to be dissociated already before endosomal release. They are present in endosomes, since no lysosomal degradation of the DNA is observed. Upon release, LPEI diffuses freely through the cytoplasm due to its small size. DNA is released out of the endosome under pressure and is afterwards immobile in the cytoplasm.

5.3.2 PLL

For LPEI and DNA no colocalization was found after endosomal release which implies that LPEI particles are dissociated during endosomal release. To determine whether the release behavior of DNA and polymer was dependent on binding affinity to and the characteristics of the cationic polymer, a polymer with stronger DNA binding properties was used. In previous studies it was shown that the polymer poly-L-lysine (PLL) has a much higher affinity for DNA than LPEI resulting in stronger particle condensation [196]. It was shown that the condensed state of the PLL particles was maintained in the cytoplasm and thus no dissociation took place. Therefore, colocalization of PLL and DNA after endosomal release is expected.

For PLL/DNA particles, polymer and DNA showed comparable release patterns. According to the release dynamics, two endosomal populations were classified. These two populations are depicted in figure 5.9. Two images from a video sequence are presented directly after the start of the 405 nm illumination and at $t = 110.5$ s. The fluorescence signal of DNA and PLL is presented in different channels.

A homogeneous fluorescence distribution within the endosome was characteristic for PLL as well as for DNA before photosensitizer activation. In sharp contrast to the release of LPEI/DNA particles, all endosomes showed simultaneous and similar endosomal release of both PLL and DNA. The majority of endosomes released their contents completely in one sudden step without visible remaining fluorescence. For a small fraction of endosomes, illumination with 405 nm only led to a small decrease in fluorescence intensity for PLL as well as DNA. In figure 5.9 three endosomes are visible showing this behavior (arrowheads).

In figure 5.10 and figure 5.11 an example of these differing populations of endosomes is presented. Figure 5.10 shows three consecutive frames from a movie recorded with 500 ms acquisition time. The fluorescence intensity of both particle components of the endosome marked with an arrow simultaneously decreased in a sudden step after illumination with 405 nm laser light. Only slight fluorescence remained in the endosomal region for both components (figure 5.10, arrow). The second endosome, marked with an arrowhead, shows endosomal release at a later time point. The decrease in endosomal fluorescence was accompanied by a slight increase in cytosolic fluorescence intensity of PLL.

In figure 5.11 one endosome is presented which shows only a small decrease in fluorescence intensity for PLL as well as DNA after illumination with 405 nm light. The release is indicated by the change in diameter of the fluorescence signal between frame two and three. Particles with only a small decrease in intensity after release were comparably bright even after prolonged illumination. The spots persisted at the location of the original endosome without any movement.

As mentioned at the beginning of this section, PLL/DNA particles were expected to show colocalized endosomal release, because of the higher DNA binding affinity. This was indeed observed. For the majority of endosomes, a rapid diffusion of PLL as well as DNA was noticed
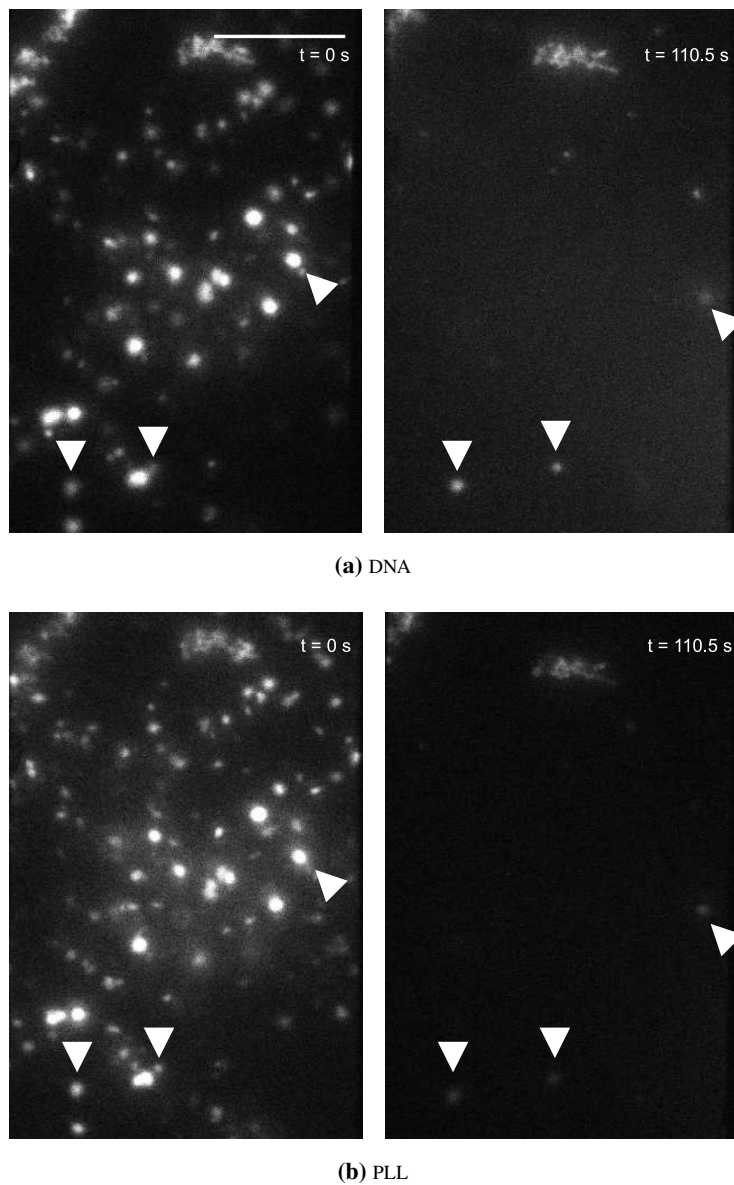
(a) DNA

(b) PLL

Figure 5.9: Image at the start of 405 nm illumination (left) and after 110.5 s (right) with an acquisition time of 500 ms. The 405 nm illumination period lasted 10 s. In (a) the distribution of DNA-related fluorescence in a cell is shown. In (b) the fluorescence of PLL is presented. The overwhelming majority of endosomes disappears completely after photosensitizer activation. Three endosomes show only a small decrease in fluorescence intensity (arrowheads). Scale bar: 10 μm.
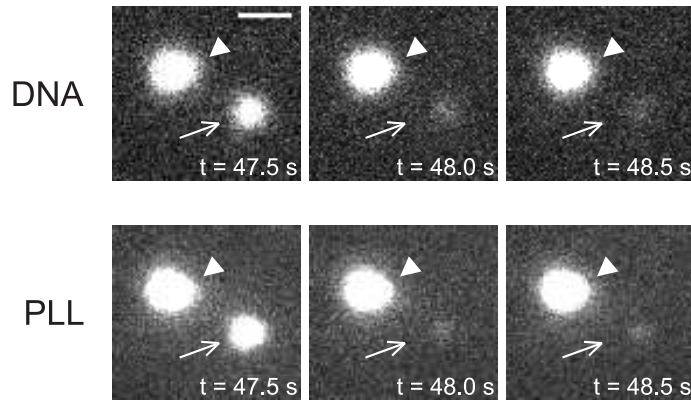
Figure 5.10: The images show frames from a movie recorded with an acquisition time of 500 ms. The cells were illuminated with 405 nm laser light for 5.5 s. The images show two endosomes in three subsequent frames 47.5 s after start of 405 nm illumination. The upper panel represents DNA fluorescence, the lower panel PLL fluorescence. In one endosome, the fluorescence intensity of both DNA and PLL decreased in one sudden step (arrow) and little fluorescence remained in the endosomal region whereas the second endosome (arrowhead) did not release its content in the presented time interval. Scale bar: 2 μm.
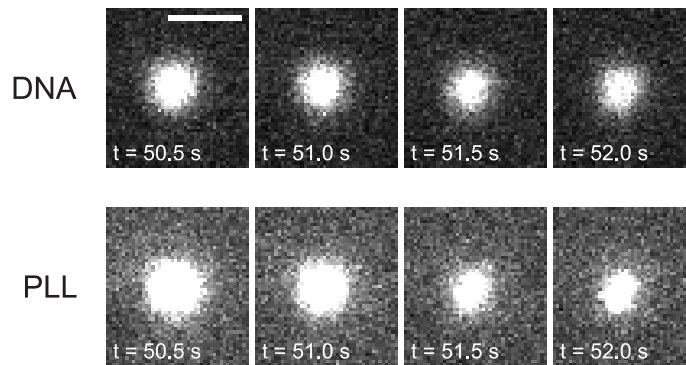

Figure 5.11: The images show frames from a movie recorded with an acquisition time of 500 ms. The cells were illuminated with 405 nm laser light for 5.5 s. The images present four subsequent frames of a movie showing one endosome filled with PLL/DNA particles. The upper panel represents DNA fluorescence, the lower panel PLL fluorescence. The first frame shows the endosome 50.5 s after the start of 405 nm illumination. The fluorescence intensity of both DNA and PLL decreased only slightly and a bright spot remained visible even after prolonged illumination with 405 nm laser light. Scale bar: 2 μm.

upon photosensitizer activation. Simultaneous and similar release behavior was seen as well for the small fraction of endosomes that showed only a small decrease in intensity. The fact that a cytosolic increase in fluorescence was observed for PLL but not for DNA may be explained by the different labeling ratios of both components. Since the molar ratio of Alexa dye:cy5 dye was 5.5:1, PLL may have remained visible after endosomal release, whereas DNA could not be detected further.

The observation that DNA diffuses rapidly away from the endosome implies that it is degraded into smaller fragments before endosomal release is induced. The cellular compartment for degradation in the endocytic pathway is the lysosome, therefore PLL/DNA particles are most probably transported to lysosomes. This is confirmed by Akinc et al. [193] demonstrating that the PLL/DNA particles are present in compartments with low pH and thus no "proton sponge" effect was observed [45].

Now the question arises whether the colocalized endosomal release of DNA and PLL proves that the particles are still condensed in the cytoplasm. When in condensed form, PLL protects DNA from degradation by DNAse I, a DNA digesting enzyme [194]. However, DNA showed rapid diffusion upon endosomal release implying degradation of DNA. Therefore, particles may be dissociated before endosomal release takes place. The protection of DNA by PLL may have been lost during the 12 hours incubation period and degradation of PLL and DNA may induce dissociation of the complexes.

A small population of endosomes filled with PLL/DNA particles showed only a modest decrease in fluorescence intensity after activation of the photosensitizer. This suggests that the polyplexes are still partly intact, probably due to the strong condensation of DNA by PLL. Upon endosomal disruption the condensed particles are too large to diffuse through the cytoplasm. These particles may still be in late endosomes where little degradation occurs.

In short, two populations of PLL/DNA particles can be distinguished. The largest population is transported to lysosomes where degradation of PLL and DNA takes place. Upon photosensitizer activation, both components diffuse freely through the cytosol. A small population of particles may still be in late endosomes where little degradation occurs. It consists partly of intact particles that are too large to diffuse through the cytoplasm.

5.3.3 PDL

Up to this point, release of *intact* DNA was observed when DNA was condensed with a *non-biodegradable* polymer *with buffering ability*. DNA *degradation* occurred for *biodegradable* particles *without buffering capacity*. To relate the degradation of DNA to biodegradability, poly-D-lysine (PDL) was used as a condensing polymer. PDL is the D-amino acid isomer of PLL and is also able to condensate DNA [51]. Just as PLL it is not able to buffer the pH of endosomes. Due to its D-amino acid residues it is not accessible to enzymatic digestion in the lysosome.

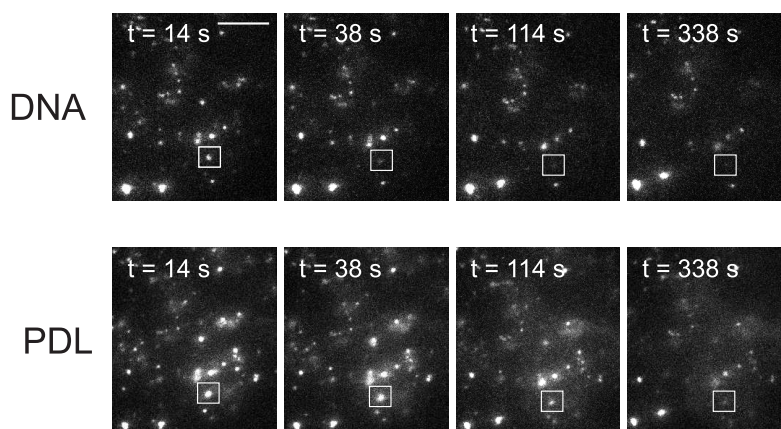The release of PDL/DNA particles is presented in figure 5.12. Four frames from a video sequence recorded with an acquisition time of 500 ms are shown. The first frame shows the cell immediately after the end of the 405 nm illumination period (13.5 s). The fluorescence signal of DNA and PDL is separated in different panels. Upon activation of the photosensitizer, most endosomes containing PDL/DNA particles did not show a clear and sudden decrease in

Figure 5.12: Four images from a video sequence recorded with an acquisition time of 500 ms are shown. The first frame shows the cell immediately after the 405 nm illumination time (13.5 s). Following frames are taken 38 s, 114 s and 338 s after the start of 405 nm illumination. The upper panel represents DNA fluorescence, the lower panel PDL fluorescence. Most particles do not show a clear decrease in intensity. Some particles show a decrease in intensity in the DNA fluorescence signal but no decrease in PDL fluorescence (boxed particle). Scale bar: 10 μm.

intensity. As this could also be caused by a lack of photosensitizer in the endosomes, the efficacy of endosomal release was verified in control samples with the same amount of TPPS$_{2a}$ and LPEI/DNA particles under the same imaging conditions.

A second, small fraction of PDL/DNA particle-loaded endosomes was observed that showed a slight decrease in intensity of the PDL signal and a stronger decrease in intensity of the DNA signal. In figure 5.12 these are marked by boxes.

Since PDL particles do not show buffering ability, the two observed populations of PDL particles are expected to be in lysosomes. The largest population of lysosomes did not show a clear decrease in intensity. For these particles, PDL has successfully protected the DNA from degradation. Particles remain intact and therefore immobile in the cytoplasm upon photosensitizer activation.

For a small population of lysosomes, a modest decrease in the intensity of the DNA signal was observed. In these lysosomes, nucleases may have been able to cleave a certain amount of DNA during the long incubation period. Although it was shown that PLL and PDL can protect DNA from degradation in experiments with 30 minutes incubation in crude cell lysates [195], our results with 12 hours incubation suggest that DNA is not fully protected against lysosomal degradation on longer time scales. Overall, the nonbiodegradable PDL protects the DNA from degradation, although not as efficiently as observed for LPEI.

Taken together, two populations of PDL/DNA particles can be distinguished. The largest population is presumably transported to lysosomes but degradation of DNA is hindered by PDL. Upon photosensitizer activation, intact particles remain immobile in the cytosol. A small population of particles may be partly degraded and release of DNA into the cytosol is observed.

5.4 Summary

In this study we visualized endosomal release of polyplexes induced by photosensitizer activation. The release of a fluid phase marker provided information on the efficacy of photoinduced endosomal release and on the time scale of release. By comparing the endosomal release of three different classes of polyplexes, release characteristics like mobility in the cytoplasm, degradation of the particles and dissociation of polymer and DNA were investigated. The results demonstrate that the characteristics of the cationic polymer used to condensate DNA significantly influence the release behavior of the polyplexes.

Experiments with a fluorescently labeled dextran showed successful loading of endosomes with photosensitizer and AFD. Upon photosensitizer activation, the endosomal membrane was damaged and the endosomal content was set free into the cytosol within 100 ms. AFD rapidly diffused through the cytosol without staining the nucleus within the observation period.

For the release of the cationic polymers, the following behavior was observed. Upon release, the intact (since nonbiodegradable) LPEI diffused quickly away from the original endosome and was spread throughout the cytosol, which can be explained by the small size of the polymer. On the time scales of observation, no diffusion of LPEI into the nucleus was observed.

PLL has a higher binding affinity to DNA than LPEI. Therefore, PLL was expected to protect the DNA more efficiently than LPEI and thus to prevent dissociation of the polyplex. In this case, the intact particles would remain immobile in the cytoplasm. Nonetheless the release behavior of PLL was similar to LPEI. PLL diffused from the endosome without any remaining structures on the site of the endosome and in rare cases an increase in cytosolic background indicated diffusion throughout the cytosol. PLL is biodegradable and may therefore be degraded in the lysosome. Then, PLL is able to freely diffuse from the endosome throughout the cytosol upon photosensitizer activation.

For PDL, almost no release was observed upon photosensitizer activation. PDL condenses DNA in the same way as PLL. In contrast to the condensation of LPEI, the strong condensation of PDL protects DNA against degradation. PDL itself is not biodegradable and therefore PDL/DNA particles remain intact. Thus, after photosensitizer activation particles remain immobile in the cytoplasm.

The release of DNA showed more distinguishable patterns. For LPEI/DNA particles, release of intact DNA was detected. The fact that LPEI/DNA particles remain in endosomes instead of lysosomes may play a major role in the conservation of DNA. Since LPEI/DNA particles have buffering ability which leads to reduced acidification DNA is prevented from degradation by lysosomal enzymes. The relatively weak binding affinity of LPEI to DNA, compared to PLL and PDL, may be lost within the endosomes already.

For PLL/DNA particles, fast release of both polymer and DNA was observed. Since PLL is

biodegradable and does not show a proton sponge effect, it may be degraded in the lysosome. This induces degradation of DNA and probably dissociation of the polyplex.

PDL/DNA particles remain largely intact in lysosomes due to the nonbiodegradability of PDL. Therefore, DNA remains largely within the endosome upon photosensitizer activation. Some DNA was released, possibly due to some lysosomal activity as a consequence of the long incubation time of 12 hours.

6. Cellular effects of photoinduced endosomal release

In the last chapter we saw that activation of TPPS$_{2a}$ results in cargo release from endosomes. TPPS$_{2a}$ is excited into a singlet state and subsequently falls back into a triplet state. This triplet state is quenched by molecular oxygen whereupon singlet oxygen is generated. Damage of macromolecules in the endosomal membrane by singlet oxygen then leads to endosomal escape.

Apart from increasing endosomal release of gene vectors, the generation of singlet oxygen by photoactivation of porphyrins is known to have side effects. Singlet oxygen is a highly reactive species with a lifetime of maximal 4 μs in H$_2$O [105] and a diffusion radius of 50 nm [106]. It easily oxidizes organic macromolecules like membrane lipids, proteins, amino acids, DNA and RNA [20, 199] that are in close proximity. Generation of large amounts of singlet oxygen in the cell leads to damage of cell membranes, mitochondria, lysosomes and nuclei and eventually to apoptosis of cells [200]. These harmful side effects are exploited by photodynamic therapy, a method to reduce cancer growth. In this method, photosensitive compounds (often porphyrins) are intravenously administered to the body and accumulate in tumor tissue. Upon photosensitizer activation, singlet oxygen is produced and reacts with intracellular targets which eventually leads to tumor necrosis [200].

In addition to singlet oxygen-related side effects, a direct influence of porphyrins on cellular compartments was observed. Porphyrins interact with the microtubule cytoskeleton by inhibition of microtubule assembly [201], most probably by binding to tubulin [202].

In this chapter the influence of TPPS$_{2a}$ on different compartments of the cell is examined. First, the interaction of TPPS$_{2a}$ with microtubules and actin cytoskeleton is studied. Second, the effect of photoactivation on early and late endosomes is demonstrated. Finally, an influence on endosomal motion is observed immediately after start of photosensitizer activation.

6.1 Microtubules and actin

It has been demonstrated earlier that porphyrins have a toxic effect on the cytoskeleton by inhibition of microtubule assembly [201]. Porphyrins bind to tubulin heterodimers [202] and a decrease in the amount of microtubules was found upon incubation of cells with tetra(4-sulfonatophenyl)porphine (TPPS$_4$) [203]. Nevertheless, visualization of microtubule damage by means of high resolution microscopy has not yet been performed. This motivated us to perform highly sensitive microscopic experiments with tubulin-GFP (green fluorescent protein) and actin-GFP expressing HUH7 cells. This enabled the visualization of microtubule
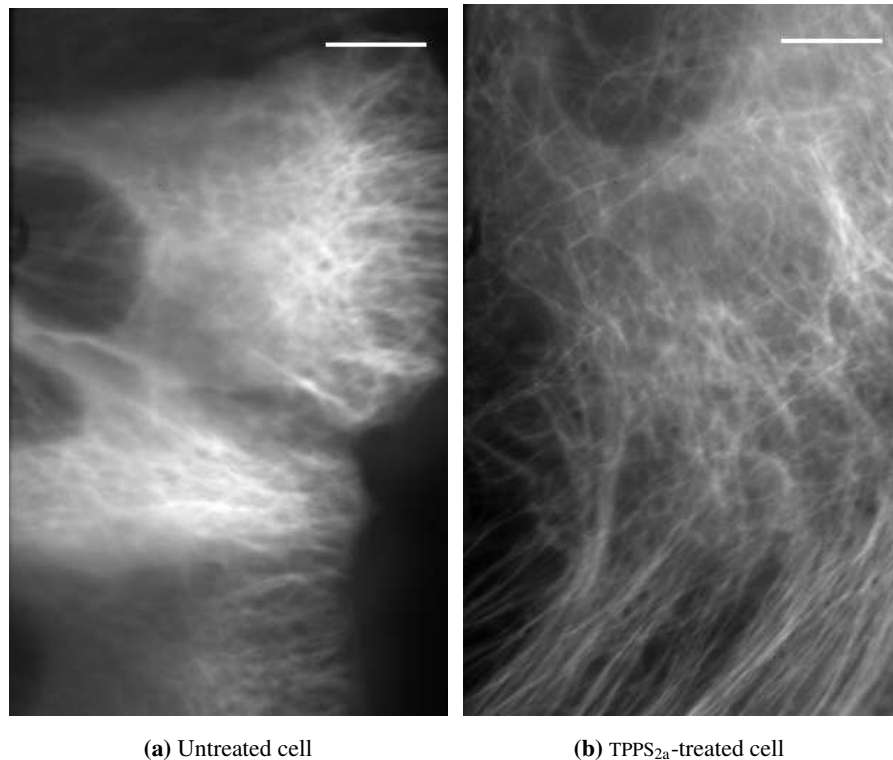
(a) Untreated cell   **(b)** TPPS$_{2a}$-treated cell

Figure 6.1: The influence of TPPS$_{2a}$ on tubulin-GFP expressing cells. For both a control (a) and a TPPS$_{2a}$-treated (b) cell the first 175 frames from a video sequence (acquisition time: 500 ms) were averaged. For the control cell the obtained image is blurred, for the TPPS$_{2a}$-treated cell single microtubule strands can be distinguished. Scale bar: 10 μm.

movement and loss of movement in untreated and photosensitizer-treated cells, respectively.

Tubulin-GFP and actin-GFP expressing HUH7 cells were seeded 48 hours before measurement in a density of $1.0 \cdot 10^4$ cells per well, on a collagen A-coated LabTek chambered cover glass. After 24 hours, the medium was changed in the dark to medium containing 0.025 μg/ml TPPS$_{2a}$ and in some cases 62.5 μg/ml Alexa Fluor Dextran (AFD), labeled with the Alexa Fluor 647 dye. The medium of control cells was changed to medium without photosensitizer. 12–16 hours later the cells were washed three times in the dark with CO_2-independent medium to remove residual TPPS$_{2a}$. Since illumination of the cells should be avoided, the samples were handled in aluminium foil before measurement and subsequently placed on a heated microstage (37°C) and imaged.

In the following experiments, the photosensitizer was not activated by the 405 nm laser, but by 488 nm laser light for the following reason. GFP is excited at 488 nm and its emission lies in the range of 500–550 nm (see section 3.3.2). The intensity of the GFP fluorescence

strongly depends on the amount of GFP expressed in the cells. To visualize microtubules and actin filaments, the intensity of the 488 nm laser light was increased by a factor of 10–100 compared to the endosomal release experiments described in the last chapter. As a consequence of this, the photosensitizer was activated with the 488 nm laser, since at this wavelength TPPS$_{2a}$ shows weak absorption (figure 5.2a). This implies that differentiation between visualization of the microtubules and activation of the photosensitizer was impossible.

The effect of TPPS$_{2a}$ incubation and activation on microtubules is presented in figure 6.1. For both a control and a TPPS$_{2a}$-treated cell, the first 175 frames from a video sequence, recorded with an acquisition time of 500 ms, were averaged and the resulting image is presented. For the untreated cell the obtained image is blurred (figure 6.1a). Individual strands cannot be distinguished. In untreated cells microtubules show the typical bending and buckling caused by polymerization and depolymerization. This movement results in a blur when the fluorescence intensity of several frames from a video sequence is averaged. In contrast, in the averaged image of the photosensitizer-treated cell, single microtubules can be identified (figure 6.1b). Microtubule motion was largely absent in this case and thus averaging of images does not result in blur. This suggests that microtubule motion is inhibited by TPPS$_{2a}$. Remarkably, in both the untreated and TPPS$_{2a}$-treated cell an intact microtubule network was observed, which remained intact during observation.

In cases where cells were incubated with TPPS$_{2a}$ and Alexa Fluor Dextran (AFD) inhibition of microtubule movement was observed before endosomal release of AFD took place. This suggests that inhibition of microtubule dynamics was not induced by the endosomal release process itself nor by free TPPS$_{2a}$ released upon endosomal release, but resulted from direct interaction of the photosensitizer with microtubules before cargo release.

Inhibition of microtubule dynamics was also observed after 2 hours of photosensitizer incubation in the dark. After 6 hours of re-incubation in photosensitizer-free medium no renewed movement was detected.

Whether the microtubule movement was inhibited already before photosensitizer activation could not be distinguished. First, due to the high intensity of the 488 nm laser, imaging of the microtubules implied photosensitizer activation. Therefore, imaging and activation of the photosensitizer could not be separated. Second, to determine motion during a movie, several consecutive frames are necessary: one single frame does not show movement. During imaging of these frames, the photosensitizer was activated because of the aforementioned reason and thus inhibition of microtubule motion before photosensitizer activation could not be distinguished.

These observations suggest a direct contact between photosensitizer and microtubules. Obviously, for this to happen the photosensitizer has to be present in the cytosol. Two possible mechanisms exist for TPPS$_{2a}$ to get into the cytosol and intervene with the microtubule dynamics. The first possibility is that TPPS$_{2a}$ is released from the endosome upon photosensitizer activation and rapidly spreads out throughout the cytosol. Since we have seen that microtubule dynamics were absent *before* endosomal release of dextran, this does not seem a probable mechanism.

The second possibility is that during the long incubation time TPPS$_{2a}$ penetrates directly through either the cell membrane or the endosomal membrane to get into the cytosol. Although little photosensitizer is expected in the cytosol due to the preferential incorporation
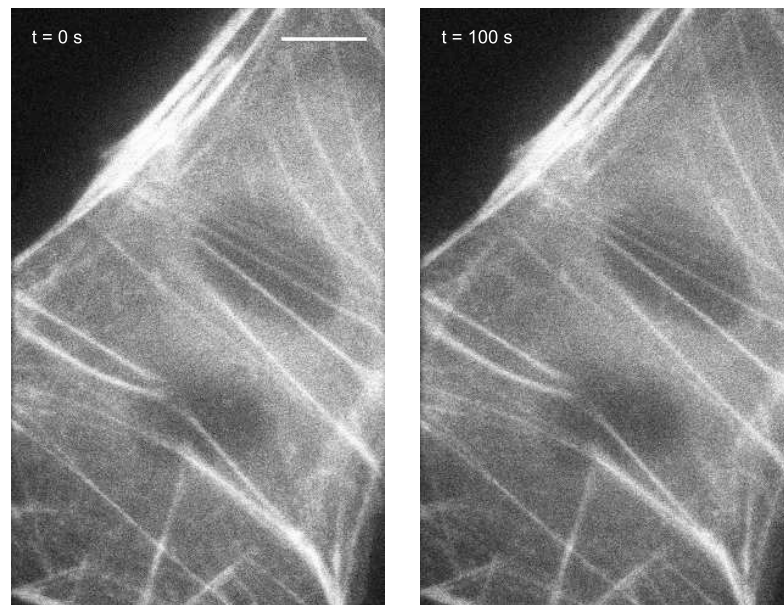
(a) Untreated actin-GFP expressing cell
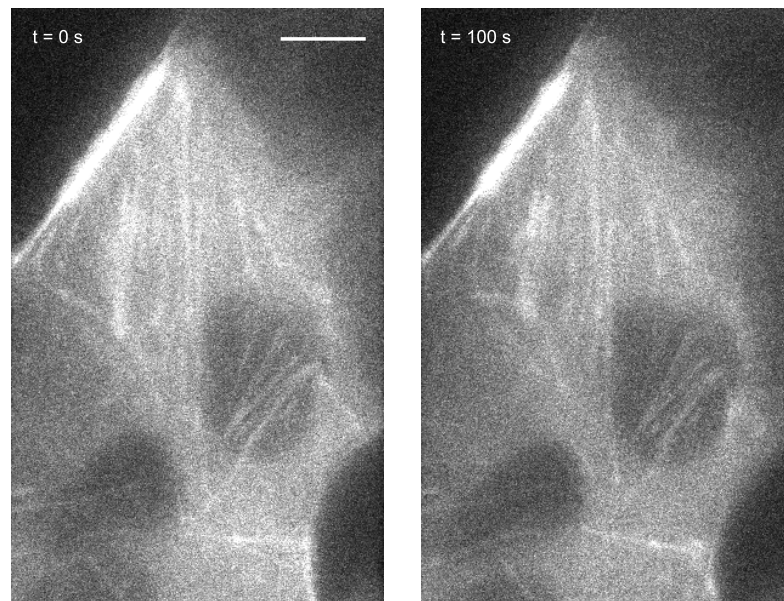
(b) TPPS$_{2a}$-treated actin-GFP expressing cell

Figure 6.2: The influence of TPPS$_{2a}$ on actin-GFP expressing cells. For both a control (a) and a TPPS$_{2a}$-treated (b) cell two images from a movie, recorded with 500 ms acquisition, are shown. Actin stress fibers are observed in both cases. No influence of the photosensitizer is observed. Scale bar: 10 μm.

in membranes [204], the 12 hours incubation time may have resulted in penetration of some photosensitizer through the membrane. This behavior was observed for the photosensitizer TPPS$_4$ where indirect evidence was given for localization of the photosensitizer in the cytosol and the nucleus [205].

Once in the cytosol, again two mechanisms exist to influence the microtubule dynamics. First, photoactivation may induce singlet oxygen production which in turn could react with microtubules. Second, direct binding of the photosensitizer to tubulin may inhibit polymerization and/or depolymerization processes. In this case activation of the photosensitizer is not necessary to inhibit microtubule motion.

Since inhibition of microtubule assembly is a well-known effect of porphyrins in the dark (without photosensitizer activation) [201], the latter process is expected to play the major role. As mentioned above, porphyrins bind to tubulin heterodimers and inhibit polymerization of free tubulin dimers. This may explain the absence of microtubule dynamics.

Since an intact microtubule network was observed after 12 hours of incubation and remained visible during the observation time, we suggest that depolymerization of microtubules does not occur.

In short, the data suggest that TPPS$_{2a}$ can penetrate membranes to a certain amount in the dark. The cytosolic pool of TPPS$_{2a}$ can bind to tubulin heterodimers resulting in distorted microtubule dynamics.

After characterizing the effect of TPPS$_{2a}$ on microtubules, the influence on the actin cytoskeleton was examined. In figure 6.2a two images from a movie, recorded with an acquisition time of 500 ms are shown. Figure 6.2a shows a control cell, incubated without photosensitizer. The stress fibers are easily recognized and the cytosolic fluorescence represents actin monomers. Figure 6.2b represents a TPPS$_{2a}$-treated cell. In this figure also cellular stress fibers are visible, although less distinct than for the control cell. This difference does not necessarily represent an effect of the photosensitizer on the cell. The amount of stress fibers differs per cell and per region of the cell. Stress fibers are especially abundant on the adhesion site of the cell. Changing the focal plane of the microscope thus results in different representations of the stress fibers. These observations therefore do not provide evidence for an influence of TPPS$_{2a}$ on the actin cytoskeleton.

6.2 Rab5 and Rab9

The original motivation for experiments with Rab5- and Rab9-GFP expressing cells was to verify the location of TPPS$_{2a}$. Rab5 and Rab9 are proteins that are expressed on early and late endosomes, respectively (see section 2.4). Thus, colocalization of the photosensitizer autofluorescence with Rab5-GFP and Rab9-GFP would provide information on localization of TPPS$_{2a}$ in early or late endosomes. Unfortunately, colocalization was ambiguous due to the low fluorescence intensity of TPPS$_{2a}$.

Nonetheless, an unexpected effect was observed upon excitation of Rab5-GFP and Rab9-GFP structures. For cells incubated with TPPS$_{2a}$ the endosomal fluorescence quickly vanished upon excitation with 488 nm laser light and the GFP signal of the endosomes dropped to
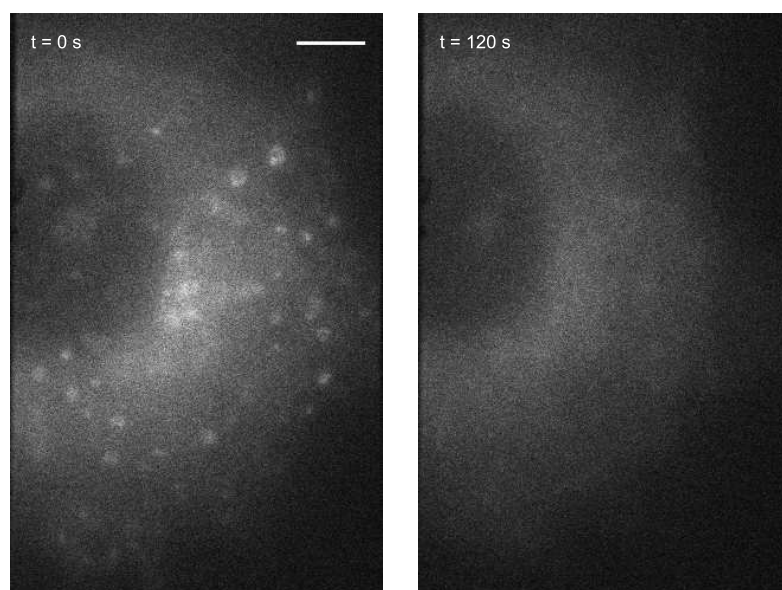
(a) TPPS$_{2a}$-treated Rab5-GFP expressing cell
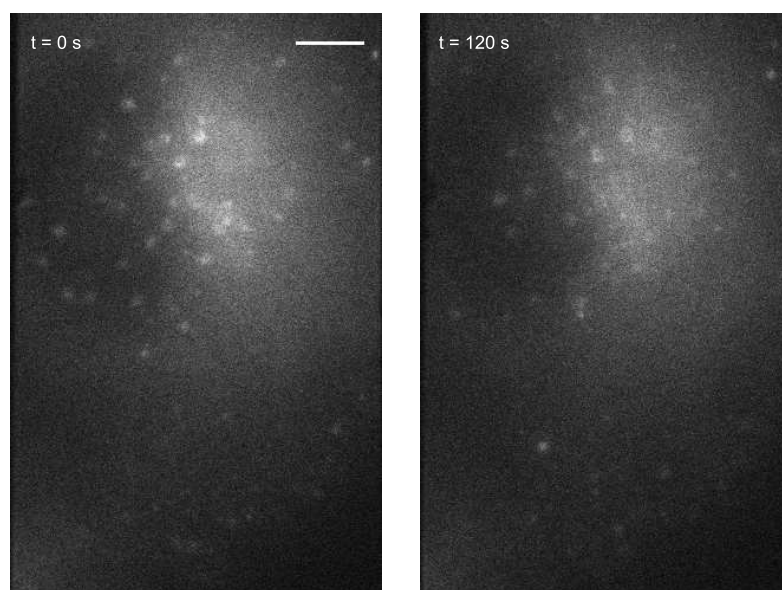
(b) Untreated Rab5-GFP expressing cell

Figure 6.3: The influence of TPPS$_{2a}$ activation on Rab5-GFP expressing cells. For both a TPPS$_{2a}$-treated (a) and a control (b) cell two images from a movie, recorded with 500 ms acquisition time under exactly the same experimental conditions and camera settings, are shown. Single endosomes can be distinguished for the TPPS$_{2a}$-treated cell at $t = 0$ s but have disappeared after 120 s. For the control cell endosomal fluorescence remains visible after 120 s. Scale bar: 5 μm.

background level.

Rab5- and Rab9-GFP expressing cells were seeded and treated similarly as described in the last section. It has to be noted that in the following experiments, the 405 nm laser was not used to activate the photosensitizer. Just as for the excitation of tubulin-GFP and actin-GFP, the intensity of the 488 nm laser was such that the photosensitizer was activated at this wavelength.

The effect of 488 nm excitation on Rab5-GFP expressing cells incubated overnight with TPPS$_{2a}$ is shown in figure 6.3a. The first image shows the cell directly after start of the illumination. The cell shows a high cytosolic background which indicates the boundary of the cell and the nucleus. No background fluorescence is observed within the cell nucleus. Single fluorescent structures represent GFP-expressing endosomes. After 120 seconds of illumination the signal of the endosomes has dropped to background level: single fluorescent endosomes cannot be detected anymore.

To exclude the possibility of GFP bleaching by the 488 nm laser, the experiment was repeated without TPPS$_{2a}$. Figure 6.3b shows an untreated Rab5-GFP expressing cell. The images were selected from a movie, recorded with an acquisition time of 500 ms under exactly the same experimental conditions and camera settings as the TPPS$_{2a}$-treated cell. In this case fluorescent endosomes are distinguished at $t = 0$ s as well as at $t = 120$ s. Single endosomes show a slight decrease in fluorescence intensity, most probably due to bleaching of GFP by laser light. The cytosolic background is lower than in the case of photosensitizer-treated cells.

A similar effect was observed for Rab9-GFP expressing cells. An example of a TPPS$_{2a}$-treated and a control cell is presented in figure 6.4. For both cells single endosomes can be distinguished at the start of illumination. After 25 seconds, the single endosomes in the TPPS$_{2a}$-treated cell have disappeared and only cytosolic background fluorescence is visible (figure 6.4a), whereas in the untreated cell single endosomes can easily be recognized (figure 6.4b).

These results show that the disappearance of single fluorescent structures in TPPS$_{2a}$-treated cells is due to the activation of TPPS$_{2a}$ rather than to bleaching of GFP by laser. For both Rab5- and Rab9-GFP expressing cells incubated with TPPS$_{2a}$ endosomal structures were detected immediately after start of illumination. This strongly indicates that the disappearance of fluorescent structures is dependent on singlet oxygen, generated upon illumination, and is not due to interaction of the photosensitizer itself with the Rab proteins.

To understand the influence of photosensitizer activation on Rab5 and Rab9 we first have to look at the mechanism of Rab protein membrane binding. Rab proteins are small GTPases that bind to the membrane of a specific compartment [206]. They play a role in vesicle fusion and transport [89, 207]. In the cytosol, Rab proteins are present in a GDP-bound conformation [208]. Binding to a GDI protein (GDP Dissociation Inhibitor) is necessary to deliver the Rab-GDP complex to the target membrane. In the membrane GDP is replaced by GTP which results in stable binding of the protein to the membrane [209]. Rab proteins can thus switch between a membrane-bound conformation and a cytosolic conformation. The observed disappearance of single fluorescent structures and the increased cytosolic fluorescence may therefore be
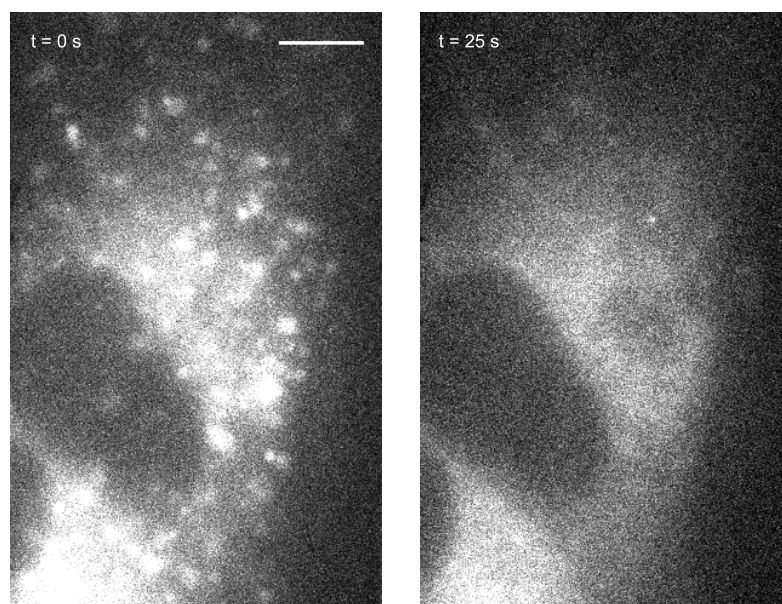
(a) TPPS$_{2a}$-treated Rab9-GFP expressing cell
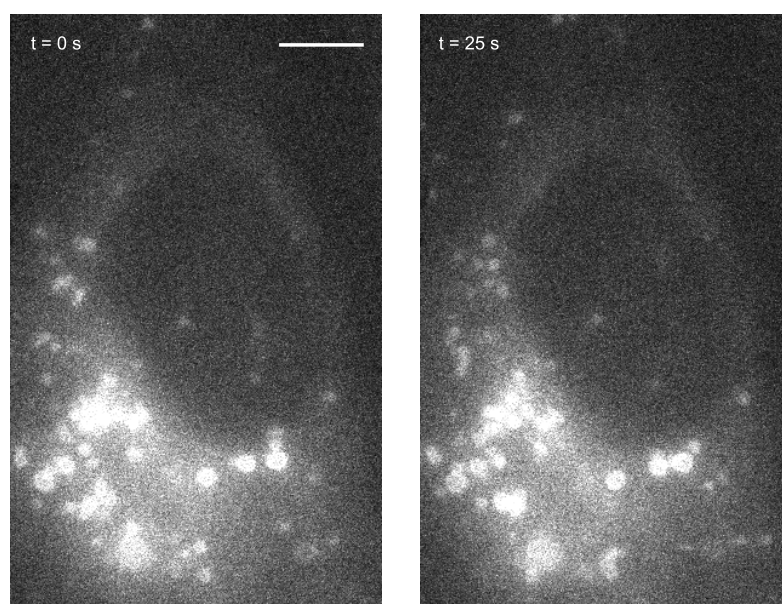
(b) Untreated Rab9-GFP expressing cell

Figure 6.4: The influence of TPPS$_{2a}$ activation on Rab9-GFP expressing cells. For both a TPPS$_{2a}$-treated (a) and a control (b) cell two images from a movie, recorded with 500 ms acquisition time under exactly the same experimental conditions and camera settings, are shown. Endosomal fluorescence is visible at $t = 0$ s but has disappeared after 25 s for the TPPS$_{2a}$-treated cell. For the control cell single endosomes can be distinguished at the start of illumination and after 25 s. Scale bar: 10 μm.

interpreted as the transition of Rab proteins from their membrane-bound conformation to their cytosolic form.

An obvious question now concerns the cause of this change in conformation. Rab proteins bind to the membrane by geranylgeranylation of the two C-terminal cysteins [210]. The geranylgeranylgroup integrates into the membrane resulting in stable binding. One possible explanation why Rab5 and Rab9 proteins transform to their cytosolic conformation might be singlet oxygen-induced damage of the cystein residues connecting Rab protein and geranylgeranylgroup. Cystein is one of the amino acids that are easily damaged by singlet oxygen [199, 211]. Since TPPS$_{2a}$ accumulates in the membrane of early and late endosomes and the diffusion radius of singlet oxygen is only 50 nm [106], the concentration of singlet oxygen is highest closest to the membrane. The cystein residues are therefore easily accessible to singlet oxygen.
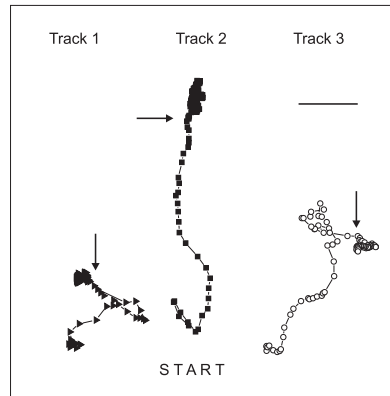
6.3 Stop of endosomal motion

An additional cellular effect of the photosensitizer was revealed during the experiments described in chapter 5. Since the intensity of the 488 nm laser used in those experiments was reduced compared to the aforementioned experiments, the 405 nm laser was used to induce photosensitizer activation. Endosomal motion stopped suddenly and completely upon photosensitizer activation, before the endosomal cargo was released into the cytosol. This effect was observed independent of endosomal cargo.

To illustrate this effect trajectories of the endosomal movement were generated as described before (section 3.5) and are presented in figure 6.5a. The corresponding instantaneous velocities of the trajectories and their mean square displacements were plotted versus time in figure 6.5b and figure 6.5c, respectively. In the first part of the trajectories, the endosomes move in an area of about 8 μm in diameter. In the corresponding instantaneous velocity plots velocities of up to 2 μm/s are observed. For all tracks directed movement is indicated by the quadratic dependence of $\langle r^2 \rangle$ on Δt in the mean square displacement plot.

After start of 405 nm illumination, marked by black arrows in figure 6.5a and figure 6.5b, endosomal motion ceased in all tracks. This is illustrated in the trajectories by a reduction of the area of movement from 8 μm to 2 μm in diameter. In the velocity plot a sudden decrease in velocity to less than 0.3 μm/s is depicted. After 65 seconds the endosomes could not be tracked further, because their fluorescent cargo was released into the cytosol. For cells incubated with photosensitizer and particles for only two hours the same effect was observed.

The time point of endosomal stalling and endosomal release was strongly dependent on the laser intensity. Higher laser intensity induced earlier onset of those events. Importantly, the order of these events - motion, stop of motion, and release of cargo - was always the same. In sharp contrast to the stop of microtubule movement, interpreted as a dark effect (without photosensitizer activation), stop of endosomal motion was only induced by illumination with the 405 nm laser. Therefore this event seems to be dependent on the formation of singlet oxygen.

(a) Trajectories
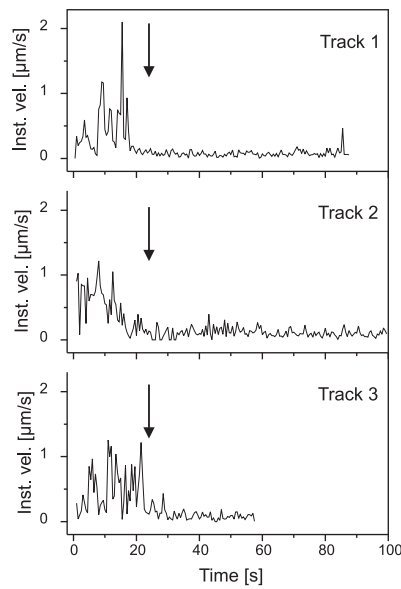
(b) Instantaneous velocity plot
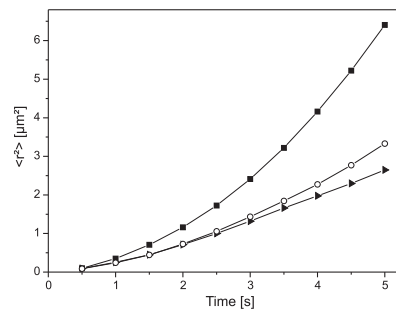
(c) Mean square displacement

Figure 6.5: Illustration of stop of endosomal motion for three particles. Upon 405 nm illumination (marked with black arrows), a reduction in the area of movement is observed in the trajectories (a) resulting in a decrease in instantaneous velocities (b). Before 405 nm illumination the particles showed directed movement (c). Scale bar (a): 2 μm.

The inhibition of active transport along microtubules was not caused by photochemical damage of microtubules as the experiments with tubulin-GFP cells described in section 6.1 showed an intact microtubule cytoskeleton upon photosensitizer activation. This indicates that endosomal stalling may be induced by singlet oxygen damage and may involve motor proteins. Singlet oxygen has a limited diffusion radius (50 nm) from its site of generation [106]. As TPPS$_{2a}$ is attached to endosomal membranes and presumably to microtubules, the generated singlet oxygen could interact at some point in the link between microtubules and endosomal transport. This may occur either by direct damage of motor proteins or by destruction of proteins involved in linkage of motor proteins to membranes.

It has been shown that Rab proteins play a role in vesicle mobility and fusion [89, 207]. They are associated with the link between motor proteins and endosomes [207, 212, 213]. As described in section 6.2 photosensitizer activation may induce relocation of Rab proteins from the endosomal membrane to the cytosol. The dissociation of Rab proteins from endosomes could thus result in loss of motor protein connection with the endosome. This would lead to an immediate stop of endosomal motion.

6.4 Summary

In this chapter the side effects of TPPS$_{2a}$ on cellular compartments were studied. These side effects may either be classified as resulting from intracellular singlet oxygen generation or from direct binding to TPPS$_{2a}$.

A stop of microtubule motion was observed that was interpreted as reduced polymerization of tubulin. Since an intact microtubule network was observed a decrease in depolymerization was not probable. A dark effect of porphyrins by binding to tubulin has been demonstrated before. This requires a direct interaction of photosensitizer and microtubules which may occur via penetration through the plasma membrane during the 12 hours incubation period.

A second side effect concerned Rab proteins. Rab5 and Rab9 are early and late endosome markers respectively and were transformed into their cytosolic form upon photosensitizer activation. Singlet oxygen may damage the link between Rab protein and endosomal membrane and thus the Rab protein may dissociate from the membrane and may be transported into the cytosol.

For the third side effect a clear dependence on photosensitizer activation was detected. Immediately after illumination with 405 nm laser light, stop of endosomal motion was observed. This stop was observed before cargo release occurred. Since Rab proteins connect endosomes to motor proteins and dissociation of the Rab proteins from the endosomal membrane was observed, the stop of endosomal motion may be caused by a loss of connection between endosomes and Rab proteins.

Bibliography

[1] Charisius H. Viren, die das Auge retten. Süddeutsche Zeitung, 2007. 28th April, p.1.

[2] Perrault I, Rozet JM, Gerber S, Ghazi I, Leowski C, et al. Leber congenital amaurosis. *Mol Genet Metab*, **68**(2) pp. 200–208, 1999.

[3] Bainbridge JWB, Smith AJ, Barker SS, Robbie S, Henderson R, et al. Effect of gene therapy on visual function in Leber's congenital amaurosis. *N Engl J Med*, 2008.

[4] Maguire AM, Simonelli F, Pierce EA, Pugh EN, Mingozzi F, et al. Safety and efficacy of gene transfer for Leber's congenital amaurosis. *N Engl J Med*, 2008.

[5] Rosenberg SA, Aebersold P, Cornetta K, Kasid A, Morgan RA, et al. Gene transfer into humans - immunotherapy of patients with advanced melanoma, using tumor-infiltrating lymphocytes modified by retroviral gene transduction. *N Engl J Med*, **323**(9) pp. 570–578, 1990.

[6] Stribley JM, Rehman KS, Niu H, and Christman GM. Gene therapy and reproductive medicine. *Fertil Steril*, **77**(4) pp. 645–657, 2002.

[7] Cho YW, Kim JD, and Park K. Polycation gene delivery systems: escape from endosomes to cytosol. *J Pharm Pharmacol*, **55**(6) pp. 721–734, 2003.

[8] Mislick KA and Baldeschwieler JD. Evidence for the role of proteoglycans in cation-mediated gene transfer. *Proc Natl Acad Sci U S A*, **93**(22) pp. 12349–12354, 1996.

[9] Payne CK, Jones SA, Chen C, and Zhuang X. Internalization and trafficking of cell surface proteoglycans and proteoglycan-binding ligands. *Traffic*, **8**(4) pp. 389–401, 2007.

[10] Hess GT, Humphries WH, Fay NC, and Payne CK. Cellular binding, motion, and internalization of synthetic gene delivery polymers. *Biochim Biophys Acta*, **1773**(10) pp. 1583–1588, 2007.

[11] Ruponen M, Ylä-Herttuala S, and Urtti A. Interactions of polymeric and liposomal gene delivery systems with extracellular glycosaminoglycans: physicochemical and transfection studies. *Biochim Biophys Acta*, **1415**(2) pp. 331–341, 1999.

[12] Kircheis R, Kichler A, Wallner G, Kursa M, Ogris M, et al. Coupling of cell-binding ligands to polyethylenimine for targeted gene delivery. *Gene Ther*, **4**(5) pp. 409–418, 1997.

[13] von Gersdorff K, Ogris M, and Wagner E. Cryoconserved shielded and EGF receptor targeted DNA polyplexes: cellular mechanisms. *Eur J Pharm Biopharm*, **60**(2) pp. 279–285, 2005.

[14] Ogris M, Steinlein P, Carotta S, Brunner S, and Wagner E. DNA/polyethylenimine transfection particles: influence of ligands, polymer size, and PEGylation on internalization and gene expression. *AAPS PharmSci*, **3**(3) p. E21, 2001.

[15] Puri C, Tosoni D, Comai R, Rabellino A, Segat D, et al. Relationships between EGFR signaling-competent and endocytosis-competent membrane microdomains. *Mol Biol Cell*, **16**(6) pp. 2704–2718, 2005.

[16] Sigismund S, Woelk T, Puri C, Maspero E, Tacchetti C, et al. Clathrin-independent endocytosis of ubiquitinated cargos. *Proc Natl Acad Sci U S A*, **102**(8) pp. 2760–2765, 2005.

[17] Engesaeter B, Bonsted A, Lillehammer T, Engebraaten O, Berg K, et al. Photochemically mediated delivery of AdhCMV-TRAIL augments the TRAIL-induced apoptosis in colorectal cancer cell lines. *Cancer Biol Ther*, **5**(11) pp. 1511–1520, 2006.

[18] Prasmickaite L, Hellum M, Kaalhus O, Høgset A, Wagner E, et al. Photochemical internalization of transgenes controlled by the heat-shock protein 70 promoter. *Photochem Photobiol*, **82**(3) pp. 809–816, 2006.

[19] Kloeckner J, Prasmickaite L, Høgset A, Berg K, and Wagner E. Photochemically enhanced gene delivery of EGF receptor-targeted DNA polyplexes. *J Drug Target*, **12**(4) pp. 205–213, 2004.

[20] Ryter SW and Tyrrell RM. Singlet molecular oxygen ($^1O_2$): a possible effector of eukaryotic gene expression. *Free Radic Biol Med*, **24**(9) pp. 1520–1534, 1998.

[21] de Bruin K, Ruthardt N, von Gersdorff K, Bausinger R, Wagner E, et al. Cellular dynamics of EGF receptor-targeted synthetic viruses. *Mol Ther*, **15**(7) pp. 1297–1305, 2007.

[22] Watson JD and Crick FH. Molecular structure of nucleic acids; a structure for deoxyribose nucleic acid. *Nature*, **171**(4356) pp. 737–738, 1953.

[23] Sullivan SM. Introduction to gene therapy and guidelines to pharmaceutical development. In Rolland A and Sullivan SM (editors), *Pharmaceutical gene delivery systems*, volume 131 of *Drugs and the pharmaceutical sciences*, pp. 1–16. Marcel Dekker, Inc., New York, NY, 2003.

[24] Flotte TR. Gene therapy: the first two decades and the current state-of-the-art. *J Cell Physiol*, **213**(2) pp. 301–305, 2007.

[25] Edelstein ML, Abedi MR, and Wixon J. Gene therapy clinical trials worldwide to 2007 - an update. *J Gene Med*, **9**(10) pp. 833–842, 2007.

[26] Raper SE, Chirmule N, Lee FS, Wivel NA, Bagg A, et al. Fatal systemic inflammatory response syndrome in a ornithine transcarbamylase deficient patient following adenoviral gene transfer. *Mol Genet Metab*, **80**(1-2) pp. 148–158, 2003.

[27] Hacein-Bey-Abina S, von Kalle C, Schmidt M, Deist FL, Wulffraat N, et al. A serious adverse event after successful gene therapy for X-linked severe combined immunodeficiency. *N Engl J Med*, **348**(3) pp. 255–256, 2003.

[28] Ott MG, Schmidt M, Schwarzwaelder K, Stein S, Siler U, et al. Correction of X-linked chronic granulomatous disease by gene therapy, augmented by insertional activation of MDS1-EVI1, PRDM16 or SETBP1. *Nat Med*, **12**(4) pp. 401–409, 2006.

[29] Morgan RA, Dudley ME, Wunderlich JR, Hughes MS, Yang JC, et al. Cancer regression in patients after transfer of genetically engineered lymphocytes. *Science*, **314**(5796) pp. 126–129, 2006.

[30] Slama J, Andree C, Winkler T, Swain WF, and Eriksson E. Gene transfer. *Ann Plast Surg*, **35**(4) pp. 429–439, 1995.

[31] Gary DJ, Puri N, and Won YY. Polymer-based siRNA delivery: perspectives on the fundamental and phenomenological distinctions from polymer-based DNA delivery. *J Control Release*, **121**(1-2) pp. 64–73, 2007.

[32] Kichler A. Gene transfer with modified polyethylenimines. *J Gene Med*, **6 Suppl 1** pp. S3–10, 2004.

[33] Walther W and Stein U. Viral vectors for gene transfer: a review of their use in the treatment of human diseases. *Drugs*, **60**(2) pp. 249–271, 2000.

[34] Bessis N, GarciaCozar FJ, and Boissier MC. Immune responses to gene therapy vectors: influence on vector function and effector mechanisms. *Gene Ther*, **11 Suppl 1** pp. S10–S17, 2004.

[35] Waehler R, Russell SJ, and Curiel DT. Engineering targeted viral vectors for gene therapy. *Nat Rev Genet*, **8**(8) pp. 573–587, 2007.

[36] Mrsny RJ. Tissue- and cell-specific targeting for the delivery of genetic information. In Amiji MM (editor), *Polymeric gene delivery*, chapter 2, pp. 5–28. CRC Press LLC, Boca Raton, Florida, 2005.

[37] Thomas CE, Ehrhardt A, and Kay MA. Progress and problems with the use of viral vectors for

gene therapy. *Nat Rev Genet*, **4**(5) pp. 346–358, 2003.

[38] van Gaal EVB, Hennink WE, Crommelin DJA, and Mastrobattista E. Plasmid engineering for controlled and sustained gene expression for nonviral gene therapy. *Pharm Res*, **23**(6) pp. 1053–1074, 2006.

[39] Uyechi-O'Brien LS and Szoka FC. Mechanisms for cationic lipids in gene transfer. In Rolland A and Sullivan SM (editors), *Pharmaceutical gene delivery systems*, volume 131 of *Drugs and the pharmaceutical sciences*, chapter 4, pp. 79–108. Marcel Dekker, Inc., New York, NY, 2003.

[40] Conwell CC and Huang L. Recent advances in non-viral gene delivery. In *Non-viral vectors for gene therapy*. Elsevier academic press, 2005.

[41] Wightman L, Kircheis R, Rössler V, Carotta S, Ruzicka R, et al. Different behavior of branched and linear polyethylenimine for gene delivery *in vitro* and *in vivo*. *J Gene Med*, **3**(4) pp. 362–372, 2001.

[42] Merdan T, Kopecek J, and Kissel T. Prospects for cationic polymers in gene and oligonucleotide therapy against cancer. *Adv Drug Deliv Rev*, **54**(5) pp. 715–758, 2002.

[43] Behr JP. The proton sponge: a trick to enter cells the viruses did not exploit. *Chimia*, **51** pp. 34–36, 1997.

[44] Boussif O, Lezoualc'h F, Zanta MA, Mergny MD, Scherman D, et al. A versatile vector for gene and oligonucleotide transfer into cells in culture and in vivo: polyethylenimine. *Proc Natl Acad Sci U S A*, **92**(16) pp. 7297–7301, 1995.

[45] Sonawane ND, Szoka FC, and Verkman AS. Chloride accumulation and swelling in endosomes enhances DNA transfer by polyamine-DNA polyplexes. *J Biol Chem*, **278**(45) pp. 44826–44831, 2003.

[46] Laemmli UK. Characterization of DNA condensates induced by poly(ethylene oxide) and polylysine. *Proc Natl Acad Sci U S A*, **72**(11) pp. 4288–4292, 1975.

[47] Kornguth SE and Stahmann MA. Effect of polylysine on the leakage and retention of compounds by Ehrlich ascites tumor cells. *Cancer Res*, **21** pp. 907–912, 1961.

[48] Shen WC and Ryser HJ. Conjugation of poly-L-lysine to albumin and horseradish peroxidase: a novel method of enhancing the cellular uptake of proteins. *Proc Natl Acad Sci U S A*, **75**(4) pp. 1872–1876, 1978.

[49] Pruzanski W and Saito S. The influence of natural and synthetic cationic substances on phagocytic activity of human polymorphonuclear cells. An alternative pathway of phagocytic enhancement. *Exp Cell Res*, **117**(1) pp. 1–13, 1978.

[50] Elferink JG. Cytolytic effect of polylysine on rabbit polymorphonuclear leukocytes. *Inflammation*, **9**(3) pp. 321–331, 1985.

[51] Reich Z, Ittah Y, Weinberger S, and Minsky A. Chiral and structural discrimination in binding of polypeptides with condensed nucleic acid structures. *J Biol Chem*, **265**(10) pp. 5590–5594, 1990.

[52] Plank C, Mechtler K, Szoka FC, and Wagner E. Activation of the complement system by synthetic DNA complexes: a potential barrier for intravenous gene delivery. *Hum Gene Ther*, **7**(12) pp. 1437–1446, 1996.

[53] Ogris M, Brunner S, Schüller S, Kircheis R, and Wagner E. PEGylated DNA/transferrin-PEI complexes: reduced interaction with blood components, extended circulation in blood and potential for systemic gene delivery. *Gene Ther*, **6**(4) pp. 595–605, 1999.

[54] Ward CM, Read ML, and Seymour LW. Systemic circulation of poly(L-lysine)/DNA vectors is influenced by polycation molecular weight and type of DNA: differential circulation in mice and rats and the implications for human gene therapy. *Blood*, **97**(8) pp. 2221–2229, 2001.

[55] Goula D, Benoist C, Mantero S, Merlo G, Levi G, et al. Polyethylenimine-based intravenous

delivery of transgenes to mouse lung. *Gene Ther*, **5**(9) pp. 1291–1295, 1998.

[56] Shir A, Ogris M, Wagner E, and Levitzki A. EGF receptor-targeted synthetic double-stranded RNA eliminates glioblastoma, breast cancer, and adenocarcinoma tumors in mice. *PLoS Med*, **3**(1) p. e6, 2006.

[57] Conner SD and Schmid SL. Regulated portals of entry into the cell. *Nature*, **422**(6927) pp. 37–44, 2003.

[58] May RC and Machesky LM. Phagocytosis and the actin cytoskeleton. *J Cell Sci*, **114**(Pt 6) pp. 1061–1077, 2001.

[59] Alberts B, Johnson A, Lewis J, Raff M, Roberts K, et al. *Molecular biology of the cell*. Garland Science, Taylor & Francis Group, LLC, 5th edition, 2008.

[60] Liu J and Shapiro JI. Endocytosis and signal transduction: basic science update. *Biol Res Nurs*, **5**(2) pp. 117–128, 2003.

[61] Robinson MS. The role of clathrin, adaptors and dynamin in endocytosis. *Curr Opin Cell Biol*, **6**(4) pp. 538–544, 1994.

[62] Gaidarov I, Santini F, Warren RA, and Keen JH. Spatial control of coated-pit dynamics in living cells. *Nat Cell Biol*, **1**(1) pp. 1–7, 1999.

[63] Merrifield CJ, Feldman ME, Wan L, and Almers W. Imaging actin and dynamin recruitment during invagination of single clathrin-coated pits. *Nat Cell Biol*, **4**(9) pp. 691–698, 2002.

[64] Merrifield CJ, Perrais D, and Zenisek D. Coupling between clathrin-coated-pit invagination, cortactin recruitment, and membrane scission observed in live cells. *Cell*, **121**(4) pp. 593–606, 2005.

[65] Ehrlich M, Boll W, Oijen AV, Hariharan R, Chandran K, et al. Endocytosis by random initiation and stabilization of clathrin-coated pits. *Cell*, **118**(5) pp. 591–605, 2004.

[66] Kirchhausen T. Clathrin. *Annu Rev Biochem*, **69** pp. 699–727, 2000.

[67] Carpentier JL, Gorden P, Anderson RG, Goldstein JL, Brown MS, et al. Co-localization of ^{125}I-epidermal growth factor and ferritin-low density lipoprotein in coated pits: a quantitative electron microscopic study in normal and mutant human fibroblasts. *J Cell Biol*, **95**(1) pp. 73–77, 1982.

[68] Schlessinger J, Shechter Y, Willingham MC, and Pastan I. Direct visualization of binding, aggregation, and internalization of insulin and epidermal growth factor on living fibroblastic cells. *Proc Natl Acad Sci U S A*, **75**(6) pp. 2659–2663, 1978.

[69] Haigler HT, McKanna JA, and Cohen S. Direct visualization of the binding and internalization of a ferritin conjugate of epidermal growth factor in human carcinoma cells a-431. *J Cell Biol*, **81**(2) pp. 382–395, 1979.

[70] Wilde A, Beattie EC, Lem L, Riethof DA, Liu SH, et al. EGF receptor signaling stimulates SRC kinase phosphorylation of clathrin, influencing clathrin redistribution and EGF uptake. *Cell*, **96**(5) pp. 677–687, 1999.

[71] Rust MJ, Lakadamyali M, Zhang F, and Zhuang X. Assembly of endocytic machinery around individual influenza viruses during viral entry. *Nat Struct Mol Biol*, **11**(6) pp. 567–573, 2004.

[72] Nichols BJ and Lippincott-Schwartz J. Endocytosis without clathrin coats. *Trends Cell Biol*, **11**(10) pp. 406–412, 2001.

[73] Sandvig K, Torgersen ML, Raa HA, and van Deurs B. Clathrin-independent endocytosis: from nonexisting to an extreme degree of complexity. *Histochem Cell Biol*, **129**(3) pp. 267–276, 2008.

[74] Hommelgaard AM, Roepstorff K, Vilhardt F, Torgersen ML, Sandvig K, et al. Caveolae: stable membrane domains with a potential for internalization. *Traffic*, **6**(9) pp. 720–724, 2005.

[75] Thomsen P, Roepstorff K, Stahlhut M, and van Deurs B. Caveolae are highly immobile plasma membrane microdomains, which are not involved in constitutive endocytic trafficking. *Mol Biol Cell*, **13**(1) pp. 238–250, 2002.

[76] Kurzchalia TV and Parton RG. Membrane microdomains and caveolae. *Curr Opin Cell Biol*, **11**(4) pp. 424–431, 1999.

[77] Norkin LC. Simian virus 40 infection via MHC class I molecules and caveolae. *Immunol Rev*, **168** pp. 13–22, 1999.

[78] Montesano R, Roth J, Robert A, and Orci L. Non-coated membrane invaginations are involved in binding and internalization of cholera and tetanus toxins. *Nature*, **296**(5858) pp. 651–653, 1982.

[79] Pelkmans L, Kartenbeck J, and Helenius A. Caveolar endocytosis of simian virus 40 reveals a new two-step vesicular-transport pathway to the ER. *Nat Cell Biol*, **3**(5) pp. 473–483, 2001.

[80] Henley JR, Krueger EW, Oswald BJ, and McNiven MA. Dynamin-mediated internalization of caveolae. *J Cell Biol*, **141**(1) pp. 85–99, 1998.

[81] Mayor S and Pagano RE. Pathways of clathrin-independent endocytosis. *Nat Rev Mol Cell Biol*, **8**(8) pp. 603–612, 2007.

[82] Gruenberg J and Maxfield FR. Membrane transport in the endocytic pathway. *Curr Opin Cell Biol*, **7**(4) pp. 552–563, 1995.

[83] Yamashiro DJ, Tycko B, Fluss SR, and Maxfield FR. Segregation of transferrin to a mildly acidic (pH 6.5) para-Golgi compartment in the recycling pathway. *Cell*, **37**(3) pp. 789–800, 1984.

[84] Rink J, Ghigo E, Kalaidzidis Y, and Zerial M. Rab conversion as a mechanism of progression from early to late endosomes. *Cell*, **122**(5) pp. 735–749, 2005.

[85] Mu FT, Callaghan JM, Steele-Mortimer O, Stenmark H, Parton RG, et al. EEA1, an early endosome-associated protein. EEA1 is a conserved alpha-helical peripheral membrane protein flanked by cysteine "fingers" and contains a calmodulin-binding IQ motif. *J Biol Chem*, **270**(22) pp. 13503–13511, 1995.

[86] Mills IG, Jones AT, and Clague MJ. Involvement of the endosomal autoantigen EEA1 in homotypic fusion of early endosomes. *Curr Biol*, **8**(15) pp. 881–884, 1998.

[87] Woodman PG. Biogenesis of the sorting endosome: the role of Rab5. *Traffic*, **1**(9) pp. 695–701, 2000.

[88] Gorvel JP, Chavrier P, Zerial M, and Gruenberg J. Rab5 controls early endosome fusion *in vitro*. *Cell*, **64**(5) pp. 915–925, 1991.

[89] Nielsen E, Severin F, Backer JM, Hyman AA, and Zerial M. Rab5 regulates motility of early endosomes on microtubules. *Nat Cell Biol*, **1**(6) pp. 376–382, 1999.

[90] Mellman I, Fuchs R, and Helenius A. Acidification of the endocytic and exocytic pathways. *Annu Rev Biochem*, **55** pp. 663–700, 1986.

[91] Piper RC and Luzio JP. Late endosomes: sorting and partitioning in multivesicular bodies. *Traffic*, **2**(9) pp. 612–621, 2001.

[92] Piper RC and Katzmann DJ. Biogenesis and function of multivesicular bodies. *Annu Rev Cell Dev Biol*, **23** pp. 519–547, 2007.

[93] Blanc IL, Luyet PP, Pons V, Ferguson C, Emans N, et al. Endosome-to-cytosol transport of viral nucleocapsids. *Nat Cell Biol*, **7**(7) pp. 653–664, 2005.

[94] Abrami L, Lindsay M, Parton RG, Leppla SH, and van der Goot FG. Membrane insertion of anthrax protective antigen and cytoplasmic delivery of lethal factor occur at different stages of the endocytic pathway. *J Cell Biol*, **166**(5) pp. 645–651, 2004.

[95] Bright NA, Gratian MJ, and Luzio JP. Endocytic delivery to lysosomes mediated by concurrent fusion and kissing events in living cells. *Curr Biol*, **15**(4) pp. 360–365, 2005.

[96] Riederer MA, Soldati T, Shapiro AD, Lin J, and Pfeffer SR. Lysosome biogenesis requires Rab9 function and receptor recycling from endosomes to the trans-Golgi network. *J Cell Biol*, **125**(3) pp. 573–582, 1994.

[97] Ganley IG, Carroll K, Bittova L, and Pfeffer S. Rab9 GTPase regulates late endosome size and requires effector interaction for its stability. *Mol Biol Cell*, **15**(12) pp. 5420–5430, 2004.

[98] Luzio JP, Poupon V, Lindsay MR, Mullock BM, Piper RC, et al. Membrane dynamics and the biogenesis of lysosomes. *Mol Membr Biol*, **20**(2) pp. 141–154, 2003.

[99] Mullock BM, Bright NA, Fearon CW, Gray SR, and Luzio JP. Fusion of lysosomes with late endosomes produces a hybrid organelle of intermediate density and is NSF dependent. *J Cell Biol*, **140**(3) pp. 591–601, 1998.

[100] Winchester B. Lysosomal metabolism of glycoproteins. *Glycobiology*, **15**(6) pp. 1R–15R, 2005.

[101] Dempsey CE. The actions of melittin on membranes. *Biochim Biophys Acta*, **1031**(2) pp. 143–161, 1990.

[102] Akinc A, Thomas M, Klibanov AM, and Langer R. Exploring polyethylenimine-mediated DNA transfection and the proton sponge hypothesis. *J Gene Med*, **7**(5) pp. 657–663, 2005.

[103] Høgset A, Prasmickaite L, Hellum M, Engesaeter BO, Olsen VM, et al. Photochemical transfection: a technology for efficient light-directed gene delivery. *Somat Cell Mol Genet*, **27**(1-6) pp. 97–113, 2002.

[104] Berg K, Selbo PK, Weyergang A, Dietze A, Prasmickaite L, et al. Porphyrin-related photosensitizers for cancer imaging and therapeutic applications. *J Microsc*, **218**(Pt 2) pp. 133–147, 2005.

[105] Redmond RW and Kochevar IE. Spatially resolved cellular responses to singlet oxygen. *Photochem Photobiol*, **82**(5) pp. 1178–1186, 2006.

[106] Moan J. On the diffusion length of singlet oxygen in cells and tissues. *J Photochem Photobiol B Bio*, **6** pp. 343–347, 1990.

[107] Dowty ME, Williams P, Zhang G, Hagstrom JE, and Wolff JA. Plasmid DNA entry into postmitotic nuclei of primary rat myotubes. *Proc Natl Acad Sci U S A*, **92**(10) pp. 4572–4576, 1995.

[108] Lukacs GL, Haggie P, Seksek O, Lechardeur D, Freedman N, et al. Size-dependent DNA mobility in cytoplasm and nucleus. *J Biol Chem*, **275**(3) pp. 1625–1629, 2000.

[109] Margalit A, Vlcek S, Gruenbaum Y, and Foisner R. Breaking and making of the nuclear envelope. *J Cell Biochem*, **95**(3) pp. 454–465, 2005.

[110] Brunner S, Sauer T, Carotta S, Cotten M, Saltik M, et al. Cell cycle dependence of gene transfer by lipoplex, polyplex and recombinant adenovirus. *Gene Ther*, **7**(5) pp. 401–407, 2000.

[111] Grosse S, Thévenot G, Monsigny M, and Fajac I. Which mechanism for nuclear import of plasmid DNA complexed with polyethylenimine derivatives? *J Gene Med*, **8**(7) pp. 845–851, 2006.

[112] Talcott B and Moore MS. Getting across the nuclear pore complex. *Trends Cell Biol*, **9**(8) pp. 312–318, 1999.

[113] van der Aa MAEM, Mastrobattista E, Oosting RS, Hennink WE, Koning GA, et al. The nuclear pore complex: the gateway to successful nonviral gene delivery. *Pharm Res*, **23**(3) pp. 447–459, 2006.

[114] Zanta MA, Belguise-Valladier P, and Behr JP. Gene delivery: a single nuclear localization signal peptide is sufficient to carry DNA to the cell nucleus. *Proc Natl Acad Sci U S A*, **96**(1) pp. 91–96, 1999.

[115] Sebestyén MG, Ludtke JJ, Bassik MC, Zhang G, Budker V, et al. DNA vector chemistry: the covalent attachment of signal peptides to plasmid DNA. *Nat Biotechnol*, **16**(1) pp. 80–85, 1998.

[116] von Gersdorff K. *PEG-shielded and EGF receptor targeted DNA polyplexes: cellular mechanisms*. Ph.D. thesis, LMU München, 2006.

[117] Plank C, Zatloukal K, Cotten M, Mechtler K, and Wagner E. Gene transfer into hepatocytes using asialoglycoprotein receptor mediated endocytosis of DNA complexed with an artificial tetra-antennary galactose ligand. *Bioconjug Chem*, **3**(6) pp. 533–539, 1992.

[118] Boeckle S, von Gersdorff K, van der Piepen S, Culmsee C, Wagner E, et al. Purification of polyethylenimine polyplexes highlights the role of free polycations in gene transfer. *J Gene Med*, **6**(10) pp. 1102–1111, 2004.

[119] Moerner W and Fromm D. Methods of single molecule fluorescence spectroscopy and microscopy. *Rev Sci Instrum*, **74**(8) pp. 3597–3619, 2003.

[120] Koehler A. A new system of illumination for photomicrographic purposes. *Zeitschrift fuer Wissenschaftliche Mikroskopie*, **10** pp. 433–440, 1893.

[121] Davidson MW and Abramowitz M. Optical microscopy. http://www.olympusmicro.com/primer/microscopy.pdf, 1999.

[122] Lichtman JW and Conchello JA. Fluorescence microscopy. *Nat Methods*, **2**(12) pp. 910–919, 2005.

[123] Abramowitz M. Microscope basics and beyond. For Olympus America Inc. http://www.olympusmicro.com/primer/basicsandbeyond.pdf, 2003.

[124] Inoue S and Spring K. *Video Microscopy*. Plenum Publishing, New York, NY, 2nd edition, 1997.

[125] Lakowicz JR. *Principles of fluorescence spectroscopy*. Kluwer Academic/Plenum publishers, New York, NY, 2nd edition, 2003.

[126] Atkins P and de Paula J. *Atkins' physical chemistry*. Oxford University Press, Oxford, 7th edition, 2002.

[127] Eftink MR. Fluorescence quenching: theory and applications. In Lakowicz JR (editor), *Principles*, volume 2 of *Topics in fluorescence spectroscopy*, chapter 2, p. 58. Plenum Press, New York, NY&, 1991.

[128] Nikon. How to use a microscope and take a photomicrograph. Nikon corporation, 1997.

[129] Schmidt T, Schütz GJ, Baumgartner W, Gruber HJ, and Schindler H. Imaging of single molecule diffusion. *Proc Natl Acad Sci U S A*, **93**(7) pp. 2926–2929, 1996.

[130] Saxton MJ and Jacobson K. Single-particle tracking: applications to membrane dynamics. *Annu Rev Biophys Biomol Struct*, **26** pp. 373–399, 1997.

[131] Levi V and Gratton E. Exploring dynamics in living cells by tracking single particles. *Cell Biochem Biophys*, **48**(1) pp. 1–15, 2007.

[132] Seisenberger G, Ried MU, Endress T, Büning H, Hallek M, et al. Real-time single-molecule imaging of the infection pathway of an adeno-associated virus. *Science*, **294**(5548) pp. 1929–1932, 2001.

[133] Kues T, Peters R, and Kubitscheck U. Visualization and tracking of single protein molecules in the cell nucleus. *Biophys J*, **80**(6) pp. 2954–2967, 2001.

[134] Lakadamyali M, Rust MJ, Babcock HP, and Zhuang X. Visualizing infection of individual influenza viruses. *Proc Natl Acad Sci U S A*, **100**(16) pp. 9280–9285, 2003.

[135] Ritchie K, Iino R, Fujiwara T, Murase K, and Kusumi A. The fence and picket structure of the plasma membrane of live cells as revealed by single molecule techniques (review). *Mol Membr Biol*, **20**(1) pp. 13–18, 2003.

[136] Yildiz A, Forkey JN, McKinney SA, Ha T, Goldman YE, et al. Myosin V walks hand-over-hand: single fluorophore imaging with 1.5-nm localization. *Science*, **300**(5628) pp. 2061–2065, 2003.

[137] Cheezum MK, Walker WF, and Guilford WH. Quantitative comparison of algorithms for tracking single fluorescent particles. *Biophys J*, **81**(4) pp. 2378–2388, 2001.

[138] Anderson CM, Georgiou GN, Morrison IE, Stevenson GV, and Cherry RJ. Tracking of cell surface receptors by fluorescence digital imaging microscopy using a charge-coupled device camera. Low-density lipoprotein and influenza virus receptor mobility at 4 degrees C. *J Cell Sci*, **101 (Pt 2)** pp. 415–425, 1992.

[139] Cover T and Hart P. Nearest neighbor pattern classification. *IEEE Trans Information Theory*, **13**

pp. 21–27, 1967.

[140] Saxton MJ. Lateral diffusion in an archipelago. Single-particle diffusion. *Biophys J*, **64**(6) pp. 1766–1780, 1993.

[141] Saxton MJ. Anomalous diffusion due to obstacles: a Monte Carlo study. *Biophys J*, **66**(2 Pt 1) pp. 394–401, 1994.

[142] Saxton MJ. Single-particle tracking: models of directed transport. *Biophys J*, **67**(5) pp. 2110–2119, 1994.

[143] Saxton MJ. Single-particle tracking: effects of corrals. *Biophys J*, **69**(2) pp. 389–398, 1995.

[144] Saxton MJ. Anomalous diffusion due to binding: a Monte Carlo study. *Biophys J*, **70**(3) pp. 1250–1262, 1996.

[145] Saxton MJ. Single-particle tracking: the distribution of diffusion coefficients. *Biophys J*, **72**(4) pp. 1744–1753, 1997.

[146] Qian H, Sheetz MP, and Elson EL. Single particle tracking. Analysis of diffusion and flow in two-dimensional systems. *Biophys J*, **60**(4) pp. 910–921, 1991.

[147] Klessinger M and Michl J. *Excited states and photochemistry of organic molecules*. VCH Publishers, Inc., New York, NY, 1995.

[148] McNamee CE, Yamamoto S, and Higashitani K. Effect of the physicochemical properties of poly(ethylene glycol) brushes on their binding to cells. *Biophys J*, **93**(1) pp. 324–334, 2007.

[149] Belting M. Heparan sulfate proteoglycan as a plasma membrane carrier. *Trends Biochem Sci*, **28**(3) pp. 145–151, 2003.

[150] Kopatz I, Remy JS, and Behr JP. A model for non-viral gene delivery: through syndecan adhesion molecules and powered by actin. *J Gene Med*, **6**(7) pp. 769–776, 2004.

[151] Bernfield M, Götte M, Park PW, Reizes O, Fitzgerald ML, et al. Functions of cell surface heparan sulfate proteoglycans. *Annu Rev Biochem*, **68** pp. 729–777, 1999.

[152] Martinho RG, Castel S, Ureña J, Fernández-Borja M, Makiya R, et al. Ligand binding to heparan sulfate proteoglycans induces their aggregation and distribution along actin cytoskeleton. *Mol Biol Cell*, **7**(11) pp. 1771–1788, 1996.

[153] von Gersdorff K, Sanders NN, Vandenbroucke R, Smedt SCD, Wagner E, et al. The internalization route resulting in successful gene expression depends on both cell line and polyethylenimine polyplex type. *Mol Ther*, **14**(5) pp. 745–753, 2006.

[154] Rejman J, Bragonzi A, and Conese M. Role of clathrin- and caveolae-mediated endocytosis in gene transfer mediated by lipo- and polyplexes. *Mol Ther*, **12**(3) pp. 468–474, 2005.

[155] Grosse S, Aron Y, Thévenot G, François D, Monsigny M, et al. Potocytosis and cellular exit of complexes as cellular pathways for gene delivery by polycations. *J Gene Med*, **7**(10) pp. 1275–1286, 2005.

[156] Bausinger R, von Gersdorff K, Braeckmans K, Ogris M, Wagner E, et al. The transport of nanosized gene carriers unraveled by live-cell imaging. *Angew Chem Int Ed Engl*, **45**(10) pp. 1568–1572, 2006.

[157] DeRouchey J, Walker GF, Wagner E, and Rädler JO. Decorated rods: a "bottom-up" self-assembly of monomolecular DNA complexes. *J Phys Chem B*, **110**(10) pp. 4548–4554, 2006.

[158] Luten J, van Steenbergen MJ, Lok MC, de Graaff AM, van Nostrum CF, et al. Degradable PEG-folate coated poly(DMAEA-co-BA)phosphazene-based polyplexes exhibit receptor-specific gene expression. *Eur J Pharm Sci*, 2007.

[159] Herbst RS. Review of epidermal growth factor receptor biology. *Int J Radiat Oncol Biol Phys*, **59**(2 Suppl) pp. 21–26, 2004.

[160] Carpenter G. Receptors for epidermal growth factor and other polypeptide mitogens. *Annu Rev Biochem*, **56** pp. 881–914, 1987.

[161] Hinrichsen L, Harborth J, Andrees L, Weber K, and Ungewickell EJ. Effect of clathrin heavy chain- and alpha-adaptin-specific small inhibitory RNAs on endocytic accessory proteins and receptor trafficking in HeLa cells. *J Biol Chem*, **278**(46) pp. 45160–45170, 2003.

[162] Orth JD, Krueger EW, Weller SG, and McNiven MA. A novel endocytic mechanism of epidermal growth factor receptor sequestration and internalization. *Cancer Res*, **66**(7) pp. 3603–3610, 2006.

[163] Baulida J, Kraus MH, Alimandi M, Fiore PPD, and Carpenter G. All ErbB receptors other than the epidermal growth factor receptor are endocytosis impaired. *J Biol Chem*, **271**(9) pp. 5251–5257, 1996.

[164] Vonna L, Wiedemann A, Aepfelbacher M, and Sackmann E. Micromechanics of filopodia mediated capture of pathogens by macrophages. *Eur Biophys J*, **36**(2) pp. 145–151, 2007.

[165] Kress H, Stelzer EHK, Holzer D, Buss F, Griffiths G, et al. Filopodia act as phagocytic tentacles and pull with discrete steps and a load-dependent velocity. *Proc Natl Acad Sci U S A*, **104**(28) pp. 11633–11638, 2007.

[166] den Hartigh JC, van Bergen en Henegouwen PM, Verkleij AJ, and Boonstra J. The EGF receptor is an actin-binding protein. *J Cell Biol*, **119**(2) pp. 349–355, 1992.

[167] Sheetz MP, Turney S, Qian H, and Elson EL. Nanometre-level analysis demonstrates that lipid flow does not drive membrane glycoprotein movements. *Nature*, **340**(6231) pp. 284–288, 1989.

[168] Caspi A, Yeger O, Grosheva I, Bershadsky AD, and Elbaum M. A new dimension in retrograde flow: centripetal movement of engulfed particles. *Biophys J*, **81**(4) pp. 1990–2000, 2001.

[169] Keating E, Nohe A, and Petersen N. Studies of distribution, location and dynamic properties of EGFR on the cell surface measured by image correlation spectroscopy. *Eur Biophys J*, 2007.

[170] Arrio-Dupont M, Foucault G, Vacher M, Devaux PF, and Cribier S. Translational diffusion of globular proteins in the cytoplasm of cultured muscle cells. *Biophys J*, **78**(2) pp. 901–907, 2000.

[171] Luby-Phelps K. Cytoarchitecture and physical properties of cytoplasm: volume, viscosity, diffusion, intracellular surface area. *Int Rev Cytol*, **192** pp. 189–221, 2000.

[172] Tilney LG and Tilney MS. The wily ways of a parasite: induction of actin assembly by listeria. *Trends Microbiol*, **1**(1) pp. 25–31, 1993.

[173] Pelkmans L, Püntener D, and Helenius A. Local actin polymerization and dynamin recruitment in SV40-induced internalization of caveolae. *Science*, **296**(5567) pp. 535–539, 2002.

[174] Merrifield CJ, Moss SE, Ballestrem C, Imhof BA, Giese G, et al. Endocytic vesicles move at the tips of actin tails in cultured mast cells. *Nat Cell Biol*, **1**(1) pp. 72–74, 1999.

[175] Taunton J, Rowning BA, Coughlin ML, Wu M, Moon RT, et al. Actin-dependent propulsion of endosomes and lysosomes by recruitment of N-WASP. *J Cell Biol*, **148**(3) pp. 519–530, 2000.

[176] Murray JW, Bananis E, and Wolkoff AW. Reconstitution of ATP-dependent movement of endocytic vesicles along microtubules *in vitro*: an oscillatory bidirectional process. *Mol Biol Cell*, **11**(2) pp. 419–433, 2000.

[177] King SJ and Schroer TA. Dynactin increases the processivity of the cytoplasmic dynein motor. *Nat Cell Biol*, **2**(1) pp. 20–24, 2000.

[178] Suh J, Wirtz D, and Hanes J. Efficient active transport of gene nanocarriers to the cell nucleus. *Proc Natl Acad Sci U S A*, **100**(7) pp. 3878–3882, 2003.

[179] Berg K, Selbo PK, Prasmickaite L, Tjelle TE, Sandvig K, et al. Photochemical internalization: a novel technology for delivery of macromolecules into cytosol. *Cancer Res*, **59**(6) pp. 1180–1183, 1999.

[180] Høgset A, Prasmickaite L, Tjelle TE, and Berg K. Photochemical transfection: a new technology for light-induced, site-directed gene delivery. *Hum Gene Ther*, **11**(6) pp. 869–880, 2000.

[181] Selbo PK, Sivam G, Fodstad O, Sandvig K, and Berg K. In vivo documentation of photochemical

internalization, a novel approach to site specific cancer therapy. *Int J Cancer*, **92**(5) pp. 761–766, 2001.

[182] Ndoye A, Dolivet G, Høgset A, Leroux A, Fifre A, et al. Eradication of p53-mutated head and neck squamous cell carcinoma xenografts using nonviral p53 gene therapy and photochemical internalization. *Mol Ther*, **13**(6) pp. 1156–1162, 2006.

[183] Nishiyama N, Iriyama A, Jang WD, Miyata K, Itaka K, et al. Light-induced gene transfer from packaged DNA enveloped in a dendrimeric photosensitizer. *Nat Mater*, **4**(12) pp. 934–941, 2005.

[184] Falk J. *Porphyrins and metalloporphyrins*. Elsevier publishing company, 1964.

[185] LeGourrierec D, Andersson M, Davidsson J, Mukhtar E, Sun L, et al. Photoinduced electron transfer from a higher excited state of a porphyrin in a zinc porphyrin-ruthenium(II) trisbipyridine dyad. *J Phys Chem A*, **103 (5)** pp. 557–559, 1999.

[186] Bonnett R, McGarvey DJ, Harriman A, Land EJ, Truscott TG, et al. Photophysical properties of *meso*-tetraphenylporphyrin and some *meso*-tetra(hydroxyphenyl)porphyrins. *Photochem Photobiol*, **48**(3) pp. 271–276, 1988.

[187] Schmidt R. Photosensitized generation of singlet oxygen. *Photochem Photobiol*, **82**(5) pp. 1161–1177, 2006.

[188] Mehrdad Z, Noll A, Grabner EW, and Schmidt R. Sensitization of singlet oxygen *via* encounter complexes and *via* exciplexes of $\pi\pi*$ triplet excited sensitizers and oxygen. *Photochem Photobiol Sci*, **1**(4) pp. 263–269, 2002.

[189] Korinek M, Dedic R, Svoboda A, and Hála J. Luminescence study of singlet oxygen production by *meso*-tetraphenylporphine. *J Fluoresc*, **14**(1) pp. 71–74, 2004.

[190] Berlin RD and Oliver JM. Surface functions during mitosis. II. quantitation of pinocytosis and kinetic characterization of the mitotic cycle with a new fluorescence technique. *J Cell Biol*, **85**(3) pp. 660–671, 1980.

[191] Probes M. Product information: dextran conjugates. Revised 05-april-2006.

[192] Seksek O, Biwersi J, and Verkman AS. Translational diffusion of macromolecule-sized solutes in cytoplasm and nucleus. *J Cell Biol*, **138**(1) pp. 131–142, 1997.

[193] Akinc A and Langer R. Measuring the pH environment of DNA delivered using nonviral vectors: implications for lysosomal trafficking. *Biotechnol Bioeng*, **78**(5) pp. 503–508, 2002.

[194] Capan Y, Woo BH, Gebrekidan S, Ahmed S, and DeLuca PP. Stability of poly(L-lysine)-complexed plasmid DNA during mechanical stress and DNase I treatment. *Pharm Dev Technol*, **4**(4) pp. 491–498, 1999.

[195] Ramsay E and Gumbleton M. Polylysine and polyornithine gene transfer complexes: a study of complex stability and cellular uptake as a basis for their differential *in-vitro* transfection efficiency. *J Drug Target*, **10**(1) pp. 1–9, 2002.

[196] Itaka K, Harada A, Yamasaki Y, Nakamura K, Kawaguchi H, et al. In situ single cell observation by fluorescence resonance energy transfer reveals fast intra-cytoplasmic delivery and easy release of plasmid DNA complexed with linear polyethylenimine. *J Gene Med*, **6**(1) pp. 76–84, 2004.

[197] Huth S, Hoffmann F, von Gersdorff K, Laner A, Reinhardt D, et al. Interaction of polyamine gene vectors with RNA leads to the dissociation of plasmid DNA-carrier complexes. *J Gene Med*, **8**(12) pp. 1416–1424, 2006.

[198] van Weert AW, Dunn KW, Gueze HJ, Maxfield FR, and Stoorvogel W. Transport from late endosomes to lysosomes, but not sorting of integral membrane proteins in endosomes, depends on the vacuolar proton pump. *J Cell Biol*, **130**(4) pp. 821–834, 1995.

[199] Spikes JD and Straight R. Sensitized photochemical processes in biological systems. *Annu Rev Phys Chem*, **18** pp. 409–436, 1967.

[200] Ochsner M. Photophysical and photobiological processes in the photodynamic therapy of tumours. *J Photochem Photobiol B*, **39**(1) pp. 1–18, 1997.

[201] Boekelheide K, Eveleth J, Tatum AH, and Winkelman JW. Microtubule assembly inhibition by porphyrins and related compounds. *Photochem Photobiol*, **46**(5) pp. 657–661, 1987.

[202] Tian F, Johnson EM, Zamarripa M, Sansone S, and Brancaleon L. Binding of porphyrins to tubulin heterodimers. *Biomacromolecules*, **8**(12) pp. 3767–3778, 2007.

[203] Berg K. The unpolymerized form of tubulin is the target for microtubule inhibition by photoactivated tetra(4-sulfonatophenyl)porphine. *Biochim Biophys Acta*, **1135**(2) pp. 147–153, 1992.

[204] Berg K, Western A, Bommer JC, and Moan J. Intracellular localization of sulfonated *meso*-tetraphenylporphines in a human carcinoma cell line. *Photochem Photobiol*, **52**(3) pp. 481–487, 1990.

[205] Berg K, Moan J, Bommer JC, and Winkelman JW. Cellular inhibition of microtubule assembly by photoactivated sulphonated *meso*-tetraphenylporphines. *Int J Radiat Biol*, **58**(3) pp. 475–487, 1990.

[206] Zerial M and McBride H. Rab proteins as membrane organizers. *Nat Rev Mol Cell Biol*, **2**(2) pp. 107–117, 2001.

[207] Jordens I, Marsman M, Kuijl C, and Neefjes J. Rab proteins, connecting transport and vesicle fusion. *Traffic*, **6**(12) pp. 1070–1077, 2005.

[208] Pfeffer S. A model for Rab GTPase localization. *Biochem Soc Trans*, **33**(Pt 4) pp. 627–630, 2005.

[209] Ali BR and Seabra MC. Targeting of Rab GTPases to cellular membranes. *Biochem Soc Trans*, **33**(Pt 4) pp. 652–656, 2005.

[210] Goody RS, Rak A, and Alexandrov K. The structural and mechanistic basis for recycling of rab proteins between membrane compartments. *Cell Mol Life Sci*, **62**(15) pp. 1657–1670, 2005.

[211] Davies MJ. Singlet oxygen-mediated damage to proteins and its consequences. *Biochem Biophys Res Commun*, **305**(3) pp. 761–770, 2003.

[212] Pfeffer SR. Motivating endosome motility. *Nat Cell Biol*, **1**(6) pp. E145–E147, 1999.

[213] Hammer JA and Wu XS. Rabs grab motors: defining the connections between Rab GTPases and motor proteins. *Curr Opin Cell Biol*, **14**(1) pp. 69–75, 2002.

Acknowledgments

List of publications

Peer-reviewed publications

De Bruin K, Ruthardt N, von Gersdorff K, Bausinger R, Ogris M, Wagner E, Bräuchle C. Cellular dynamics of EGF receptor-targeted synthetic viruses, *Mol. Ther.* **15** (7), p1297

De Bruin KG, Fella C, Ogris M, Wagner E, Bräuchle C. Dynamics of photoinduced endosomal release of polyplexes, *accepted for publication in Journal of Controlled Release*

Oral presentations

De Bruin KG, Photochemical release of artificial viruses, Gene Therapy Meeting, LMU Munich, June 2007

Poster presentations

De Bruin KG, Ruthardt N, Braeckmans K, Wagner E, Bräuchle C, Uptake kinetics and dynamics of functionalized and non-functionalized polyplexes in HUH7 cells, Annual Meeting of the European Society of Gene Therapy, Athens, November 2006

De Bruin KG, Ruthardt N, Wagner E, Bräuchle C, Uptake kinetics and dynamics of functionalized and non-functionalized polyplexes in HUH7 cells, CeNS Winter School 2007, Mauterndorf, February 2007

De Bruin KG, Ruthardt N, Braeckmans K, Wagner E, Bräuchle C, Observation of nanoparticle uptake in living cells by single particle tracking, 58. Mosbacher Kolloquium (Gesellschaft für Biochemie und Molekularbiologie), Mosbach, March 2007

De Bruin KG, Ruthardt N, Fella C, Ogris M, Wagner E, Bräuchle C, Effects of photochemical release on a single cell level, Annual Meeting of the European Society of Gene Therapy, Rotterdam, November 2007

De Bruin KG, Fella C, Ogris M, Wagner E, Ruthardt N, Bräuchle C, A microscopic view on photoinduced polyplex release from endosomes, 10th European Symposium on Drug Delivery, Noordwijk, April 2008

Curriculum Vitae

Karla de Bruin

Date of birth	23 July 1979
Place of birth	Almelo, Netherlands
Nationality	Dutch
Marital status	Unmarried

Education

Jan 2005 – July 2008	PhD in physical chemistry under supervision of Prof. C. Bräuchle, LMU Munich
Sep 2002 – March 2003	Master thesis in physical chemistry under supervision of Prof. F. Merkt, ETH Zurich
Sep 1998 – Aug 2003	MSc. in chemistry, University of Amsterdam
Sep 1991 – June 1997	High school, Almelo, Netherlands

Awards and scholarships

April 2008	Jan Feijen Prize for the best scientific poster presented during the 10th European Symposium on Controlled Drug Delivery
Sep 2003 – May 2004	"Bonusbeurs" scholarship of the University of Amsterdam
Sep 2002 – March 2003	Erasmus scholarship
Sep 2002 – March 2003	Scholarship of the "Stichting Vrijvrouwe van Renswoude"